Università degli Studi dell'Insubria
Department of Science and High Technology

Master Degree in PHYSICS
A.A. 2013-2014

THE FAMU EXPERIMENT:

MEASUREMENT OF MUONIC ATOMS SPECTRA

MASTER DEGREE THESIS

CANDIDATE:
Daniele Guffanti

ID: 708639

TUTOR:
Prof. Michela Prest
Università degli Studi dell'Insubria
& INFN Milano Bicocca

CO-TUTOR:
Dr. Erik Vallazza
INFN Trieste

COMO, MARCH 2015

Università degli Studi dell'Insubria
Department of Science and High Technology

Daniele Guffanti:
The FAMU experiment: Measurement of muonic atoms spectra
Master Degree Thesis in Physics

TUTOR: Prof. Michela Prest
CO-TUTOR: Dr. Erik Vallazza

Como, March 2015.

It does not do harm to the mystery to know a little about it.
— Richard Feynman

To all the ones who walked with me in these years

CONTENTS

Riassunto vii

Introduction 1

1 THE STRANGE CASE OF THE PROTON RADIUS 5
  - 1.1 A brief history of the proton 5
  - 1.2 Proton radius measurement strategy 7
    - 1.2.1 Proton radius measurement via electron scattering 8
    - 1.2.2 Proton charge radius from atomic spectroscopy measurements in hydrogen 17
    - 1.2.3 The proton radius puzzle: the Lamb Shift experiment 22

2 CONCEPT OF THE FAMU EXPERIMENT 29
  - 2.1 Physical origin of the hyperfine splitting 30
  - 2.2 Motivation of the measurement of the HFS in muonic hydrogen 34
  - 2.3 The FAMU experimental proposal 36
    - 2.3.1 Muonic atoms formation and thermalization 39
    - 2.3.2 Laser requirements 41
    - 2.3.3 Muon transfer to a higher-Z gas 43

3 THE 2014 BEAM TEST: EXPERIMENTAL SET-UP 49
  - 3.1 The RIKEN-RAL facility 49
    - 3.1.1 Muon beam properties 51
  - 3.2 Description of the experimental set-up 52
    - 3.2.1 The gas target 53
    - 3.2.2 The hodoscope 54
    - 3.2.3 $LaBr_3$(Ce) scintillating detectors 55
    - 3.2.4 HPGe detectors 58
  - 3.3 Data Acquisition 59
  - 3.4 Waveform analysis strategy 61
    - 3.4.1 Calibration and performance of the $LaBr_3$ scintillating detectors 63

4 DESCRIPTION OF THE RESULTS 69
  - 4.1 Geometrical description of the experimental set-up 69
  - 4.2 Beam energy calibration 70
  - 4.3 Data anlysis 71
    - 4.3.1 Graphite target 71
    - 4.3.2 Pure hydrogen target 73
    - 4.3.3 Argon target 79

4.3.4 Carbon dioxide target 82
4.4 Final remarks 87

5 CONCLUSIONS AND OUTLOOKS 89

List of Acronyms 93

List of Figures 94

List of Tables 99

BIBLIOGRAPHY 101

RIASSUNTO

Il cosiddetto *proton radius puzzle* è uno dei tanti problemi aperti nel panorama della fisica moderna. Il fatto che il protone potesse avere una struttura interna era già stato ipotizzato negli anni Trenta, quando le prime misure del momento magnetico del protone diedero risultati totalmente incompatibili con la previsione di Dirac. La prova definitiva del fatto che il protone non fosse una particella puntiforme dovette attendere lo sviluppo dei primi acceleratori di particelle: seguendo il percorso già tracciato da Rutherford, lo scattering elastico di elettroni di alta energia venne utilizzato da Hofstadter e collaboratori per indagare la struttura elettromagnetica del protone. Le deviazioni dalla sezione d'urto calcolata per una particella puntiforme furono tali da estrarre un valore del raggio quadratico medio della distribuzione di carica del protone dell'ordine di 1 fm.

Per molti anni lo scattering elastico di elettroni su nuclei di idrogeno è stato l'unico metodo per indagare la struttura del protone. Negli anni Novanta la sensibilità degli esperimenti di spettroscopia atomica divenne tale da rendere osservabili gli effetti della dimensione finita del protone sul *Lamb shift* dell'atomo di idrogeno. Il Lamb shift è la somma di tutti i contributi allo spettro energetico dell'atomo che non sono compresi nella descrizione della struttura fine e iperfine; tipicamente il contributo maggiore al Lamb shift è dovuto a correzioni di vertice o a loop calcolabili con una trattazione puramente quantistica dell'interazione elettromagnetica, mentre l'effetto del raggio finito del protone è piuttosto ridotto ma comunque misurabile. Le misure di spettroscopia atomica diedero risultati compatibili con quelli ottenuti attraverso gli esperimenti di scattering elastico, contribuendo ad aumentare la precisione del valore del raggio del protone.

Nel 2001 venne proposto un nuovo metodo per la stima del raggio del protone basato sulla misura del Lamb shift nell'idrogeno muonico, ovvero nel sistema legato formato da un protone e un muone (μp). Essendo il muone molto più pesante dell'elettrone, il raggio di Bohr del μp è circa duecento volte minore di quello dell'idrogeno ordinario e ciò porta a un contributo molto maggiore della dimensione del protone al Lamb shift. I risultati di questo esperimento furono pubblicati nel 2010 e fornirono un valore del raggio del protone molto inferiore a quello ottenuto dagli esperimenti di scattering e di spettroscopia atomica. La differenza tra i due valori era maggiore di 5σ; questo risultato inaspettato venne ulteriormente rinforzato nel 2013, quando vennero pubblicati nuovi risultati dell'esperimento che portarono la discrepanza tra le misure "muoniche" ed "elettroniche" sopra 7σ.

Questa differenza dopo cinque anni è ancora senza spiegazione e sono ancora molte le ipotesi in gioco: da incertezze non considerate nei metodi sperimen-

tali a effetti di nuova fisica al di là del Modello Standard. Questa tesi descrive i primi stadi dello sviluppo di un nuovo esperimento che mira a contribuire alla soluzione di questo enigma. Infatti anche lo splitting iperfine mostra una sensibile dipendenza dalla struttura del protone. Questo effetto è molto piccolo nell'idrogeno ordinario ($\approx 40\,\mathrm{ppm}$ nello stato fondamentale), ma diventa molto più rilevante nell'idrogeno muonico, dove contribuisce per lo 0.8% circa dell'energia della transizione iperfine nel *ground state*.

L'esperimento FAMU intende misurare, per la prima volta in maniera diretta, lo splitting iperfine dello stato fondamentale dell'atomo di idrogeno muonico con una precisione tale da poter estrarre il raggio di Zemach (ovvero il primo momento della convoluzione della densità di carica e di momento magnetico) del protone con una accuratezza $\leq 1\%$. Il confronto con i valori del raggio di Zemach ottenuti in precedenza considerando l'interazione tra protone ed elettrone potrà delimitare o rafforzare il proton radius puzzle: se l'esperimento desse valori compatibili spingerebbe a riconsiderare le metodologie delle misure del raggio quadratico medio della distribuzione di carica, mentre qualora si evidenziasse una discrepanza ci sarebbero ulteriori motivi per cercare effetti di nuova fisica.

La strategia sperimentale di FAMU combina tecniche proprie della fisica nucleare e sub-nucleare a quelle della spettroscopia atomica: atomi di idrogeno muonico nella configurazione di singoletto vengono eccitati nello stato di tripletto da un impulso laser con frequenza pari all'energia della transizione iperfine ($\lambda \approx 6.8\,\mu\mathrm{m}$); questi atomi si diseccitano nelle collisioni con altre molecole di H_2 ma circa 2/3 dell'energia della transizione è convertita in energia cinetica dell'atomo di idrogeno muonico, che risulta accelerato di $\approx 120\,\mathrm{meV}$. Questi μp "caldi" possono trasferire il proprio muone ad altri elementi con Z più alto con maggiore probabilità rispetto agli altri μp termalizzati, e il trasferimento del muone è seguito immediatamente dall'emissione di raggi-X caratteristici dell'atomo muonico così formato. Contando i raggi-X caratteristici emessi dopo l'impulso laser per diverse frequenze del laser stesso si ha una indicazione del numero di μp "caldi" da cui è possibile ricavare la posizione della risonanza dello splitting iperfine.

Una prima serie di misure atte a valutare la fattibilità dell'esperimento è stata effettuata nel giugno 2014 presso la RIKEN-RAL muon facility dei Rutherford-Appleton Laboratories (UK): un odoscopio letto da Silicon PhotoMultiplier era stato costruito per monitorare il fascio di muoni, mentre un rivelatore HPGe specificatamente indicato per la spettroscopia X e γ di bassa energia è servito da riferimento per gli spettri X generati dalle transizioni degli atomi muonici. Il cuore del sistema spettroscopico era costituito da rivelatori a scintillazione basati su cristalli di $LaBr_3$(Ce). Questi cristalli, oltre ad avere una eccellente risoluzione energetica, sono scintillatori estremamente veloci, e ciò li rende particolarmente indicati all'ambiente di misura che presentava un alto *event rate*. Per poter estrarre la maggior quantità di informazioni possibile dai rivelatori $LaBr_3$, il segnale in uscita da questi ultimi è stato registrato da un digitizer con una frequenza di campionamento di 500 MHz per un tempo di $5\,\mu\mathrm{s}$ successivo al trigger dato dall'arrivo del fascio di muoni. Ciò ha richiesto lo sviluppo di un algoritmo che analizzasse off-line le forme d'onda: questo programma è in grado di riconoscere automaticamente gli impulsi e di estrarre da questi tutte le informazioni utili (altezza, integrale, tempo, etc.) attraverso il fit della regione di interesse del segnale con una funzione che descrive uno o più impulsi a seconda della situazione. In questo modo è stato possibile identificare e recuperare gli eventi che altrimenti sarebbero stati scartati perché affetti da pile-up (circa il 26%).

Durante il test-beam sono stati esposti a un fascio di muoni di 61 MeV/c un bersaglio di grafite e tre diverse miscele di gas contenute in un vessel di alluminio. Per ognuno di questi bersagli è stato ricostruito lo spettro X: dagli spettri degli scintillatori $LaBr_3$ si sono potuti osservare tutti i picchi dovuti alle transizioni attese degli atomici muonici, confermando così la validità della scelta di questi rivelatori per l'esperimento in esame. Per ogni bersaglio si è studiato anche lo spettro temporale degli eventi: sebbene gli andamenti rispecchino le attese non è stato possibile spingersi in analisi più dettagliate vista l'assenza di uno studio teorico dedicato che spieghi anche l'origine del fondo osservato dagli scintillatori.

Un nuova presa dati sul fascio della RIKEN-RAL muon facility è prevista per l'estate del 2015: in questo nuovo test-beam verranno utilizzati quattro nuovi rivelatori basati su cristalli di $LaBr_3$(Ce) e un nuovo vessel dotato di un sistema criogenico. Nel frattempo è auspicabile lo sviluppo di una simulazione Monte Carlo per comprendere il ruolo che gli elettroni generati dal decadimento dei muoni possono avere nell'orgine del fondo.

INTRODUCTION

The hydrogen atom is one of the cornerstones of modern physics. The unknown origin of its discrete energy levels was one of the problems that boosted the formulation of quantum theory in the first years of the XX century, and the explanation of the discreteness of atomic spectra was one of the greatest achievements of this theory.

It's been a long time since Bohr's first works on the hydrogen atom (which preceded of more than a decade the formulation of the Schrödinger equation) and quantum physics has now a solid theoretical and experimental background[1], but the hydrogen atom still manages to astonish physicists.

Atomic spectroscopy measurements have reached in the years outstanding levels of precision, showing that the energy levels predicted by quantum mechanics were actually slightly shifted. The first observation of this phenomenon dates back in 1947 when the physicists Willis Lamb and Robert Retherford measured a small discrepancy between the $(2S)_{1/2} \rightarrow (2P)_{1/2}$ transition energy in hydrogen and the value predicted by the theory[2]. This observation was explained a few months later by Hans Bethe, opening the way for the development of a quantum theory of the electromagnetic field.

The so-called *Lamb shift* groups all the corrections to the energy levels predicted by the "standard" quantum mechanics, including radiative corrections, recoil effects and taking into account also the small effects of the nuclear structure instead of considering the nucleus as a point-like particle. The level of accuracy needed to measure the effect of the finite nuclear size (namely the RMS of the proton charge radius) on the hydrogen energy levels was reached in the nineties, providing values of the proton charge radius compatible with the ones obtained in previous experiments. Indeed, up to then the only way to investigate the size of the proton was through elastic scattering experiments. Following the legacy of Rutherford, many experiments of this type have been performed since the 1950s and their results, combined with the ones from spectroscopic measurements in hydrogen, contributed to determine the mean value of the proton charge radius

$$r_\text{p} = 0.8775 \pm 0.0051\,\text{fm}$$

In 2001 a new method was proposed. An accurate measurement of the Lamb shift in muonic hydrogen (a hydrogen atom where the electron is replaced by a muon) could provide a value of the RMS proton charge radius an order of magnitude more accurate than the ones obtained with ordinary hydrogen. In fact in muonic hydrogen the muon is much closer to the proton than the electron in the common hydrogen atom, thus the atomic energy levels are much more sensitive to the proton finite size.

---

[1] This despite the fact that Richard Feynman (Nobel prize in Physics in 1965 and one of the fathers of the quantum field theory) declared "I think I can safely say that nobody understands quantum mechanics".

[2] In 1955 Willis Lamb was honoured with the Nobel prize in Physics "for his discoveries concerning the fine structure of the hydrogen spectrum".

The first results of the proton size obtained from the measurement of the Lamb shift in muonic hydrogen were published in 2010, presenting a size of the proton incompatibly smaller with respect to the previous measurements.

This thesis work describes the first stages of a new experiment that can shed new light on this puzzle. Indeed, the Lamb shift is not the only contribution which depends on the proton size; also the hyperfine splitting presents a slight dependence on the proton structure. This effect is very small in ordinary hydrogen ($\sim 40\,\mathrm{ppm}$), but its importance is much more relevant in muonic hydrogen, where it contributes for $\sim 0.8\%$ of the transition energy. The FAMU experiment aims at measuring the hyperfine splitting of the ground state of muonic hydrogen for the first time in a direct way and with a high accuracy, which may allow to extract the Zemach radius (*i.e.* the first moment of the convolution of the charge and magnetic moment density distributions) of the proton with a precision $\leq 1\%$. The experimental method is a combination of particle physics and laser spectroscopy techniques: muonic hydrogen at the ground state and in singlet configuration is excited to the triplet state by means of a $\sim 6.8\,\mu\mathrm{m}$ wavelength laser pulse. Atoms in the triplet configuration are spin-flipped back to the singlet state colliding with H_2 molecules, but about 2/3 of the transition energy ($\approx 120\,\mathrm{meV}$) is converted into kinetic energy of the muonic hydrogen atom. These “hot” atoms can transfer their muons to some other higher-Z elements with a higher rate with respect to the thermalized atoms; the muon transfer event is promptly followed by the emission of a characteristic X-ray from the just formed muonic atoms, thus a detection system capable of performing X-ray spectroscopy with a precise timing of the events is needed.

In the first chapter of this thesis, the history of the measurements of the proton size will be presented considering the two “classical” approaches mentioned earlier: the proton–electron elastic scattering measurements and the spectroscopy of the hydrogen energy levels. The last part of the chapter is devoted to the description of the results of the Lamb shift experiment with muonic hydrogen, which raised the *proton radius puzzle*.

In chapter 2, after a brief summary of the physics behind the hyperfine splitting, the proposed measurement will be described. The experimental strategy is quite complex, thus only some of the key aspects of the proposed experiment are discussed in detail at the end of the chapter.

In June 2014 a first set of measurements has been performed at the RIKEN-RAL muon facility at the Rutherford Appleton Laboratories (UK) in order to test the feasibility of the experiment and the fitness of the experimental set-up imagined for this measurement. Different targets were exposed to an intense $61\,\mathrm{MeV}/c$ muon beam in order to measure the characteristic X-rays of the muonic atoms transitions and their time distribution. Chapter 3 is devoted to the description of the experimental set-up. A high-purity germanium detector specifically designed for the detection of low-energy X-rays was used to state a benchmark on the X-ray spectrum due to muonic atoms formed in the target. However, because of its long dead time it was not the ideal instrument. For their short decay time ($\sim 25\,\mathrm{ns}$) and good energy resolution, $\mathrm{LaBr_3(Ce)}$ scintillating crystals have been chosen as the main component of the detection system: as mentioned earlier, not only the energy spectrum is relevant, but also the timing of the recorded events has a capital importance. This is not an easy task, since the intense muon flux ($\sim 10^5$ muons/s on an area of $4 \times 4\,\mathrm{cm}^2$) corresponds to a high event rate that caused a relevant pile-up rate also in fast detectors like the ones based on $\mathrm{LaBr_3(Ce)}$. To overcome this problem and not lose any information for the analysis, the output of the $\mathrm{LaBr_3}$ detectors was recorded by a 500 MHz digitizer for a time of 5 µs after the beam trigger. An algorithm has been developed for the off-line analysis of the scintillating detectors waveforms; this program automatically detects the pulses and defines a “region of interest” which is fitted with a function describing one or more pulses, according to the situation. In this way, pile-up events are not only identified, but *recovered* for the analysis. This results in saving about 26% of the recorded events, that otherwise would have been rejected.

This strategy for the off-line pulse analysis allows to associate to each pulse a mathematical function, from which it is easy to extract almost every information about the pulse, like its height, its integral and its starting time. In particular, the X-ray spectrum can be obtained from the distribution of both the pulse height and the pulse integral. Comparing the results of these two approaches, the pulse integral method was found to provide a better energy resolution, compatible with the one obtained using a standard spectroscopic acquisition system.

The results of the beam test are described in chapter 4. The main goal of this test was to prove that a scintillator-based detection system is capable of performing X-ray spectroscopy with an energy resolution good enough while providing accurate information also on the time of the recorded events. During the beam test, three different gas targets and a graphite target were tested and all the expected lines of the characteristic X-rays due to the different transitions in the various muonic atoms have been identified. On the other hand, the obtained time spectra are difficult to judge since dedicated Monte Carlo simulations have to be implemented in order to understand the results. Also the origin of the background of the measurements, which is quite relevant, is not well understood yet and requires more theoretical work and Monte Carlo simulations to be explained and possibly reduced.

Finally, in chapter 5 some outlooks for the future development of the detection system will be presented.

CHAPTER 1

THE STRANGE CASE OF THE PROTON RADIUS

In 2010 one of the main cover stories of *Nature* was about a puzzling measurement of what it can appear as a simple property of one of the most known and studied particles in the history of physics: the proton. This particle is one of the building blocks of matter as we usually intend it and has been one of the first "elementary" particles being discovered in 1919 by Ernest Rutherford just a few years after his first idea about the atomic structure. Since then, the proton has been widely studied contributing fundamentally to build the Standard Model of Particle Physics (SM).

In the 2010 research the radius of the proton was measured with a technique never used before, giving a value totally incompatible with the previous measurements. This unexpected outcome raised great interest in the scientific community, and since then many other experiments have been proposed to try to solve this *puzzle*.

In this thesis work, a new method to measure the proton radius will be presented with the preliminary results of a first set of measurements whose goal was to test the feasibility of the proposed experiment.

In this chapter, after a brief introduction about the proton, the main strategy for the determination of the proton radius will be presented, from the "historical" elastic scattering measurement to the effect of the finite size of the proton on the hydrogen energy levels. The last part of the chapter is devoted to the "puzzling" measurement that raised the question of the proton radius.

1.1 A BRIEF HISTORY OF THE PROTON

The proton is an essential constituent of our universe. Together with the electron and the neutron, it is one of the three fundamental bricks that make up atoms and thus matter as we usually intend it.

In the long road to the discovery of the structure of matter, one of the first steps is due to Rutherford and his collaborators Geiger and Marsden, that in the early years of the twentieth century studied α particles scattered off a thin gold foil. Surprisingly, they observed that most of these particles crossed the foil almost undeflected but some of them were deflected at large angles in a way incompatible with the hypothesis of the positive charge spread in the atom volume [1]. This was the first evidence of the internal structure of the atom and led Rutherford to develop an atomic model as a hull of electrons surrounding a small positive-charged nucleus [2]. The unique role of the hydrogen nucleus, *i.e.* the proton, as a constituent of heavier nuclei was discovered when Rutherford transmuted nitrogen into oxygen through the reaction $^{14}\mathrm{N} + \alpha \rightarrow {}^{17}\mathrm{O} + \mathrm{p}$ [3]. The proton was then considered a fundamental particle just like the electron (discovered in 1897 by Thomson [4]) but heavier and with a positive charge. The subsequent discovery of the neutron by Chadwick in 1932 [5] seemed to complete the description of the building blocks of matter.

Besides these experimental discoveries, the quantum theory was quickly growing. The relativistic theory developed by Dirac to describe point-like spin-$\frac{1}{2}$ particles predicts a particle with mass M and charge Ze to have a magnetic moment

$$|\boldsymbol{\mu}| = \frac{g}{2}\frac{Ze}{M}\frac{\hbar}{2} \tag{1.1}$$

where g is the gyro-magnetic ratio and its predicted value is 2. Small deviations from the foreseen $g = 2$ gyro-magnetic ratio of the electron are perfectly explained by QED (Quantum electrodynamics) corrections. For the proton one defines

$$|\boldsymbol{\mu}| = \mu_\mathrm{p}\mu_N m_s \tag{1.2}$$

being $\mu_N = e\hbar/(2m_\mathrm{p})$ the nuclear magneton and m_s the spin quantum number. In the thirties Stern and collaborators found a value[1] of μ_p of about 2.5, totally inconsistent with the Dirac theory which predicts $\mu_\mathrm{p} = 1$ [7]. This was the first evidence that the proton was not just a heavier and positively charged electron, but it could have an internal structure.

However, in 1947 the picture of particle physics seemed complete: besides the proton, the neutron and the electron, the anti-electron predicted by the Dirac theory was discovered and the Yukawa theory of the interaction between nucleons to form atomic nuclei found its mediator in the pion. Apart the remarkable exception of the muon[2], every particle had its role and this scheme provided a fully satisfactory theory for the building blocks of matter.

The discovery of *strange* particles in cosmic rays [8] destroyed this comfortable picture. Gell-Mann [9] was able to arrange the known baryons (heavy particles such as p, n, Λ^0,. . .) and mesons (particles with a "middle"-mass between the proton and the electron like $\pi^\pm$, π^0,. . .) into geometrical patterns according to their quantum numbers. This intuition led to the hypothesis formulated independently by Gell-Mann and Zweig [10] that considers baryons and mesons as formed by three and two *quarks* respectively, a new type of elementary particle[3]. In the meantime, particle accelerators appeared on the scene of physics.

---

[1] The last value of the proton magnetic moment (in nuclear magnetons) recommended by CODATA (Committee on Data for Science and Technology) is $\mu_\mathrm{p} = 2.792847356(23)$ [6].

[2] The role of the muon was not clear and it looked like unnecessary in the overall picture. The puzzlement of the physicists of that time is well represented by the famous question of Isidore Rabi "Who ordered *that*?" speaking of the muon.

[3] Among the many phenomena explained by the quark theory, also the anomalous magnetic moment of the proton mentioned earlier can be easily understood in the framework of the quark model [11].

Experiments performed in the mid fifties by Hofstadter and collaborators at SLAC [12] (described in sec. 1.2.1) showed that the proton and the neutron have a finite size. The quark model was then integrated with Feynman's *parton* theory [13] and proved in deep inelastic scattering experiments at SLAC [14].

The quark theory described the proton as formed by three *valence* quarks (two *up* quarks and one *down* quark) and a number of other quarks—antiquarks pairs forming the so-called *sea* quarks; all these quarks interact via the exchange of *gluons*, that are the mediators of the strong interaction. The interaction between quarks is described by Quantum Chromodynamics (QCD). This theory works fine at high energy, but becomes almost impossible to manage in the low energy range. In recent years some of these difficulties have been overcome with the development of a particular discrete calculation technique (Lattice QCD), but despite some remarkable results [15], an accurate description of the electromagnetic structure of the proton is still far from being reached.

1.2 PROTON RADIUS MEASUREMENT STRATEGY

As shown in the previous section, the typical way to investigate the internal structure of an object in particle physics is to observe scattering processes. Historically, although the first evidence of an internal structure of the nucleon came from the measurement of the proton and neutron magnetic moment, the spatial distribution of the charge inside a nucleon remained unknown until elastic electron scattering experiments on proton and deuteron were performed in the mid-fifties by Hofstadter and collaborators[4].

The discovery of the internal structure of the proton, and thus of its finite size, led to discard the hypothesis that considered the proton as a point-like particle in the calculation of the hydrogen energy levels. Thanks to the extreme accuracy of QED predictions, these effects can be calculated and thus experimental spectroscopic measurements can provide further information about the electromagnetic structure of the proton.

In this section these complementary methods will be briefly described. Section 1.2.1 will present the theoretical foundations of e^-–p elastic scattering and the last measurements performed at the Mainz Microtron (MAMI), while in sec. 1.2.2 the main correction due to the finite proton size in hydrogen atomic levels will be described.

The proton RMS charge radius recommended value obtained by CODATA with a combined analysis from both e^-–p elastic scattering and hydrogen spectroscopy measurements is

$$r_\mathrm{p} = 0.8775 \pm 0.0051\,\mathrm{fm} \tag{1.3}$$

In 2010 another measurement of the proton charge radius was performed by Pohl and collaborators using the Lamb shift in *muonic* hydrogen (μp). This experiment is briefly described in sec. 1.2.3 and provides a value for the proton charge radius of [16]

---

[4] For his studies on the structure of the nucleons Robert Hofstadter was awarded with the Nobel prize in Physics in 1961.

$$r_{\mathrm{p}} = 0.84184 \pm 0.00067\,\mathrm{fm} \tag{1.4}$$

which differs from the CODATA 2006 reference value of 5σ. Further measurements on the $2S$-$2P$ transition frequency in muonic hydrogen worsened this difference, giving a value of $r_{\mathrm{p}} = 0.84087 \pm 0.00039\,\mathrm{fm}$ consistent with the previous μp measurement but 7σ distant from the CODATA value. These spectroscopy measurements exploiting muonic atoms and their non-compatibility with the previous "classical" measurements of the proton charge radius raised the so called *proton radius puzzle*, which is the reason of the experiment proposed and described in the following chapter.

1.2.1 *Proton radius measurement via electron scattering*

Scattering is a fundamental tool for physicists to investigate the properties of an object. As the structure of condensed matter can be studied by means of scattering of neutrons or X-rays, protons and neutrons can be examined in a similar way using electrons (or muons). Indeed, in his famous experiment, Rutherford studied α particles scattered by gold nuclei proving that the positive charge that balances the negative charge of electrons in an atom is concentrated in a much smaller volume than the one of the whole atom [2]. However, since α particles themselves are *not* point-like objects and can also interact via the strong force, they are not the best choice to dig into the internal structure of the proton. Electrons and muons, being point-like particles, are much more suited for such measurements.

For low energy scattering ($E \ll m_W$, where m_W is the W boson mass), the weak interaction between e^- and quarks forming the proton can be neglected, leaving only the electromagnetic interaction, whose theory (QED) can be considered well-established [17].

Theoretical introduction

The simplest case of scattering with electrons is the elastic case. In an elastic process energy and momentum are transferred from the electron to the nucleon via the exchange of a single photon without exciting any nuclear state. In his calculation of the differential cross section for a charged particle scattered off a heavier nucleus, Rutherford assumed a static and point-like target, leading to

$$\frac{\mathrm{d}\sigma}{\mathrm{d}\Omega}^{\mathrm{Ruth}} = \left(\frac{Z\alpha}{2E}\right)^2 \frac{1}{\sin^4\frac{\theta}{2}} \tag{1.5}$$

were $\alpha = e^2(4\pi)^{-1}$ is the fine structure constant ($\approx 1/137$), Z is the atomic number of the nucleus and θ is the electron scattering angle.

This result, derived using classical mechanics more than a century ago, allowed to describe Rutherford's experiment. However, to investigate the proton structure a spatial resolution of $\sim 1\,\mathrm{fm}$ is needed: using the scale set by

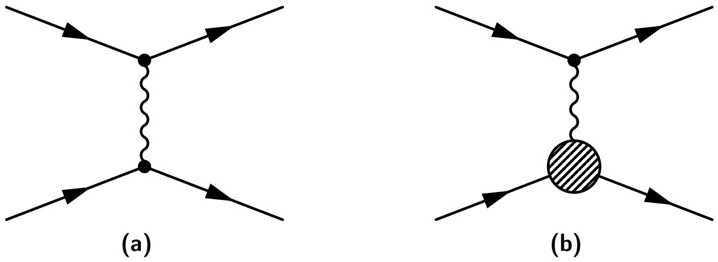

(a) (b)

Figure 1.1: Feynman diagrams representing the elastic scattering of an electron off **(a)** a heavier point-like particle (*e.g.* a muon) and **(b)** a proton.

$\hbar c \sim 200\,\mathrm{MeV}\cdot\mathrm{fm}$, it follows that $\sim 200\,\mathrm{MeV}/c$ momentum electrons, that are relativistic objects, are needed [17].

The relativistic expression of the cross section for elastic scattering off a static target is due to Mott [18]

$$\frac{\mathrm{d}\sigma}{\mathrm{d}\Omega}^{\mathrm{Mott}} = \frac{\mathrm{d}\sigma}{\mathrm{d}\Omega}^{\mathrm{Ruth}}\left(1-\beta\sin^2\tfrac{\theta}{2}\right) \tag{1.6}$$

being β the incident particle velocity in units of the speed of light ($\beta = v/c$). However, this expression still contains no information on the internal structure of the target. To appreciate the difference between a point-like target (*e.g.* a muon) and a finite size object, a full QED treatment is needed.

Let's start considering elastic scattering between two point-like, spin-$\frac{1}{2}$ objects, such as an electron and a muon. The cross section from the Feynman diagram in fig. 1.1a is [19, 20]

$$\mathrm{d}\sigma = \frac{1}{\mathscr{J}}\overline{|\mathscr{M}|}^2\frac{\mathrm{d}^3p'}{2E'(2\pi)^3}\frac{\mathrm{d}^3k'}{2\varepsilon'(2\pi)^3}(2\pi)^4\delta^{(4)}(p+k-p'-k') \tag{1.7}$$

where (p,p') and (k,k') are the initial and final four-momentum for the muon and the electron respectively and the $(2E')^{-1}$ and $(2\varepsilon')^{-1}$ factors (being E' and ε' the final energy of the muon and the electron) are related to the normalization of the wave functions in the final state. The calculation is carried out with the muon at rest in the laboratory frame, where the flux factor $\mathscr{J} = 4P\cdot k$ is simply $4M\varepsilon$ with M being the mass of the muon. The factor $\overline{|\mathscr{M}|}^2$ is the spin-averaged invariant amplitude and it follows from the Feynman rules of QED

$$\mathscr{M} = -e^2\bar{u}(k')\gamma^\mu u(k)\frac{1}{q^2}\bar{u}(p')\gamma_\mu\bar{u}(p) \tag{1.8}$$

where $u(k)$ and $u(p)$ are the spinors associated to the electron and the muon respectively and q is the exchanged four-momentum ($q = k-k'$). It is convenient to write the squared modulus, spin-averaged invariant amplitude as

$$\overline{|\mathscr{M}|}^2 = \frac{e^4}{q^4}L_e^{\mu\nu}L_{\mu\nu}^{\mathrm{muon}} \tag{1.9}$$

with the *leptonic* tensor defined as

$$L_e^{\mu\nu} = \tfrac{1}{2} \sum_{\text{spin}} \left[\bar{u}(k')\gamma^\mu u(k)\right] \left[\bar{u}(k')\gamma^\nu u(k)\right]^* \tag{1.10}$$

and similarly for $L_{\mu\nu}^{\text{muon}}$.

These tensors can be expressed in a much simpler form using trace identities [19, 20], resulting in

$$L^{\mu\nu} = 2\left[k'^\mu k^\nu + k^\mu k'^\nu - g^{\mu\nu}\left(k\cdot k' - m^2\right)\right] \tag{1.11}$$

Neglecting the electron mass and using $p' = p + k - k'$, one finds in the laboratory frame

$$\begin{aligned} L_e^{\mu\nu} L_{\mu\nu}^{\text{muon}} &= 8\left[2\left(p\cdot k'\right)\left(p\cdot k\right) + \left(k\cdot k'\right)\left(p\cdot q - m^2\right)\right] \\ &= 16 m^2 \varepsilon\varepsilon' \left(\cos^2\tfrac{\theta}{2} - \frac{q^2}{2m^2}\sin^2\tfrac{\theta}{2}\right) \end{aligned} \tag{1.12}$$

Integrating eq. (1.7) over d^3p' and inserting $\mathrm{d}k' = k'^2\mathrm{d}k'\mathrm{d}\Omega \simeq \varepsilon'\mathrm{d}\varepsilon'\mathrm{d}\Omega$, the differential cross section can be written in the form

$$\frac{\mathrm{d}^2\sigma}{\mathrm{d}\Omega\mathrm{d}\varepsilon'} = \frac{\alpha^2}{4\varepsilon^2\sin^4\frac{\theta}{2}}\left(\cos^2\tfrac{\theta}{2} - \frac{q^2}{2m^2}\sin^2\tfrac{\theta}{2}\right)\delta\left(\nu + \frac{q^2}{2m}\right) \tag{1.13}$$

where ν is $\varepsilon' - \varepsilon = E - E'$ and, given the fact that in an elastic process energy and momentum are conserved, $\nu = Q^2/2m$ (with $Q^2 = -q^2$).

Finally, the integration over $\mathrm{d}\varepsilon'$, with ε' kinematically determined by ε and θ

$$\varepsilon' = \frac{\varepsilon}{1 + (2\varepsilon/m)\sin^2\frac{\theta}{2}} \tag{1.14}$$

gives

$$\begin{aligned} \frac{\mathrm{d}\sigma}{\mathrm{d}\Omega}^{\text{pl}} &= \frac{\alpha^2}{4\varepsilon^2\sin^4\frac{\theta}{2}}\frac{1}{1+(2\varepsilon/m)\sin^2\frac{\theta}{2}}\left[1 - \frac{q^2}{2m^2}\tan^2\tfrac{\theta}{2}\right]\cos^2\tfrac{\theta}{2} \\ &= \left(\frac{\mathrm{d}\sigma}{\mathrm{d}\Omega}\right)^{\text{Mott}}_{\beta\to 1}\frac{\varepsilon'}{\varepsilon}\left[1 + \frac{Q^2}{2m^2}\tan^2\tfrac{\theta}{2}\right] \end{aligned} \tag{1.15}$$

where the ratio ε'/ε takes into account the recoil of the nucleon. Equation (1.15) is the cross-section for the scattering of two point-like spin-$\frac{1}{2}$ Dirac particles in the laboratory frame obtained using the rules of QED. But if one considers a proton, or any object with an internal structure, the situation is slightly different. As shown in the diagram in fig. 1.1b, in calculating the spin-averaged invariant amplitude one has to replace the leptonic tensor of the muon in eq. (1.9) with a *nucleon* tensor $N_{\mu\nu}$. In the definition of the leptonic tensor the standard electromagnetic current (and its expression obtained using the Gordon decomposition[5])

$$\begin{aligned} \left\langle\psi_e(k')\right| j^\mu(x)\left|\psi_e(k)\right\rangle &= \bar{u}(k')\gamma^\mu u(k)\mathrm{e}^{\mathrm{i}(k'-k)\cdot x} \\ &= \bar{u}(k')\left[\frac{(k'+k)^\mu}{2m} + \frac{\mathrm{i}\sigma^{\mu\nu}q_\nu}{2m}\right]u(k)\mathrm{e}^{\mathrm{i}(k'-k)\cdot x} \end{aligned} \tag{1.16}$$

---

[5] The $\sigma^{\mu\nu}$ tensor indicates the anti-symmetric tensor defined by $\sigma^{\mu\nu} = \frac{\mathrm{i}}{2}[\gamma^\mu, \gamma^\nu]$

was used ($|\psi_e(k)\rangle$ is the state vector of a free electron with momentum k), but since the proton is an extended object the exact form of the interaction current J^μ is unknown. Whatever the electromagnetic interaction is, J^μ must be a Lorenz four-vector: the most general four-vector that one can obtain from k, k', q and the Dirac γ-matrices between the $\bar{u}$ and u spinors includes only two independent terms, namely γ^μ and $\mathrm{i}\sigma^{\mu\nu}q_\nu$, and their coefficients are functions of Q^2 (since Q^2 is the only independent scalar variable at the proton vertex). The terms involving γ^5 are excluded by parity conservation.

Therefore, the general expression of the proton interaction current can be written as

$$\left\langle \psi_N(p')\right| J^\mu(x) \left|\psi_N(p')\right\rangle = e\bar{u}(p')\left[F_1(Q^2)\gamma^\mu + \frac{\mathrm{i}\sigma^{\mu\nu}q_\nu}{2M}\kappa F_2(Q^2)\right]u(p)\mathrm{e}^{\mathrm{i}(p'-p)\cdot x} \tag{1.17}$$

where $F_1(Q^2)$ and $F_2(Q^2)$ are two independent form factors also called Dirac- and Pauli- form factor respectively and κ is the anomalous magnetic moment of the proton[6]. Comparing eq.s (1.17) and (1.16), one can notice that for $Q^2 \to 0$, that is for long-wavelength photons, it does not make any difference that the nucleon has an internal structure at the order of 1 fm. In this case the proton will appear like a point-like particle of charge e and magnetic moment $1+\kappa$, i.e. $F_1(0) = 1$ and $F_2(0) = 1$.

The resulting cross section for an extended object, known as the Rosenbluth cross section, is

$$\frac{\mathrm{d}\sigma}{\mathrm{d}\Omega}^{\mathrm{Ros}} = \left(\frac{\mathrm{d}\sigma}{\mathrm{d}\Omega}^{\mathrm{Mott}}\right)\frac{\varepsilon'}{\varepsilon}\left\{F_1^2(Q^2) + \frac{Q^2}{4M^2}\left[\kappa^2F_2^2(Q^2) + \right.\right.$$
$$\left.\left. +2\left(F_1(Q^2)+\kappa F_2(Q^2)\right)^2\tan^2\tfrac{\theta}{2}\right]\right\} \tag{1.18}$$

It is more convenient to define the *Sachs form factors*

$$G_E(Q^2) = F_1(Q^2) - \frac{Q^2}{4M^2}\kappa F_2(Q^2) \tag{1.19}$$
$$G_M(Q^2) = F_1(Q^2) + \kappa F_2(Q^2) \tag{1.20}$$

also referred to as electric (G_E) and magnetic (G_M) form factors. At this point, the Rosenbluth cross section can be written in the form:

$$\frac{\mathrm{d}\sigma}{\mathrm{d}\Omega}^{\mathrm{Ros}} = \left(\frac{\mathrm{d}\sigma}{\mathrm{d}\Omega}^{\mathrm{Mott}}\right)\frac{\varepsilon'}{\varepsilon}\left\{\frac{G_E^2(Q^2)+\tau G_M^2(Q^2)}{1+\tau} + 2\tau G_M^2(Q^2)\tan^2\tfrac{\theta}{2}\right\} \tag{1.21}$$

where $\tau = Q^2/(2M^2)$. The physical meaning of the electric and magnetic form factors becomes clear in the Breit frame, defined by

$$p^{(\mathrm{B})} + p'^{(\mathrm{B})} = (2E^{(\mathrm{B})}, 0, 0, 0) \tag{1.22}$$

---

[6] The anomalous magnetic moment is defined as $\kappa = (g-2)/2$ where g is the gyromagnetic ratio. For the proton $\kappa \approx 1.79$.

In this frame, the first component of the proton transition current (eq. (1.17)) reduces to

$$\left\langle \psi_N\left(\frac{\boldsymbol{q}}{2}\right) \middle| J^0(x) \middle| \psi_N\left(\frac{-\boldsymbol{q}}{2}\right)\right\rangle = 2MeG_E(\boldsymbol{q}^2) \tag{1.23}$$

but the zeroth component of the electromagnetic current is the charge density, so eq. (1.23) can be written in an explicit form as[7]

$$2E(\boldsymbol{q})\int \mathrm{d}^3x\rho(\boldsymbol{x})\mathrm{e}^{\mathrm{i}\boldsymbol{q}\cdot\boldsymbol{x}} = 2MG_E(\boldsymbol{q}^2) \tag{1.24}$$

Thus the electric form factor $G_E(Q^2)$ is strictly connected with the Fourier transform (FT) of the charge density of the nucleon. In particular, for a small transferred momentum $\boldsymbol{q}$, $E(\boldsymbol{q}) \to M$, so that G_E can be approximatively interpreted as the FT of the charge density. Assuming an exponential trend in the charge density $\rho(r)$, the electric form factor is a dipole. The standard parametrization is the following:

$$G_E^{\text{st.dip.}}(Q^2) = \left(1 + \frac{Q^2}{0.71\,(\text{GeV}/c)^2}\right)^{-2} \tag{1.25}$$

In this situation, expanding the Fourier transform of $\rho(x)$ at small $\boldsymbol{q}$, one finds

$$\begin{aligned} G_E(Q^2) = \int \mathrm{d}^3x\rho(\boldsymbol{x})\mathrm{e}^{\mathrm{i}\boldsymbol{q}\cdot\boldsymbol{x}} &\simeq \int \mathrm{d}^3x\left[1 + \mathrm{i}\boldsymbol{q}\cdot\boldsymbol{x} - \tfrac{1}{2}(\boldsymbol{q}\cdot\boldsymbol{x})^2 - \ldots\right]\rho(\boldsymbol{x}) \\ &= Q(0) - \tfrac{1}{6}Q^2\int x^2\rho(\boldsymbol{x})\mathrm{d}^3x + \ldots \\ &= Q(0) - \tfrac{1}{6}Q^2\langle r^2\rangle + \ldots \end{aligned} \tag{1.26}$$

where $Q(0)$ is set by the charge of the nucleon ($Q(0) \simeq 0$ for the neutron and $Q(0) \simeq 1$ for the proton).

Therefore, the mean-squared charge radius of the nucleon is defined as

$$\langle r_E^2\rangle = -\frac{6}{G_E(0)}\left.\frac{\mathrm{d}G_E(Q^2)}{\mathrm{d}Q^2}\right|_{Q^2=0} \tag{1.27}$$

Similarly, it can be demonstrated that $G_M(Q^2)$ is related to the Fourier transform of the *magnetic* density, thus the mean-squared magnetic radius of the proton is

$$\langle r_M^2\rangle = -\frac{6}{G_M(0)}\left.\frac{\mathrm{d}G_M(Q^2)}{\mathrm{d}Q^2}\right|_{Q^2=0} \tag{1.28}$$

---

[7] Here the standard expression for the spinor $u(\boldsymbol{k}) = \sqrt{E+M}\begin{pmatrix}\chi_s \\ \frac{\boldsymbol{\sigma}\cdot\boldsymbol{k}}{E+M}\chi_s\end{pmatrix}$ is adopted.

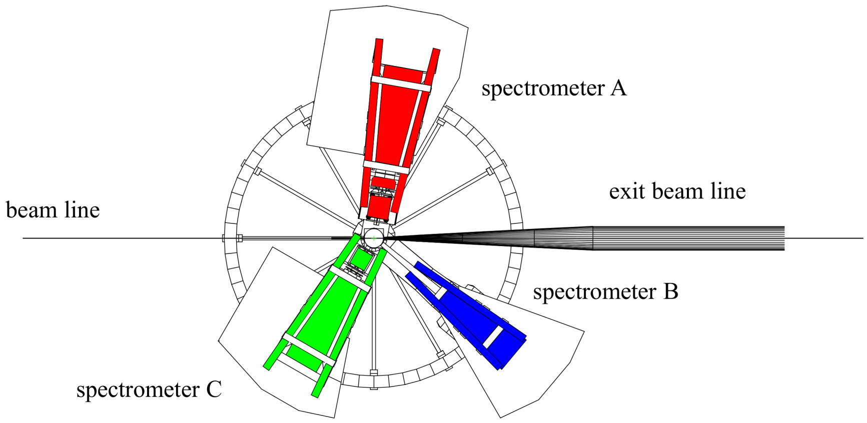

Figure 1.2: Scheme of the arrangement of the three spectrometers used at MAMI by the A1 collaboration [22].

Experimental measurements

Since the time of the Hofstadter experiment in the fifties, many experimental measurements of the electric and magnetic form factors of the proton and neutron have been performed. As shown in eq. (1.27), in order to obtain the charge radius the slope of the electric form factor $G_E(Q^2)$ at $Q^2 = 0$ must be extrapolated. The last measurements considered by CODATA for the 2010 review of the Recommended Values of the Fundamental Physical Constants [6], were the ones presented by Bernauer at al. in [21] on behalf of the A1 collaboration.

The results of the A1 collaboration were obtained from the analysis of 1400 cross sections measured at the Mainz Microtron using an electron beam in the 180–855 MeV energy-range, covering Q^2 from 0.004 to 1 (GeV/c)^2. The measurement of the elastic e^-–p cross section (eq. (1.21) with higher order electromagnetic corrections) with a statistical precision better than 2% was performed exploiting three high-resolution spectrometers, achieving to extract the form factors up to a negative four-momentum transfer squared of $Q^2 = 0.6$ (GeV/c)^2.

The arrangement of the three spectrometers is shown in fig. 1.2. The magnetic system of Spectrometer A and C is composed of a quadrupole, a sextupole and two dipoles (QSDD). This system allowed a high resolution measurement of the particle momentum and angle inside a relatively large angular acceptance (28 msr). The B spectrometer in fig. 1.2 is equipped with a single dipole magnet in clamshell configuration, characterized by a slim design, higher momentum resolution and smaller acceptance (5.6 msr) than the A and C spectrometers [22, 23].

Each of the three spectrometers has a momentum resolution of 10^{-4} and is equipped with a detector system consisting of two scintillator tiles of different thickness, two packets of two vertical drift chambers layers (VDC) and a gas Čerenkov detector (fig. 1.3).

The scintillators are used for triggering and to provide a time reference. The different thickness of the two planes (3 mm and 1 cm) allows to distinguish be-

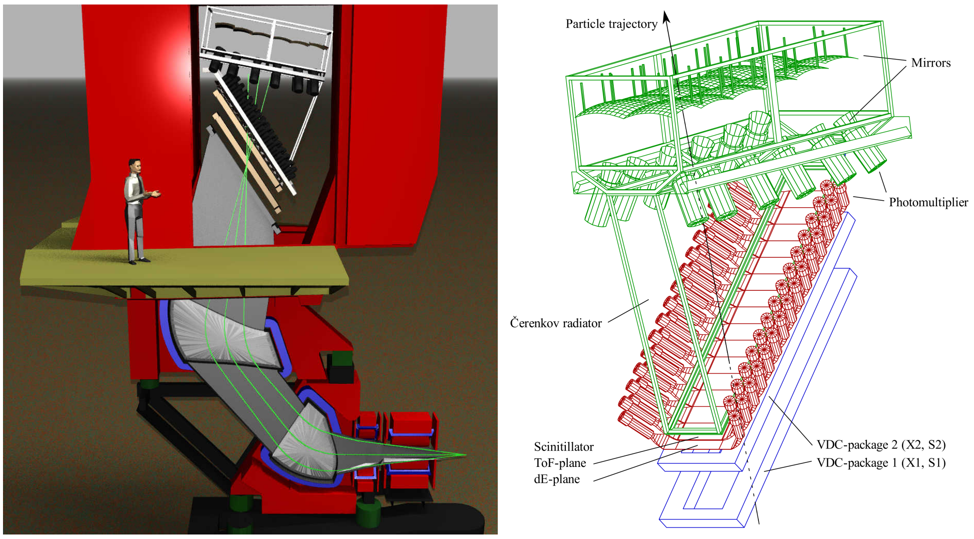

(a) **(b)**

Figure 1.3: **(a)** Rendering of one of the magnetic spectrometers A (from: `http://wwwa1.kph.uni-mainz.de/A1/gallery/`) and drawing of the detector system **(b)** [22].

tween minimum ionizing particles (MIPs) and heavier particles given the different energy deposit. The vertical drift chambers are used to reconstruct the particle trajectory inside the detector system with a spatial resolution of 200 µm and 400 µm in the dispersive and non-dispersive direction respectively, while the Čerenkov detector is used to discriminate electrons from heavier particles.

A cryogenic hydrogen target was placed in a vacuum scattering chamber located on the rotation axis of the spectrometers (center of fig. 1.2).

Since in the elastic scattering process the final energy of the electron E' and the scattering angle are related by eq. (1.14)

$$E'(\theta) = \frac{E}{1 + E/M(1 - \cos\theta)} \tag{1.29}$$

being E the initial energy of the electron and M the proton mass, electrons elastically scattered (without the emission of any photons) are identified considering only those events where the difference between the detected energy E'_{exp} and the energy calculated from the detected scattering angle $E'(\theta_{\mathrm{exp}})$ is near to zero.

Two strategies were adopted to obtain the form factors from the measurement of the elastic cross section. The first is the classical “Rosenbluth separation” [24]: the Rosenbluth cross section in eq. (1.21) can be written in the form

$$\frac{\mathrm{d}\sigma}{\mathrm{d}\Omega}^{\mathrm{Ros}} = \frac{\mathrm{d}\sigma}{\mathrm{d}\Omega}^{\mathrm{Mott}*} \cdot \left[G_E^2(Q^2) + \frac{\tau}{\xi} G_M^2(Q^2) \right] \frac{1}{1+\tau} \tag{1.30}$$

where the label “Mott*” indicates the recoiling Mott cross section and ξ denotes the polarization of the virtual photon

$$\xi = \left[1 + 2(1+\tau)\tan^2\tfrac{\theta}{2}\right]^{-1} \tag{1.31}$$

The method takes advantage of the linear dependence in ξ of form factors in the reduced cross section σ_R which can be written as

$$\sigma_R = \frac{\left(\frac{\mathrm{d}\sigma}{\mathrm{d}\Omega}{}^{\mathrm{Ros}}_{\mathrm{exp}}\right)}{\left(\frac{\mathrm{d}\sigma}{\mathrm{d}\Omega}{}^{\mathrm{Mott}^*}\right)} \frac{\xi(1+\tau)}{\tau} = \frac{\xi}{\tau} G_E^2 + G_M^2 \tag{1.32}$$

Thus, for fixed values of Q^2 one can obtain the electric and magnetic form factors from a linear fit in ξ. This method is model independent to the first order in the photon propagator, but requires data at a constant value of Q^2 for a range large enough of ξ and given the finite angular range of the three spectrometers, the covered kinematical range is limited. This problem was solved by the A1 collaboration with a direct fit of the models of the form factors to the measured cross section (“super-Rosenbluth separation”). This procedure allows all the Q^2 and ξ to contribute in the fit, without the need to project Q^2 on a specific value, but introduces a dependence from the model. To avoid a large model-dependence, a wide range of models was used and their outcomes were compared: generally good values of χ^2/DOF were achieved with flexible forms such as polynomials or splines, but not with inflexible forms (*e.g.* dipoles or double-dipoles).

The results of the direct fits were generally compatible with the results obtained from the Rosenbluth separation method, but this latter method was found to be more sensitive to systematic deviations being therefore a worse estimator of the electric and magnetic form factor. The results of the spline model for $G_E(Q^2)$ are shown in fig. 1.4.

The use of polynomials and splines led to slightly different values in the extracted charge radius, resulting in an additional uncertainty term (group) in the average value

$$r_\mathrm{p} = \sqrt{\langle r_\mathrm{p}^2 \rangle} = 0.879 \pm 0.005_{\mathrm{stat}} \pm 0.004_{\mathrm{sys}} \pm 0.002_{\mathrm{model}} \pm 0.004_{\mathrm{group}} \mathrm{fm} \tag{1.33}$$

In a recent review [25], Pohl et al. listed some of the issues of this kind of measurements. In particular the role of the two photon exchange (TPE) is controversial: in the data presented by Bernauer this contribution was initially neglected, and the later application of the TPE correction after a comment by Arrington showed a variation of the extracted proton radius compatible with the previously associated error [26, 27].

In order to shed some light on the role of the exchange of two photons, high precision experiments are under way to determine observables that depend on the two-photon exchange, such as the differences between the e^+–p and e^-–p cross section.

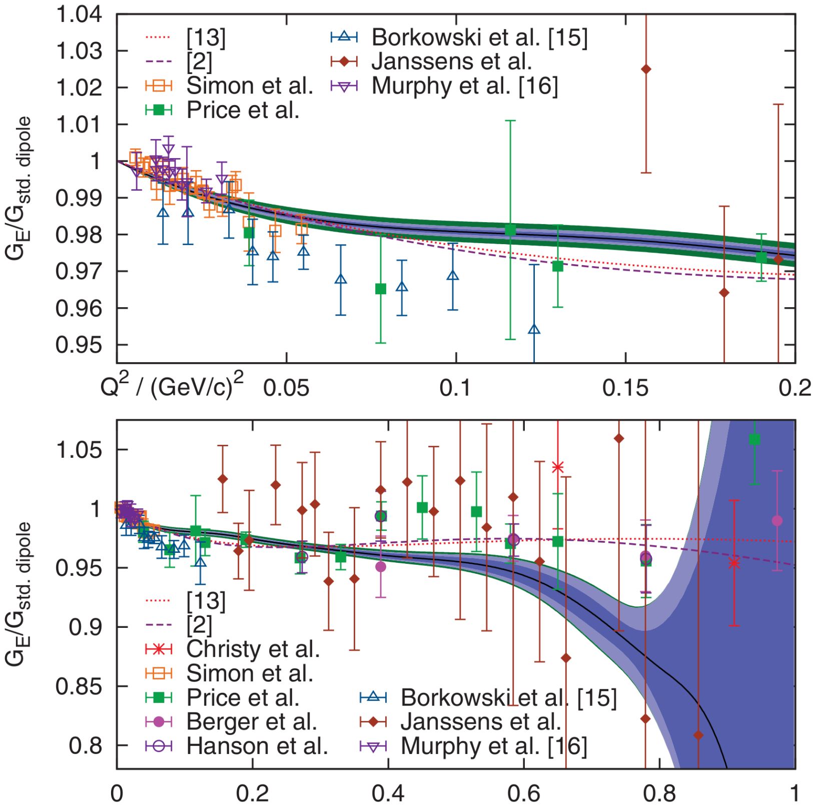

Figure 1.4: The electric form factor $G_E(Q^2)$ normalized to the standard dipole (eq. (1.25)) as a function of Q^2, as obtained by the A1 collaboration. Black line: best fit to the data; blue area: statistical 68% pointwise confidence bound; light blue area: experimental systematic error; green outer band: variation of the Coulomb correction by ±50% [21].

1.2.2 *Proton charge radius from atomic spectroscopy measurements in hydrogen*

Spectroscopy of atomic hydrogen has been fundamental for the development of modern physics since the dawn of quantum theory more than a century ago. It was the discovery of deviations of the energy levels from the ones expected from the Dirac equation that first showed effects of QED beyond the Dirac equation. Since the observation of this effect in 1947 by Lamb and Retherford [28], QED has reached an impressive level of accuracy in the calculation of the hydrogen levels: as an example, the $1S$–$2S$ transition in now known with an associated error of four parts in 10^{15} [29]. With such a level of accuracy, QED can be tested comparing the results of the calculation of the hydrogen levels with the experimental values.

However, the precision of the QED test is limited by two parameters that enter in the calculation: the Rydberg constant R_∞ and the root-mean-squared radius of the proton. Thus, one can either obtain these parameters in different ways and use them to test QED with experimental measurements of the hydrogen levels, or *extract* them from the measurements of the energy levels.

To achieve this goal, besides a great experimental precision, an accurate description of the energy levels in the range of fourteen orders of magnitude is needed and is thus necessary to keep into account the many corrections to the Dirac energies at this level of precision.

In this section, a brief description of the calculation of the hydrogen energy levels is given following the path marked by Antognini in [30]. For more detailed calculations see for instance [31]. The energy eigenvalue of a solution of the Dirac equation for a static Coulomb source is

$$E_{nj} = mc^2 f(n,j) \tag{1.34}$$

where m is the mass of the electron and

$$f(n,j) = \left[1 + \frac{(Z\alpha)^2}{\left(n - j - \frac{1}{2} + \sqrt{(j+\frac{1}{2})^2 - (Z\alpha)^2}\right)^2}\right]^{-\frac{1}{2}} \tag{1.35}$$

with n the principal quantum number and j the sum of the orbital and spin angular momentum of the electron. States with the same principal quantum number n but different angular momentum are thus split into n components of the fine structure. Considering the effect of the finite mass of the nucleon and the hyperfine splitting E^{hfs}_{njlF}, the total energy of the electron in the level characterized by the (n,j,l,F) quantum numbers (F being the total angular momentum of the proton–electron system) can be expressed as

$$\begin{aligned} E^{\mathrm{tot}}_{njlF} = mc^2 + Mc^2 + [f(n,j)-1]m_{\mathrm{r}}c^2 - \\ -[f(n,j)-1]^2 \frac{m_{\mathrm{r}}^2 c^2}{2(m+M)} + L_{njl} + E^{\mathrm{hfs}}_{njlF} \end{aligned} \tag{1.36}$$

where m_r is the reduced mass $(mM)/(m+M) \simeq 0.9995 \cdot m$ for hydrogen (M is the proton mass) and Z the atomic number of the nucleus. To give an idea of the magnitude of the different contributions in the transition $1S$–$2S$, one can notice that the first two terms always cancel out when measuring transition energies; the third term contributes about 2.5×10^3 THz, while the fourth term (recoil) contributes ≈ 22 MHz. The hyperfine splitting of the $1S$ state is $E^{\mathrm{tot}}_{1S(F=1)} - E^{\mathrm{tot}}_{1S(F=0)} \simeq 1420$ MHz. The term L_{njl} indicates the *Lamb shift*, which is defined as the sum of any corrections to the energy level predicted by the Dirac equation (partially corrected for the finite nucleus mass). The difference of the Lamb shift of the state $1S$ and $2S$ is $L_{1S} - L_{2S} \simeq 8 - 1 = 7$ GHz.

The Lamb shift arises from QED corrections to the energy levels that can be written in the form of a power series in three small dimensionless parameters α, $Z\alpha$ and m/M. Although these parameters enter in the calculations in a non-perturbative way, nevertheless it is convenient to use them to set the scale of the corrections magnitude.

The main sources of the corrections combined in the Lamb shift are usually classified in four groups, here listed in decreasing order of relevance:

RADIATIVE CORRECTIONS take into account pure QED effects like the electron self-energy and the vacuum polarization for an electron in a Coulomb potential of an infinitely heavy point-like nucleus. These contributions depend only on α and $Z\alpha$.

RECOIL CORRECTIONS describe corrections due to the finite mass of the nucleus that are not included in eq. (1.36) without considering any further QED correction. These contributions derive from the fact that the introduction of the reduced mass m_r alone cannot account for all the recoil corrections in a relativistic two-body system. Recoil corrections depend only on the mass ratio m/M and $Z\alpha$.

RADIATIVE–RECOIL CORRECTIONS concern the mixed recoil and radiative contributions such as recoil contributions with one or more photon loops in the fermion line. Given their “mixed” nature, these corrections depend simultaneously on m/M, α and $Z\alpha$.

NUCLEAR STRUCTURE CORRECTIONS are mainly due to the finite size of the nucleus. The smearing of the nucleus charge over a finite volume makes electrons experience a smaller attraction than in the case of a point-like nucleus. Another contribution related to the nuclear structure comes with the nucleus polarization which accounts for the nuclear excitation to virtual excited states.

Fortunately, the most of these contributions can be calculated independently one from the other, *e.g.* radiative corrections can be evaluated without taking into account the effect of the nuclear structure and vice-versa.

The main contribution to the Lamb shift in hydrogen comes from the electron self-energy (fig. 1.5a). These corrections are due to the emission and re-absorption of virtual photons by the electron that, as a result, appears with

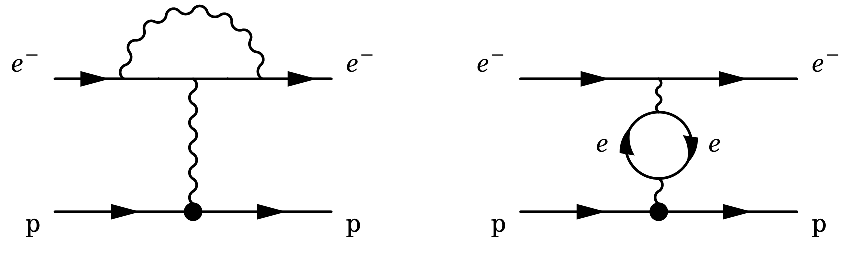

(a) electron self-energy (b) vacuum polarization

Figure 1.5: Feynman diagrams of the leading order contributions to the electron self-energy **(a)** and to the vacuum polarization **(b)**.

its charge spread over a finite volume instead of being point-like [31]. As it was shown in the previous section, the description of non-point-like particles requires the introduction of form factors ($F_1(Q^2)$ and $F_2(Q^2)$). The smearing of the electron charge makes the binding energy weaker than the one of a point-like electron, resulting in higher energy levels. Moreover, this effect is non-vanishing only at the source of the Coulomb potential, thus it influences in a different way energy levels with different angular momentum, splitting the energy levels with the same j but different orbital angular momentum [31]. Another consequence of this effect is the anomalous magnetic moment $(g-2)$ of the electron and the muon, firstly calculated by Schwinger in [32].

The Vacuum Polarization correction (fig. 1.5b) is a QED correction of the same order of the electron self-energy. It accounts for the creation of a fermion loop in the photon propagator that results in a modification of the Coulomb field. The electron surrounded by this polarization cloud sees a larger charge that makes the electromagnetic interaction stronger and the energy level smaller [31]. Numerically, Vacuum Polarization is much less relevant than the effect of the electron self-energy, but, as it will be shown in the next section, it plays an important role in muonic hydrogen.

On the other hand, the electric potential $V(r)$ of the extended nucleus differs from that of a point-like nucleus by [30]

$$\delta V(r) = V(r) - \left(-\frac{Z\alpha}{r}\right) \tag{1.37}$$

In the momentum space this perturbation takes the form

$$\delta V(\boldsymbol{q}) = \frac{4\pi Z\alpha}{\boldsymbol{q}^2}(1 - F_1(\boldsymbol{q})) \simeq \frac{2\pi Z\alpha}{3} r_\mathrm{p}^2 \tag{1.38}$$

where $F_1(\boldsymbol{q})$ is the Dirac form factor introduced in eq. (1.17). The resulting energy shift is

$$\Delta E = \langle\psi(r)|\delta V|\psi(r)\rangle = \frac{2\pi Z\alpha}{3} r_\mathrm{p}^2 |\psi(0)|^2 = \frac{m^2}{(\hbar/mc)^2}\frac{2}{3n^3}(Z\alpha)^4 r_\mathrm{p}^2 \delta_{l0} \tag{1.39}$$

being ψ the state vector of the electron [31].

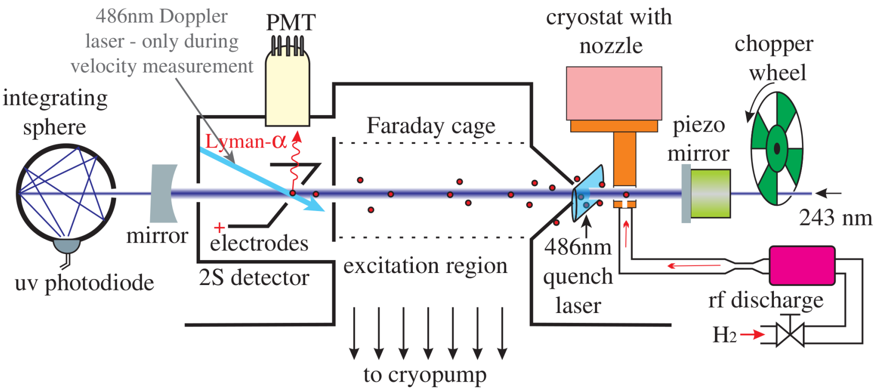
486nm Doppler laser - only during velocity measurement
PMT
cryostat with nozzle
chopper wheel
integrating sphere
Lyman-α
Faraday cage
piezo mirror
mirror
+
−
electrodes
243 nm
uv photodiode
2S detector
excitation region
486nm quench laser
rf discharge
H2
to cryopump

Figure 1.6: Scheme of the experimental set-up used for the measurement of the $1S$–$2S$ transition energy in [29].

To give an idea of the magnitude of the proton size contribution to the Lamb shift in the $1S$ state of hydrogen, this is

$$L_{1S} \simeq (8172000 + 1.5 \cdot r_\mathrm{p}^2)\ \mathrm{MHz} \tag{1.40}$$

with r_p^2 expressed in fm, for a contribution of $\sim 1.5 \times 10^{-4}$ [25]. However, since the nineties, the increase of experimental and theoretical accuracy makes hydrogen spectroscopy sensitive to the effects of the proton size.

To extract the Rydberg constant and the proton radius from such spectroscopic measurements, one needs at least two transition frequencies in hydrogen. Given this fact, the energy of the S-states in hydrogen can be approximated as

$$E(nS) \simeq -\frac{R_\infty}{n^2} + \frac{L_{1S}}{n^3} \tag{1.41}$$

where L_{1S} is the Lamb shift in the $1S$ state; typically one uses the $2S$–$8S, D$ or the $2S$–$12D$ transition to extract the Rydberg constant and the $1S$–$2S$ transition to determine the proton radius. This choice is motivated by the fact that for high n the Lamb shift contribution is smaller due to the n^{-3} scaling allowing an easier determination of the Rydberg constant, while the $1S$–$2S$ transition contains the maximal $1S$ Lamb shift and is therefore maximally sensitive to the proton radius [25].

For this kind of measurements an outstanding experimental accuracy is required. An example of the experimental strategy for the precise determination of the $1S$–$2S$ transition energy can be found in [29]. In this experiment, a beam of atomic hydrogen dissociated in a radio-frequency (RF) cavity was cooled to 5.8 K and was injected in a Faraday cage to avoid the interference of stray fields. Here the hydrogen atoms are excited from the $1S$ to the $2S$ state by two photons provided by an extended-cavity diode laser near 972 nm whose frequency was doubled twice within two resonant cavities to obtain the required UV light near 234 nm.

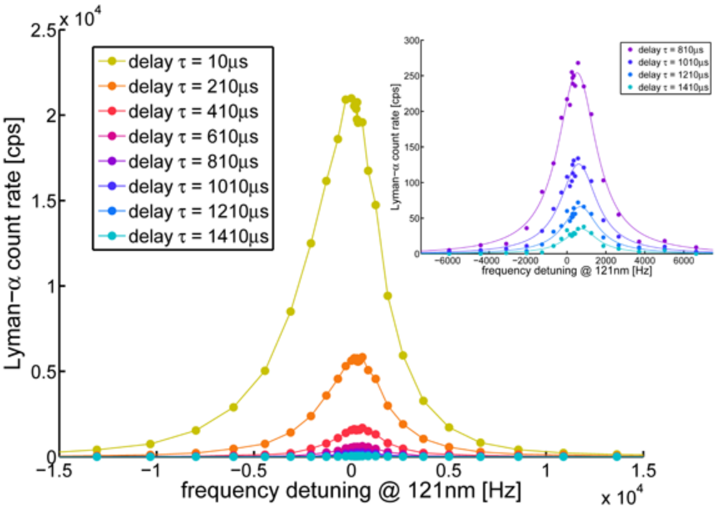

Figure 1.7: Photon count rate as a function of the frequency detuning for different values of the delay τ (from: `http://www2.mpq.mpg.de/~haensch/hydrogen/`).

In the scheme shown in fig. 1.6, hydrogen is excited by a co- and counter-propagating photon: the co-propagating photon is red-shifted because of the Doppler effect due to the velocity of the atoms, and the counter-propagating photon is blue-shifted of the same amount, cancelling the systematic Doppler effect at the first order.

For the detection, atoms in the long-lived $2S$ state are quenched via the $2P$ state by an electric field of 10 V/m. The $2P$ state decays quickly emitting a 121 nm photon which is detected by a PhotoMultiplier Tube.

The Lyman-α count rate for different delays τ is shown in fig. 1.7. The strong asymmetry in the $\tau = 10\,\mu\text{s}$ data is due to the second order Doppler effect which maps the maxwellian velocity distribution of the thermal atomic beam onto the spectral line. This asymmetry disappears at increasing delays. To correct this residual Doppler shift, the velocity distribution of the atoms was measured independently via the first-order Doppler effect on the $2S$–$4P$ one-photon transition.

With this procedure, a value of the transition frequency between the $1S$ and the $2S$ state with a fractional uncertainty of 4.2×10^{-15} was extracted [29].

Fig. 1.8 shows the different values of the proton radius r_{p} obtained by combining the $1S$–$2S$ transition and each of the other precisely measured transitions in hydrogen (blue dots). In addition, three values of r_{p} extracted directly from measurements of the $2P$–$2S$ transition are reported (green dots). The blue line and the light blue area are the average value and its uncertainty as calculated by CODATA. Fig. 1.9 shows the comparison of the average value of the proton radius obtained with spectroscopic measurements in hydrogen and the ones extracted from e^{-}–p elastic scattering experiments and world data analysis.

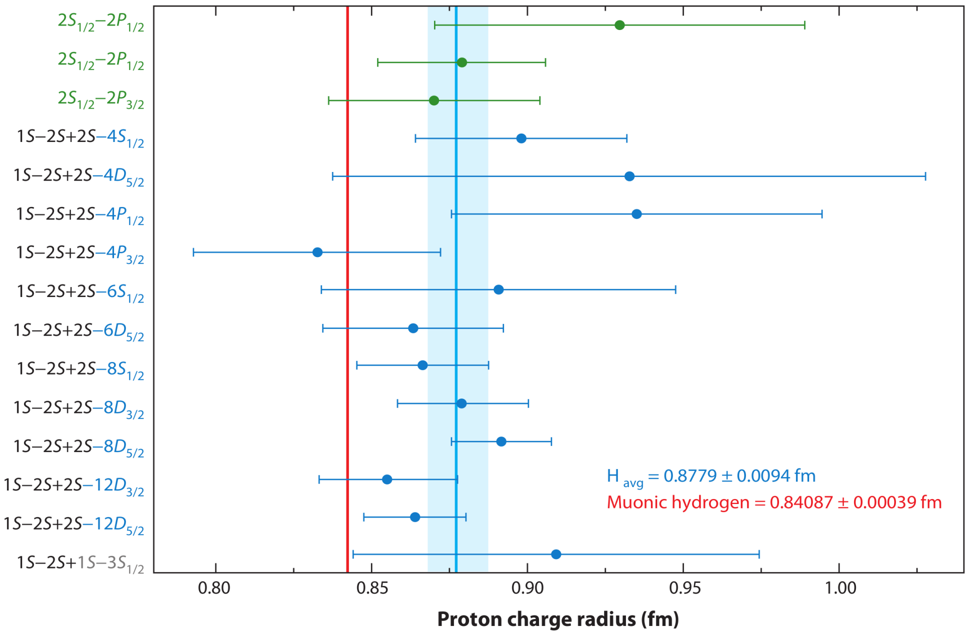

Figure 1.8: Proton charge radii r_p obtained from hydrogen spectroscopy [25]. The values of r_p can be extracted by the combined measurement of the $1S$–$2S$ [29] and $2S$–$8S,D/12D$ [33, 34] transitions. The value of r_p obtained from the Lamb shift in muonic hydrogen (sec. 1.2.3) is also shown in red.

1.2.3 *The proton radius puzzle: the Lamb Shift experiment*

As can be noticed from fig. 1.8 and 1.9, in the last twenty years the results on the proton charge radius obtained from e^-–p elastic scattering experiments and with spectroscopic measurements in hydrogen are fully compatible. The fact that compatible values of the proton radius were provided by two completely different experimental techniques was encouraging, but in 2010 a new value of the proton radius extracted by a measurement of the Lamb shift between the $2S^{F=1}_{1/2}$ and the $2P^{F=2}_{3/2}$ states in muonic hydrogen heavily questioned the results obtained until then.

The determination of the proton radius with muonic hydrogen was originally motivated by the need to improve the accuracy of this parameter ($\approx 0.58\%$ in the last CODATA review) to enhance the precision of the test on bound state QED, that was (and still is) limited by the large ($\sim 1\%$) uncertainty on the proton radius obtained by the only independent method, which is e^-–p scattering.

A r_p determination from an independent source was therefore highly desired. Muonic hydrogen is a good system to study the proton structure since, given the larger mass of the muon, the Bohr radius for μp is about 200 times smaller. The ratio between the reduced masses of ordinary and muonic hydrogen is ≈ 186, thus the binding energies of μp are 186 times larger than the ones of ordinary hydrogen, falling in the keV region.

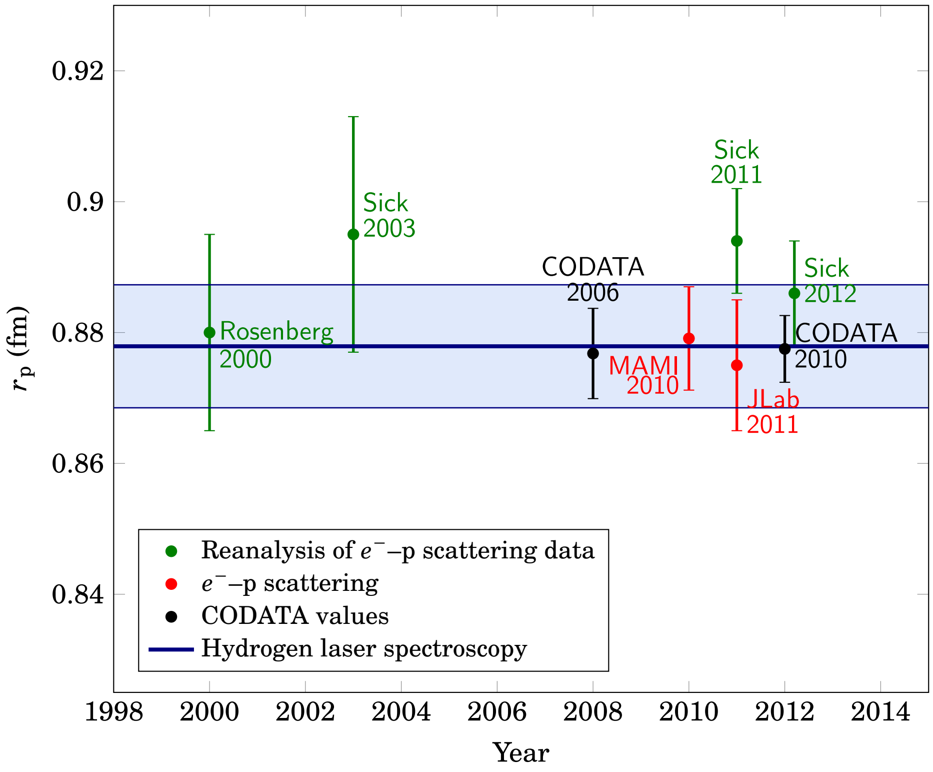

Figure 1.9: Recent "history" of the proton charge radius. Only the recent elastic scattering experiment at MAMI [21] and JLab [35] are reported (red). The green dots refers to world data analysis (from left to right [36], [37], [38], [39]), while the blue line is the average value of the proton radius extracted from laser spectroscopy measurements in hydrogen with its uncertainty (fig. 1.8). Finally, black dots indicate the value presented in the CODATA review of 2006 [40] and 2010 [6].

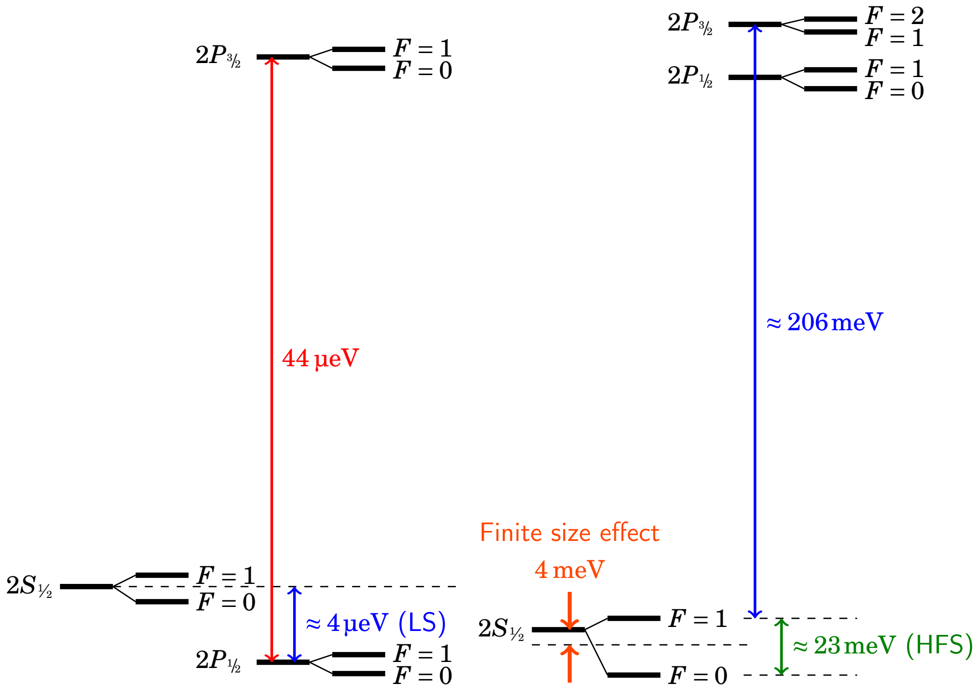
$2P_{3/2}$
$F = 1$
$F = 0$
44 µeV
$2S_{1/2}$
$F = 1$
$F = 0$
≈ 4 µeV (LS)
$2P_{1/2}$
$F = 1$
$F = 0$
$2P_{3/2}$
$F = 2$
$F = 1$
$2P_{1/2}$
$F = 1$
$F = 0$
≈ 206 meV
Finite size effect
4 meV
$2S_{1/2}$
$F = 1$
$F = 0$
≈ 23 meV (HFS)

(a) ordinary hydrogen **(b)** muonic hydrogen

Figure 1.10: Comparison of the $n = 2$ energy levels in ordinary hydrogen (left) and in muonic hydrogen (right). Note the different energy scale. The 4 µeV energy difference between the $2S_{1/2}$ and the $2P_{1/2}$ energy levels in ep was discovered by Lamb and Retherford in 1947 [28] and is mainly due to the electron-self energy correction. In the μp atom the contribution of the Lamb Shift (LS) is such that the $2S_{1/2}$ state lies ~ 200 meV below the $2P_{1/2}$ state because of the dominant vacuum polarization effect.

In fig. 1.10 the remarkable difference between ep and μp $2S$–$2P$ states is depicted. The main contribution to the ep($2S$) Lamb shift is the electron self-energy, about 1 GHz ($\approx 4\,\mu\text{eV}$), which affects the binding energy of the $2S$ state for 1 ppm, while the vacuum polarization effect is 40 times smaller. In contrast, the μp($2S$) Lamb shift is dominated by vacuum polarization, that contributes as -206 meV and shifts the $2S$ level well below the $2P_{1/2,3/2}$ states. The effect of the muon self-energy is about 300 times smaller (≈ 0.7 meV) [41].

The S states of muonic hydrogen overlap considerably with the nuclear volume, and as a consequence their energy is much more sensitive to the proton structure. The corrections due to the finite size of the proton represent about 1.8% of the Lamb shift for $n = 2$, about two orders of magnitude more than in the ep atom. Thus, the measurement of the $2S$–$2P$ Lamb shift in muonic hydrogen is an excellent tool to investigate the proton structure.

Such a measurement was performed at the proton accelerator of the Paul Scherrer Institute (PSI) in Switzerland, where a beam line dedicated to low-energy muons (with kinetic energy in the 3 keV–6 keV range) was built.

The beam line delivers about ~ 600 muons/s that must be detected before entering the target vessel to trigger the laser system and the acquisition; this is done by two transmission muon detectors consisting of two stacks of ultrathin carbon foils separated by ~ 35 cm able to detect muons with an efficiency of 80% and 70% respectively using the electrons ejected by the carbon foils when crossed by muons.

About one half of the muons are stopped in a 20 cm long vessel filled with 1 mbar H_2 [25] where they form highly excited ($n \approx 14$) μp atoms.

Most of these atoms de-excite quickly to the $1S$ ground state, but about 1% populates the long-lived $2S$ state. About 0.9 µs after the passage of the muon through the transmission detector, a short laser pulse (75 ns) with a wavelength tunable around 6 µm enters a non-resonant multipass mirror cavity surrounding the gas target, inducing a $2S \rightarrow 2P$ transition on resonance. The estimated laser fluence is $\sim 6\,\text{mJ/cm}^2$, which results in a transition probability of $\sim 30\%$ at the center of the resonance [25]. The de-excitation from the $2P$ to the ground state is almost immediate ($\tau_{2P} = 8.5\,\text{ps}$) and takes place via the emission of a 1.9 keV X-ray that was detected using 20 large-area ($14 \times 14\,\text{mm}^2$) avalanche photo-diodes (LAAPDs) [42], whose typical time and energy resolution at 1.9 keV are 35 ns and 25%.

A scan on the laser wavelength was performed. For every laser frequency, the K_α X-ray time spectrum was recorded. Fig. 1.11 shows two examples of such a time spectrum: the large “prompt” peak contains 99% of the muons that did not form the metastable μp($2S$) state and de-excite directly to the ground state, while the 75 ns-long laser time window, where the K_α events are expected, is indicated in red for the on-resonance and off-resonance case.

A resonance curve, shown in fig. 1.12, was obtained by plotting the number of K_α events recorded in the laser time window normalized to the number of prompt events as a function of the laser frequency. The resonance was fitted using a Lorenzian function over a flat background obtaining a value of $\chi^2 =$

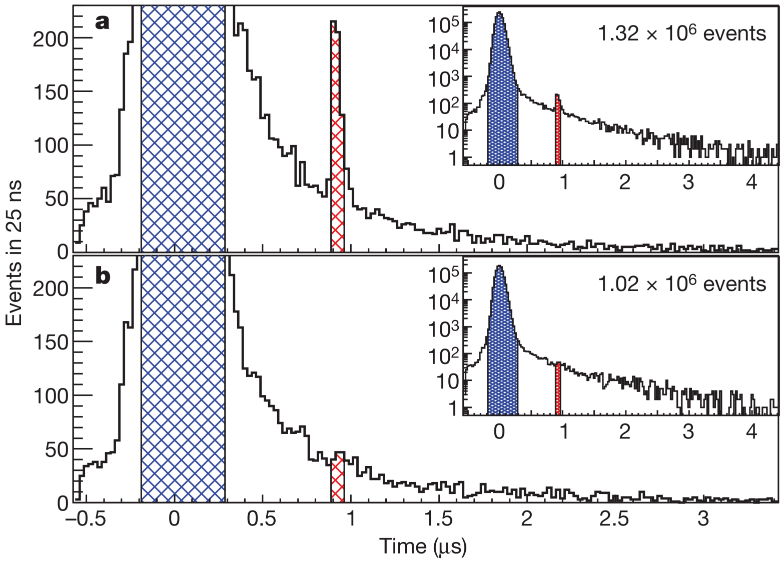

Figure 1.11: Integrated X-ray spectrum recorded on (a) and off (b) resonance. The laser time window is coloured in red, while the prompt peak is indicated in blue [16].

28.1 for 28 degrees of freedom and the centroid position for the $2S_{1/2}^{F=1}$–$2P_{3/2}^{F=2}$ transition at 49 881.88(76) GHz.

The corresponding transition energy is $\Delta\tilde{E} = 206.2949(32)\,\mathrm{meV}$. The predicted value of the $2S_{1/2}^{F=1}$–$2P_{3/2}^{F=2}$ energy difference, calculated as the sum of the radiative, recoil and proton structure contributions, was

$$\Delta\tilde{E} = 209.9779(49) - 5.2262 r_\mathrm{p}^2 + 0.0347 r_\mathrm{p}^3 \tag{1.42}$$

(with r_p expressed in fm) and from the experimental measurement of the transition energy, a value of $r_\mathrm{p} = 0.841\,84(67)\,\mathrm{fm}$ was found.

Further measurements of the $2S_{1/2}^{F=0}$–$2P_{3/2}^{F=1}$ transition energy and a re-evaluation of the $2S_{1/2}^{F=1}$–$2P_{3/2}^{F=2}$ energy difference in μp atoms were published in 2013 [43], presenting a value of $r_\mathrm{p} = 0.840\,87(39)\,\mathrm{fm}$ compatible with the previous measurement in muonic hydrogen, but 7σ distant from the CODATA-2010 reference value.

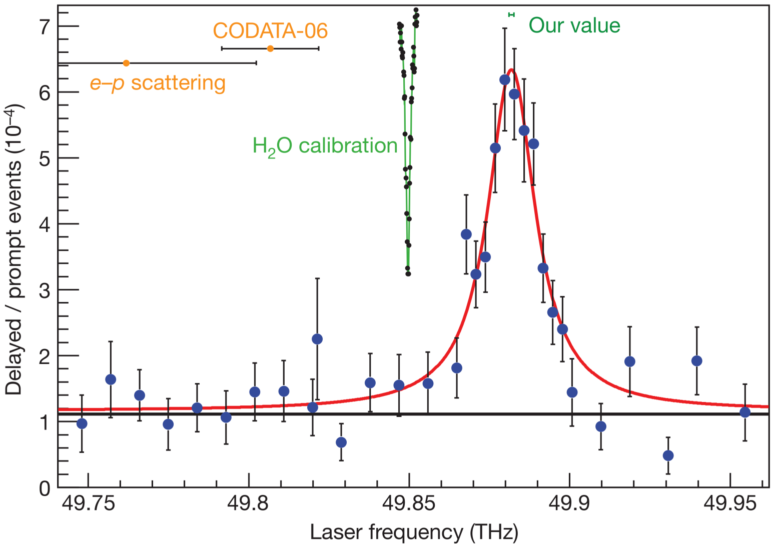

Figure 1.12: The ratio of the delayed/prompt events (blue dots) as a function of the laser frequency, forms a resonance peak, fitted by a Lorenzian distribution over a constant background. The prediction of the transition energy obtained using the value of r_{p} from CODATA–2006 and e^{-}–p scattering is shown for comparison. The calibration of the laser system with the absorption spectra of water vapour is also shown (black dots, green line) [16].

CHAPTER 2

CONCEPT OF THE FAMU EXPERIMENT

The unexpected results of the Lamb Shift experiment at PSI on the proton charge radius [16] immediately raised great sensation in the scientific community. The huge discrepancy between the value obtained from the Lamb shift in muonic hydrogen and the one calculated by CODATA has not been explained yet although several hypotheses have been made since the first days after the publication of the results in 2010.

Pohl et al., in their review on the proton radius puzzle [25], listed some possible origins of this disagreement. The first possibility is that electronic hydrogen experiments are almost, but not quite, as accurate as stated. In particular, the correlation coefficient between the Rydberg constant R_∞ and the proton radius in the 2010 CODATA adjustment is 0.984, therefore any new determination of R_∞ at a level of a few parts in 10^{12} would help in shedding new light on the discrepancy between ordinary and muonic hydrogen results [25]. A number of projects for new high-precision spectroscopic measurements in hydrogen and hydrogen-like atoms are under way in this sense (see [25] for a brief review of these experiments). Also in the field of elastic e^-–p scattering, new experiments at low-Q^2 are in programme [44].

Another possibility is that the QED calculations of the hydrogen energy levels are not precise as stated. This is quite unlikely, given the fact that these effects have been calculated independently by many groups using different approaches obtaining compatible results, but it is always possible that something in the theory is missing. In particular, the proton polarizability effect on the two-photon exchange term is still affected by a relatively large theoretical uncertainty that would be nice to reduce.

The most intriguing hypothesis is that the electron and the muon interact differently with the proton. This difference would require physics beyond the Standard Model that violates the principle of lepton universality. This possibility attracts discrete interest since the recent measurements of the anomalous magnetic moment of the muons ($a_\mu = (g_\mu - 2)/2$) shows a discrepancy with the theory of $\Delta a_\mu = a_\mu^{\mathrm{exp}} - a_\mu^{\mathrm{th}} = (288 \pm 80) \times 10^{-11}$, that, although very small, has a statistical significance of 3.6σ [45]. This difference, as well as the proton radius puzzle, could be due to a new kind of interaction that acts differently on the muon and on the electron. In addition, new gauge forces mediated by particles at the MeV–GeV scale could be dark matter candidates [46, 47]. Very recently also a possible solution based on quantum gravity has been proposed [48].

The hypothesis of a different behaviour of the electron and the muon interacting with the proton needs to be carefully tested. For this reason, a μ–p elastic scattering experiment at PSI has been proposed to shed some light on the role of the two-photon exchange contribution and test theories beyond the Standard Model [49]. Another way to test possible differences in the e^-–p and μ–p interaction is the comparison of another characteristic of the proton, the *Zemach radius* R_p, that can be obtained from the measurement of the hyperfine splitting (HFS) in ordinary and muonic hydrogen.

The extraction of the proton Zemach radius from the measurement of HFS in the ground state of muonic hydrogen is the goal of the FAMU (*Fisica Atomi MUonici*, Muonic Atoms Physics) collaboration and this chapter is devoted to the description of the experimental method developed for this measurement.

The physics behind the hyperfine splitting and the role of the proton structure in this interaction will be described in sec. 2.1. In sec. 2.2 the motivation for a precise measurement of the hyperfine splitting of the ground state of muonic hydrogen will be briefly exposed.

The experimental method proposed for this measurements is described in sec. 2.3: some of its key aspects will be examined in the following sections.

2.1 PHYSICAL ORIGIN OF THE HYPERFINE SPLITTING

The hyperfine splitting of the atomic energy levels is due to the interaction between the electron and nucleus magnetic dipoles. As already outlined in sec. 1.1, from the relativistic theory of Dirac, a spin-$\frac{1}{2}$ particle with mass m has a magnetic moment

$$\boldsymbol{\mu} = \frac{g}{2}\frac{e}{m}\boldsymbol{s} \tag{2.1}$$

where $g \approx 2$ is the gyromagnetic ratio and $\boldsymbol{s}$ is the spin of the particle. The magnetic moment of the proton is much smaller than the one of the electron given the m^{-1} mass dependence, but its effect is still relevant. From classical electrodynamics, a magnetic dipole generates a magnetic field [50]

$$\boldsymbol{B}(\boldsymbol{r}) = \frac{1}{|\boldsymbol{r}^3|}\left[3(\boldsymbol{\mu}\cdot\hat{\boldsymbol{r}})\hat{\boldsymbol{r}} - \boldsymbol{\mu}\right] + \frac{8\pi}{3}\boldsymbol{\mu}\delta^3(\boldsymbol{r}) \tag{2.2}$$

The Hamiltonian for the electron in the magnetic field due to the proton magnetic moment is

$$H_\mathrm{hfs} = \frac{2\mu_\mathrm{p}e^2}{2Mm}\frac{3(\boldsymbol{s}_\mathrm{p}\cdot\hat{\boldsymbol{r}})(\boldsymbol{s}_e\cdot\hat{\boldsymbol{r}}) - \boldsymbol{s}_\mathrm{p}\cdot\boldsymbol{s}_e}{|\boldsymbol{r}|^3} + \frac{8\pi\mu_\mathrm{p}e^2}{3Mm}\boldsymbol{s}_\mathrm{p}\cdot\boldsymbol{s}_e\delta^3(\boldsymbol{r}) \tag{2.3}$$

According to the perturbation theory, the first order correction to the energy is the expectation value of the perturbative hamiltonian H_hfs. When considering the S states, which are spherically symmetric, the first term in eq. (2.3) vanishes, leaving for the hydrogen generic nS state

$$E^{(1)}_{\text{hfs}} = \frac{8\pi}{3}\mu_{\text{p}}\frac{e^2}{Mm}\langle \boldsymbol{s}_{\text{p}} \cdot \boldsymbol{s}_e\rangle |\psi(0)|^2 = \frac{8}{3n^3a_0^3}\mu_{\text{p}}\frac{e^2}{Mm}\langle \boldsymbol{s}_{\text{p}} \cdot \boldsymbol{s}_e\rangle \tag{2.4}$$

where a_0 is the Bohr radius (calculated using the reduced mass of the proton–lepton system). The scalar product between the proton and electron spin can be written as

$$\boldsymbol{s}_{\text{p}} \cdot \boldsymbol{s}_e = \tfrac{1}{2}\left(S^2 - s_{\text{p}}^2 - s_e^2\right) \tag{2.5}$$

being $\boldsymbol{S}$ the *total* spin operator $\boldsymbol{S} = \boldsymbol{s}_{\text{p}} + \boldsymbol{s}_e$ and S^2 the squared total spin operator. Both the electron and the proton are spin-$\frac{1}{2}$ particles; thus the squared-spin eigenvalue is $s_e^2 = s_{\text{p}}^2 = \frac{1}{2}(1+\frac{1}{2})\hbar^2 = \frac{3}{4}\hbar^2$. In the triplet state, when the spins are "parallel", the total spin is 1 and hence $S^2 = 2\hbar^2$, while in the singlet state ("anti-parallel" spins) the total spin is 0 and $S^2 = 0$.

This spin–spin coupling breaks the spin-degeneracy of the energy levels lifting the triplet configuration and depressing the singlet one. The resulting energy difference is

$$\Delta E_n^{\text{hfs}(1)} = \frac{8\alpha^4}{3n^3}\mu_{\text{p}}\frac{m^2M^2}{(m+M)^3} \tag{2.6}$$

which, for the ground state of ordinary hydrogen, corresponds to a frequency of about 1420 MHz (or, equivalently, to a wavelength of 21 cm) that is of great importance in radio-astronomy.

As for the case of the Lamb shift (sec. 1.2.3), QED provides the framework for the calculation of many corrections to the value in eq. (2.6) derived by Fermi in 1930 [51]. Once again the corrections are expressed in an expansion of the three terms α, $Z\alpha$ and m/M and are typically factorized as

$$\Delta E_n^{\text{hfs}} = E_n^{\text{F}}\left(1 + \delta^{\text{Dirac}} + \delta^{\text{QED}} + \delta^{\text{structure}}\right) \tag{2.7}$$

where E_n^{F} is the $\Delta E_n^{\text{hfs}(1)}$ in eq. (2.6) also known as Fermi splitting, while the δ terms refer to the relativistic, QED and proton structure corrections respectively (note that these effects cannot be treated separately at higher order). Without going too deep into the details, these contributions can be summarized as follows:

RELATIVISTIC CORRECTION δ^{Dirac}

Purely relativistic corrections are the simplest adjustments to hyperfine splitting. In the same way in which the relativistic corrections to the fine strucutre of the hydrogen atom are basically an expansion of the solution of the Dirac equation (eq. (1.34)) in series of $(Z\alpha)^2$, the relativistic corrections to the Fermi splitting consists of a power-series expansion of the solution of the relativistic problem. As found by Breit [52], the hyperfine splitting of an energy level for a generic nS state is

$$\Delta_{nS}^{\text{Br}} = \frac{1 + 2\sqrt{1 - \frac{(Z\alpha)^2}{N^2}}}{N^3\gamma(4\gamma^2 - 1)}E_n^{\text{F}} \tag{2.8}$$

where $N = \sqrt{n^2 - 2(Z\alpha)^2(n-1)/(1+\gamma)}$ and $\gamma = \sqrt{1-(Z\alpha)^2}$. The expansion of this expression in terms of $(Z\alpha)$ for the hydrogen ground state gives

$$\Delta_{1S}^{\mathrm{Br}} = \frac{E_1^{\mathrm{F}}}{\sqrt{1-(Z\alpha)^2}\cdot\left(2\sqrt{1-(Z\alpha)^2}-1\right)} = \left[1+\frac{3}{2}(Z\alpha)^2+\frac{17}{8}(Z\alpha)^4+\ldots\right]E_1^{\mathrm{F}} \tag{2.9}$$

The δ^{Dirac} correction for the hydrogen ground state is thus

$$\delta^{\mathrm{Dirac}} = \frac{\Delta_{1S}^{\mathrm{Br}} - E_1^{\mathrm{F}}}{E_1^{\mathrm{F}}} = \left[\frac{3}{2}(Z\alpha)^2+\frac{17}{8}(Z\alpha)^4+\ldots\right] \tag{2.10}$$

QED CORRECTIONS δ^{QED}

The leading radiative correction in the hydrogen HFS is due to the anomalous magnetic moment of the electron a_e that was mentioned in sec. 1.2.2 as an effect of the electron self-energy (fig. 1.5a). The first calculation of this effect is due to Schwinger [32], and further contributions were included by Sommerfield [53] and Petermann [54] in 1957. The current value of the electron anomalous magnetic moment is $a_e = (1159.652\,180\,76 \pm 0.000\,000\,27)\times 10^{-6}$ [6]. Other QED corrections involve many complex diagrams that require the full employment of QED to be evaluated. Up to terms of order α^3, δ^{QED} is given by [55]

$$\delta^{\mathrm{QED}} = a_e + \alpha^2\left(\ln 2 - \frac{5}{2}\right) - \frac{8\alpha^3}{3\pi}\ln\alpha\left(\ln\alpha - \ln 4 + \frac{281}{480}\right) + 18.984\cdot\frac{\alpha^3}{\pi}+\ldots \tag{2.11}$$

STRUCTURE CORRECTIONS $\delta^{\mathrm{structure}}$

As in the case of the Lamb shift, the effects of the composite structure of the proton on the hyperfine splitting must be taken into account. In order to separate the different contributions, structure corrections are often put in the form [56]

$$\delta^{\mathrm{structure}} = \delta^{\mathrm{pol}} + \delta^{\mathrm{rec}} + \delta^{\mathrm{vp}} + \delta^{\mathrm{weak}} + \delta^{\mathrm{Z}} \tag{2.12}$$

where the different δ terms refer to the proton polarizability, recoil (and radiative-recoil), hadronic and muonic vacuum polarization, weak interaction and finite size corrections respectively. Polarizability and recoil corrections were already introduced in sec. 1.2.2 (for the specific case of HFS see [31]), while the contribution for muonic and hadronic vacuum polarization is due (at the leading order) to the muon and hadron loops in the photon propagator in fig. 1.5b. The weak interaction plays a small role in the hyperfine separation with a Z^0 exchange between the proton and the bound lepton [31, 57].

The last term is relative to the finite size of the proton. The main term in this contribution was calculated by Zemach in 1956 [58] without the need of a field theory treatment but starting from intuitively and reasonable assumptions. The main Fermi contribution to hyperfine splitting (eq. (2.4)) considers the proton as a point-like particle, so the interaction between the proton and electron magnetic dipole takes place at the position of the proton, thus involving the squared Schrödinger wave function at the origin ($|\psi(0)|^2$). However, the proton has a finite size, and the nuclear magnetic moment is distributed over a finite region according to a magnetic moment density distribution $\rho_\mathrm{M}(\boldsymbol{r})$. This effect can be taken into account with the obvious substitution

$$|\psi(0)|^2 \to \int \mathrm{d}^3\boldsymbol{r}\rho_\mathrm{M}(\boldsymbol{r})|\psi(\boldsymbol{r})|^2 \tag{2.13}$$

in eq. (2.4). Hence, the correction to hyperfine splitting due to the proton size depends on the behaviour of the bound-state wave function close to the origin. As shown by Zemach [58], near a distributed source of electric field (described by the charge density ρ_E), given the $\exp(-Z\alpha m_\mathrm{r} r)$ dependence, the wave function can be approximated as

$$\psi(r) \approx \psi(0)\left[1 - m_\mathrm{r} Z\alpha \int \mathrm{d}^3\boldsymbol{r}'|\boldsymbol{r}-\boldsymbol{r}'|\rho_\mathrm{E}(\boldsymbol{r}')\right] \tag{2.14}$$

Inserting this expression of $\psi(\boldsymbol{r})$ in eq. (2.13) one can find

$$|\psi(0)|^2 \to |\psi(0)|^2\left[1 - 2m_\mathrm{r} Z\alpha \int \mathrm{d}^3\boldsymbol{r}\rho_\mathrm{M}(\boldsymbol{r}) \int \mathrm{d}^3\boldsymbol{r}'|\boldsymbol{r}-\boldsymbol{r}'|\rho_\mathrm{E}(\boldsymbol{r}')\right] \tag{2.15}$$

The last expression can be simplified by the introduction of an electromagnetic distribution function $f_\mathrm{EM}(\boldsymbol{r})$ defined as the convolution of the electric and magnetic distributions

$$f_\mathrm{EM}(\boldsymbol{r}) = \int \mathrm{d}^3\boldsymbol{s}\rho_\mathrm{E}(\boldsymbol{r}-\boldsymbol{s})\rho_\mathrm{M}(\boldsymbol{r}) \tag{2.16}$$

The Zemach correction to the hyperfine splitting then becomes

$$\delta^\mathrm{Z} = -2(Z\alpha)m_\mathrm{r}R_\mathrm{p} \tag{2.17}$$

where R_p is the first moment of $f_\mathrm{EM}(\boldsymbol{r})$

$$R_\mathrm{p} = \int |\boldsymbol{r}| f_\mathrm{EM}(\boldsymbol{r})\mathrm{d}^3\boldsymbol{r} \tag{2.18}$$

and is known as *Zemach radius*.

In the momentum space, the expression of the Zemach radius can be put in the form [59]

$$R_\mathrm{p} = -\frac{4}{\pi}\int \frac{\mathrm{d}Q}{Q^2}\left[\frac{G_M(Q^2)}{\mu_\mathrm{p}}G_E(Q^2) - 1\right] \tag{2.19}$$

where G_M and G_E are the magnetic and electric form factor introduced in sec. 1.2.1. The radiative corrections to δ^Z have been calculated in [60].

E_1^{F} (MHz)	1418.84008(2)
δ^{QED}	0.00105621(1)
δ^{Dirac}	0.00007988
$\delta^{\mathrm{ps}\dagger}$	−0.00004011(61)
δ^{rec}	0.00000597(6)
δ^{pol}	0.0000014(6)
δ^{vp}	0.00000008(2)
δ^{weak}	0.00000006
$E_1^{\mathrm{hfs(th)}}$ (MHz)	1420.4057(12)
$E_1^{\mathrm{hfs(exp)}}$ (MHz)	1420.405751767(1)

Table 2.1: Numerical values for the various corrections to the hyperfine splitting in hydrogen ([56] and references therein).
† δ^{ps} indicates the proton size correction, that Volotka et al. evaluated to be $\delta^{\mathrm{ps}} = 1.0154(2)\delta^{\mathrm{Z}} + 1.4 \times 10^{-8}$.

2.2 MOTIVATION FOR THE MEASUREMENT OF THE HYPERFINE SPLITTING OF THE GROUND STATE IN MUONIC HYDROGEN

As in the case of the Lamb shift, the hyperfine splitting of the ground state of ordinary and muonic hydrogen shows very different characteristics. An example of the calculated value of the HFS for hydrogen as a result of the many corrections presented in the previous section is shown in tab. 2.1 [56].

The experimental value of the hyperfine splitting ($E_1^{\mathrm{hfs(exp)}}$ in tab. 2.1) is known with a relative uncertainty smaller than 10^{-12}, being one of the most accurate measured quantities, while the theoretical predictions are less accurate [55]. This is partially due to the increasing difficulties in the calculation of higher order terms in the perturbative expansion in powers of α and $(Z\alpha)$ and to the limited precision of the fundamental constants involved in the calculation (α, R_∞, m/M). But the main uncertainty comes from the proton structure contribution, and this limits the possibility to test the QED comparing the predicted value of the hyperfine splitting in hydrogen to the experimental one. This barrier was overcome measuring the HFS in muonium, and in this case an agreement up to 0.5×10^{-7} was shown between the theory and the measurement, providing an experimental confirmation to the correctness of the QED corrections [31].

Assuming the different corrections to be accurate, one can then obtain the Zemach radius of the proton from the hyperfine splitting in hydrogen and compare it to other values based on different proton form factor fits. The recent values of the Zemach radius are shown in tab. 2.2.

The puzzling result of the Lamb shift experiment renewed the interest in the evaluation of the proton Zemach radius from a measurement of the hyperfine splitting in muonic hydrogen, since a comparison between the Zemach radius extracted from ep and μp could either reinforce or delimit the proton radius

Reference		R_p(fm)
Dupays et al.	[55] (2003)	1.037(16)
Friar & Sick	[61] (2004)	1.086(12)
Volotka et al.	[56] (2005)	1.045(16)
Distler et al.	[62] (2011)	1.045(4)

Table 2.2: Recent values of the Zemach radius of the proton R_p.

puzzle: a substantial agreement with the value of R_p obtained with ordinary hydrogen could suggest that the explanation of the puzzle may lie in unconsidered methodology uncertainties, while a big discrepancy would give good reasons to look for new physics beyond the Standard Model [63].

In addition to this, muonic hydrogen is much more sensitive to the proton structure if compared to ep as already explained in sec. 1.2.3. The expressions derived in the previous section for the calculation of the HFS are still valid in the μp case, but the relative importance of the different corrections may change. The Fermi splitting (eq. (2.6)) is now approximatively 182 meV, corresponding to a wavelength of 6.8 µm. The latest theoretical values, obtained taking into account all known corrections, are $\Delta E^{\mathrm{hfs(th)}}_{\mu 1} = 182.725(62)\,\mathrm{meV}$ [59] and $\Delta E^{\mathrm{hfs(th)}}_{\mu 2} = 22.8148(78)\,\mathrm{meV}$. The effect of the Zemach and polarizability corrections related to the proton structure is enhanced by a factor $m_\mu/m_e \approx 206$ with respect to ordinary hydrogen and becomes the most relevant correction to the Fermi splitting in muonic hydrogen. For this reason, a measurement of the HFS in μp cannot be used as a test of QED at low energy since the effects of radiative corrections are overshadowed by the $\delta^{\mathrm{structure}}$ contribution [55].

The theoretical uncertainty on $\Delta E^{\mathrm{hfs(th)}}_{\mu n}$ is of the order of 10^{-4} and is mainly due to the uncertainty on the estimation of the Zemach and polarizability corrections, which have to be added to not yet calculated higher order radiative terms and to the uncertainty of δ^{vp} [55], whose contribution is much larger than in the case of ep [64]. The accuracy of the current value of δ^{Z} and δ^{pol} may be improved by a measurement of the hyperfine splitting in the μp ground state if the experimental uncertainty is kept below 10^{-4}. In particular, the polarizability correction is not related to a single physical parameter like the Zemach term, but is expressed in terms of the polarized structure functions of the proton that introduce model-dependent parameters [55]. Therefore, the measurement of HFS in ordinary and muonic hydrogen can be regarded as a measurement of the proton Zemach radius R_p.

In literature, only few experimental values of the hyperfine splitting in muonic hydrogen are present. The Lamb shift experiment at PSI (described in sec. 1.2.3), obtained as a by-product of the measurement of the $2S^{\mathrm{F}=1}_{1/2} \rightarrow 2P^{\mathrm{F}=2}_{3/2}$ and $2S^{\mathrm{F}=0}_{1/2} \rightarrow 2P^{\mathrm{F}=1}_{3/2}$ transition energy, provides a value of the hyperfine splitting of the $n = 2$ state of 22.8089(51) meV resulting in $R_\mathrm{p} = 1.082(37)\,\mathrm{fm}$ [43]. However the relative uncertainty of about 4% in the Zemach radius measurement is too large for any useful comparison between different experimental values and theoret-

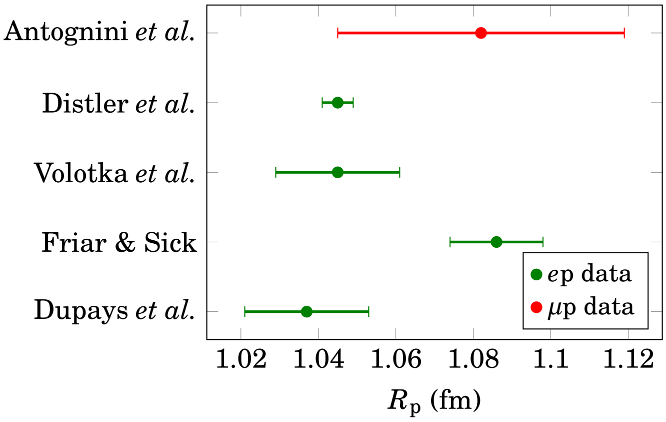

Figure 2.1: Recent values of the Zemach radius of the proton obtained using data from ordinary hydrogen (green dots) and muonic hydrogen (red dot). See tab. 2.2 and text for references.

ical predictions. The hyperfine splitting of the μp ground state was obtained directly from the spectroscopic data of the $3P \rightarrow 1S$ transition resulting in $\Delta E_{\mu 1}^{\mathrm{hfs(exp)}} = 211(19)\,\mathrm{meV}$ [65], but the uncertainty of 9% is way too large for the determination of the Zemach radius. The current available values of R_{p}, including the one obtained with the muonic hydrogen by Antognini et al., are shown in fig. 2.1.

A measurement of R_{p} with a relative uncertainty below 0.5%, in addition to providing new data that could help to solve the proton radius puzzle, would offer an efficient tool for testing the proton structure, imposing independent experimental bounds on the low transfer momentum limit of the proton electric and magnetic form factors ratio [55, 64].

These reasons, together with the outstanding progress in the development of tunable laser systems in the far infrared (FIR) region, provide a strong motivation for the accurate determination of the Zemach radius and the development of a suitable experimental strategy.

2.3 THE FAMU EXPERIMENTAL PROPOSAL

At present, a direct measurement of the μp$(1S)$ hyperfine splitting has never been performed, although several experimental methods have been proposed in the last twenty years [66]. The recent results from the measurement of the Lamb shift in muonic hydrogen give the motivation needed to intensify the experimental efforts in this direction.

The FAMU experiment develops in the framework of the research on the electromagnetic structure of the proton, proposing an accurate measurement of the hyperfine splitting of the muonic hydrogen ground state. The goal of the experiment is to extract from the measurement of $\Delta E_{\mu 1}^{\mathrm{hfs}}$ the Zemach radius of the proton with a relative precision below 1%.

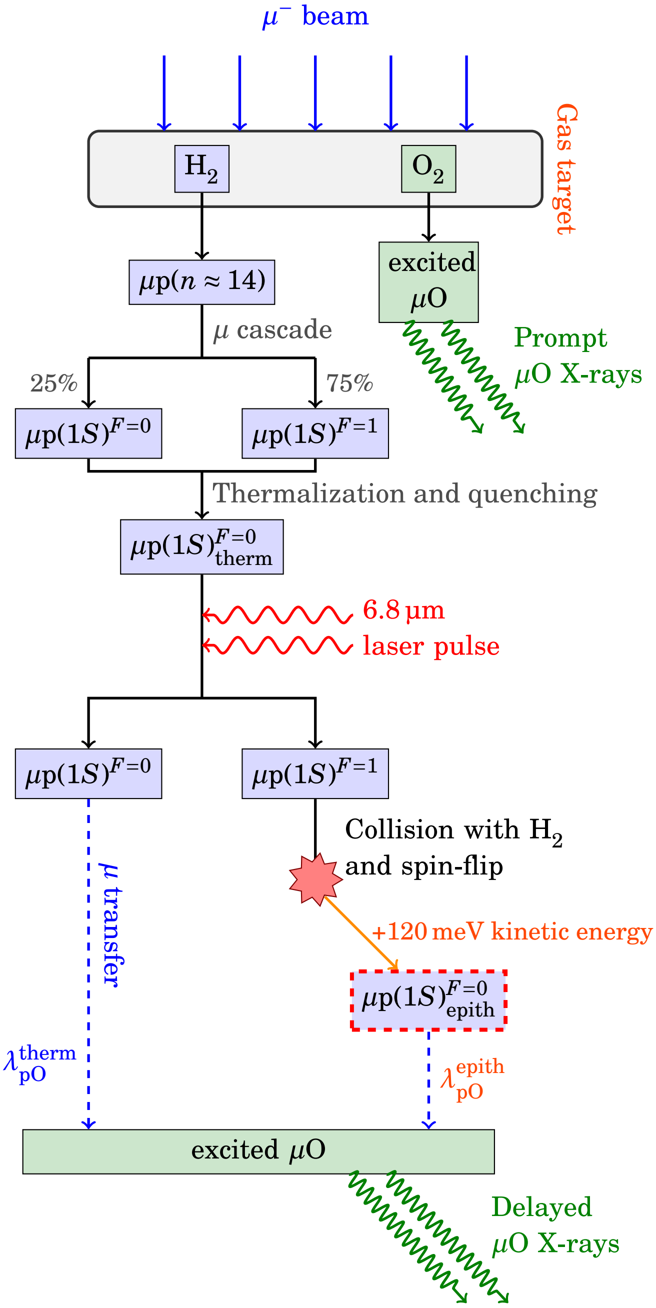
μ^- beam
Gas target
H_2
O_2
$\mu p(n \approx 14)$
excited μO
Prompt μO X-rays
μ cascade
25%
75%
$\mu p(1S)^{F=0}$
$\mu p(1S)^{F=1}$
Thermalization and quenching
$\mu p(1S)^{F=0}_{therm}$
6.8 µm laser pulse
$\mu p(1S)^{F=0}$
$\mu p(1S)^{F=1}$
Collision with H_2 and spin-flip
μ transfer
+120 meV kinetic energy
$\mu p(1S)^{F=0}_{epith}$
λ^{therm}_{pO}
λ^{epith}_{pO}
excited μO
Delayed μO X-rays

Figure 2.2: Schematic representation of the FAMU experimental method. Here a mixture of hydrogen and oxygen is used for simplicity, but also other gases can be used in place of O_2 (see text for explanation).

The experimental method for this measurement, proposed in [67], combines elementary particles with laser spectroscopy techniques and its schematic representation is shown in fig. 2.2. Muons slowed down and stopped in a hydrogen gas target form muonic hydrogen atoms: ~ 75% in the triplet state ($F = 1$) and the remaining part in the singlet configuration ($F = 0$). Collisions between muonic hydrogen atoms and H_2 molecules quickly de-excite the μp$(1S)^{F=1}$ atoms to the singlet state, leaving thermalized muonic hydrogen atoms in the $(1S)^{F=0}$ state. At this point, a laser tuned on the HFS resonance is sent inside the target, inducing a series of singlet-to-triplet transitions. Muonic hydrogen atoms in the $(1S)^{F=1}$ state are once again de-excited back to the singlet state in collision with H_2 molecules and the transition energy is converted into additional kinetic energy of the μp–H_2 system. In this way the μp atom gains about 2/3 of the hyperfine transition energy ($\approx 120\,\text{meV}$).

The challenge is then to find a method to detect these “kicked” muonic atoms exploiting the additional kinetic energy obtained by the hyperfine de-excitation. This requires a reaction whose rate depends on the μp velocity. The original idea of Bakalov et al. [66] was to observe the diffusion of μp atoms in a small volume studying the number of muon-transfer events on the target walls. These events are easy to detect because when a muon is transferred from μp to a heavier atom, it usually occupies an excited state and immediately de-excites to the ground state via the emission of a characteristic X-ray. The main drawback of this method is the impossibility to embed the target in a multipass optical cavity in order to amplify the laser radiation. As will be shown in sec. 2.3.2, this constraint limits dramatically the number of “spin–flipped” μps, making this method practically inapplicable.

This approach was later improved in [67], when Bakalov et al. proposed to study the muon-transfer events (μTEs) from muonic hydrogen to another higher-Z gas instead of the target walls. Indeed, although theory predicts in the general case a flat behaviour for the muon-transfer rate $\lambda_{\text{p}Z}$ at low energies, there are few gases in which it is proved that this is not the case. The first gas that was demonstrated to show such a particular behaviour was oxygen [68, 69], that exhibits a sort of peak in the muon transfer rate $\lambda_{\text{p}Z}^{\text{epith}}$ at the epithermal energy (~ $100\,\text{eV}$). Later theoretical and experimental studies suggested that also argon and neon could exhibit similar properties [70, 71]. Thus, adding small quantities of one of these gases to hydrogen, one can obtain the number of accelerated μps from the number of muon-transfer events measuring the characteristic X-rays of the added gas.

Performing a scan over the laser frequency near the HFS transition one and counting for each frequency the number of the μTEs, one can then obtain a resonance plot similar to the one in fig. 1.12 and thus the value of the hyperfine splitting of the $1S$ state.

In the following sections, the key elements of this method will be described.

2.3.1 *Muonic atoms formation and thermalization*

A negative muon interacting in matter is initially scattered from atom to atom, gradually losing its energy until it decays or is captured into an external atomic orbit of an atom. The energy released in the atomic capture process is transferred to Auger electrons that are emitted from the atom. The characteristic cross section for the atomic muon capture[1] depends not only on Z, but also on some features of the atomic structure such as the number of loosely bound electrons [72]. For hydrogen, the case is much simpler. Typically, muonic hydrogen is formed at the $n \sim 14$ energy levels since the optimum overlap of the bound muon and electron wave functions occurs (approximatively) at $n \approx \sqrt{m_\mathrm{r}(\mu\mathrm{p})/m_\mathrm{r}(e\mathrm{p})} \approx 14$ [41]. The formation of these highly excited atoms is followed by a number of transitions, also called *muon cascade*, down to the $1S$ ground state ($\sim 99\%$) or to the $2S$ metastable state [41]. However, for a pressure of the gas target large enough (above 10 atm) the whole cascade process takes no more than about 1 ns [63]. The choice of a large target pressure was motivated by the fact that simulations show that too few muons are stopped in a gas target with smaller density [63].

A computational study of the thermalization and depolarization of the muonic hydrogen atoms was then carried out in [63] starting from a collection of $\mu\mathrm{p}(1S)$ atoms with the singlet and triplet state populated statistically. Part of the energy released in the de-excitation cascade of the muonic hydrogen is converted into kinetic energy, spreading the thermal distribution over a broad interval up to the keV range. Thermalization and depolarization take place via elastic and spin-flip scattering with the H_2 molecules and the heavier gas. The collision with the lighter hydrogen molecules is the main component of the thermalization process; the rate of thermalization depends just slightly on the contaminating gas, depending only on the hydrogen density and on the temperature T through the molecular cross section [73, 74]. The same holds for the rate of depolarization [63].

The thermalization process can be effectively illustrated with the time evolution of the average kinetic energy of the $\mu\mathrm{p}(1S)$ atoms at different pressures and temperatures obtained from Monte Carlo simulations.

One can easily notice in fig. 2.3a that the time needed to muonic hydrogen atoms to thermalize has approximatively an inverse proportionality to the target pressure P (or to the atomic density ϕ, where ϕ is expressed in units of the liquid hydrogen density $\rho_\mathrm{lh} = 4.25 \times 10^{22}\,\mathrm{cm}^{-3}$). Fig. 2.3b shows that for a fixed density $\phi = 0.045$ the time needed for the thermalization of $\mu\mathrm{p}$ atoms is practically the same ($\approx 150\,\mathrm{ns}$) for all the considered temperatures. Thus, the gas density ϕ is the crucial parameter that determines the thermalization time.

The quenching of the $F = 1$ states of muonic hydrogen takes places via the collision with H_2 molecules too. However the depolarization of $\mu\mathrm{p}$ atoms, *i.e.* the depopulation of the triplet spin state, is much faster than the thermalization

---

[1] The atomic muon capture is not to be confused with the muon capture process, which is described by the weak process $\mu + \mathrm{p} \to \nu_\mu + \mathrm{n}$.

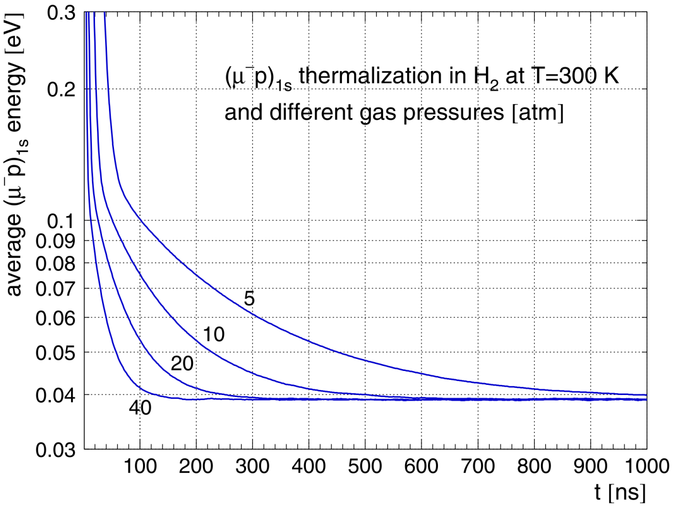

(a)

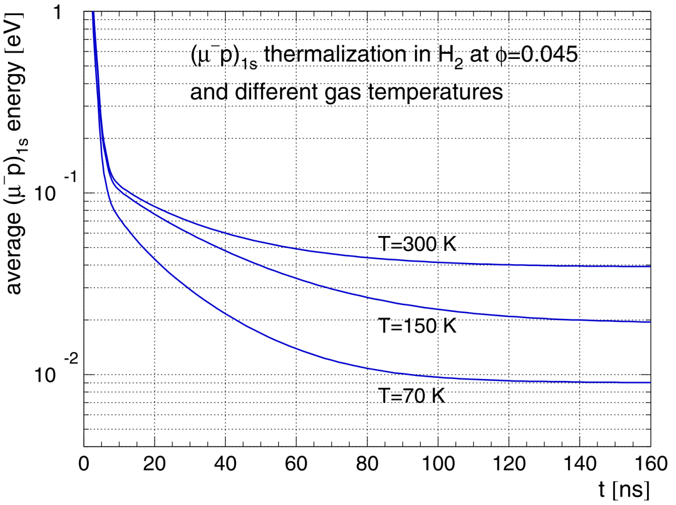

(b)

Figure 2.3: Time evolution of the average $\mu p(1S)$ **(a)** for different target pressures at a constant temperature and **(b)** at different temperatures for a fixed hydrogen density [63].

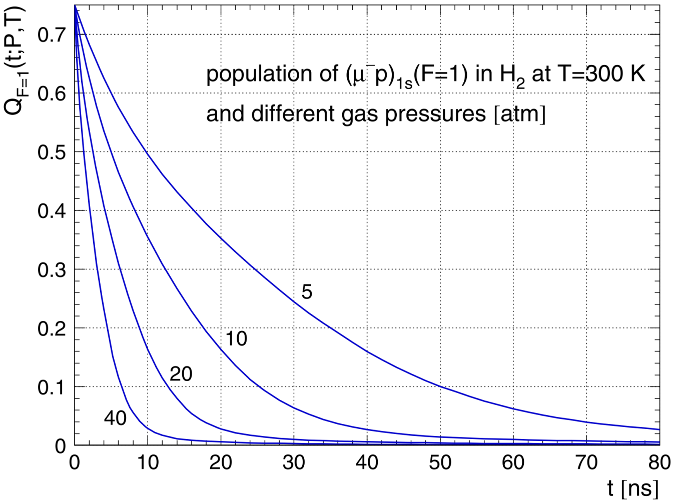

Figure 2.4: Time evolution of the population of the triplet state of muonic hydrogen at a room temperature $T = 300\,\mathrm{K}$ for the pressures $P = 5$, 10, 20 and 40 atm [63].

process [63]. As shown in fig. 2.4, the population of the $\mu\mathrm{p}(1S)^{F=1}$ state (normalized to 3/4 at $t = 0$) decreases at the same pressure and temperature conditions of fig. 2.3a about a order of magnitude faster than the thermalization process [63].

From the results of these simulations it is possible to assume with good accuracy that muonic atoms are completely thermalized and depolarized after a time t_0 given by [63]

$$t_0[\mathrm{ns}] \approx 20 \cdot \frac{T[\mathrm{K}]}{P[\mathrm{atm}]} \tag{2.20}$$

2.3.2 *Laser requirements*

Once the muonic atoms have been thermalized and depolarized, a laser with a frequency tuned in the HFS region is sent into the target. The required power of a tunable laser with a wavelength near 6.8 µm to spin-flip a reasonable number of muonic atoms was evaluated in [64].

The matrix element for the singlet-to-triplet transition of $\mu\mathrm{p}(1S)$ when stimulated by an oscillating magnetic field $\boldsymbol{B}(t) = \boldsymbol{B}_0 \cos(2\pi\nu t)$ is

$$\left\langle \mu\mathrm{p}(1S)^{F'=1} \middle| -e\cos(2\pi\nu t)\left(\frac{\mu_\mathrm{p}}{m_\mathrm{p}}\boldsymbol{B}_0\cdot\boldsymbol{s}_\mathrm{p} - \frac{\mu_\mu}{m_\mu}\boldsymbol{B}_0\cdot\boldsymbol{s}_\mu\right) \middle| \mu\mathrm{p}(1S)^{F=0} \right\rangle =$$

$$= -\frac{e\hbar}{2}\cos(2\pi\nu t)\left[\frac{\mu_\mathrm{p}}{m_\mathrm{p}} + \frac{\mu_\mu}{m_\mu}\right] \tag{2.21}$$

where m_p, m_μ, $\boldsymbol{s}_\mathrm{p}$, $\boldsymbol{s}_\mu$ denote the mass and the spin operator of the proton and the muon, and the quantization axis is chosen parallel to $\boldsymbol{B}_0$ [64]. The muon and the proton magnetic moment μ_p and μ_μ are in unit of $e\hbar/(2m_\text{p})$ and $e\hbar/(2m_\mu)$ respectively.

The probability per unit of time for the spin-flip transition is then

$$\frac{\mathrm{d}P}{\mathrm{d}t}(\nu,\nu_0) = \frac{1}{\hbar^2}\left(\mu_\text{B}|\boldsymbol{B}_0|\right)^2\left[\frac{\mu_\text{p}}{m_\text{p}} + \frac{\mu_\mu}{m_\mu}\right]^2 \delta(\nu-\nu_0) \tag{2.22}$$

being μ_B the Bohr magneton and ν_0 the resonance frequency. The probability distribution ρ_D of ν_0 around the resonance at rest $\overline{\nu}_0 = \Delta E^\text{hfs}_{\mu 1}/h$ is not a δ function because of the Doppler effect, resulting in

$$\rho_\text{D}(\nu_0) = \frac{1}{\sigma_\text{D}\sqrt{2\pi}}\exp\left\{-\frac{(\nu_0-\overline{\nu}_0)^2}{2\sigma_\text{D}^2}\right\} \quad \text{with} \quad \sigma_\text{D} = \overline{\nu}_0\cdot\sqrt{\frac{kT}{(m_\text{p}+m_\mu)c^2}} \tag{2.23}$$

Taking into account also the laser line width $\rho_\text{L}(\nu)$, the observable transition probability per unit of time becomes [64]

$$\begin{aligned}\frac{\mathrm{d}\overline{P}}{\mathrm{d}t} &= \int \mathrm{d}\nu_0 \rho_\text{D}(\nu_0)\int \mathrm{d}\nu \rho_\text{L}(\nu)\frac{\mathrm{d}P}{\mathrm{d}t}(\nu,\nu_0) \\ &\simeq \sqrt{\frac{(m_\text{p}+m_\mu)c^2}{2\pi kT\overline{\nu}_0^2}}\left[\frac{\mu_\text{B}}{\hbar}\left(\frac{m_e}{m_\text{p}}\mu_\text{p} + \frac{m_e}{m_\mu}\mu_\mu\right)\right]^2 |\boldsymbol{B}_0|^2\end{aligned} \tag{2.24}$$

given that $\sigma_\text{D} \gg \sigma_\text{L}$ in the case of interest.

The squared modulus of $\boldsymbol{B}_0$ is related to the average density of energy flux $\overline{\boldsymbol{F}}$ carried by the electromagnetic field by the relation $|\overline{\boldsymbol{F}}| = c/(2\mu_0)\cdot|\boldsymbol{B}_0|^2$, where μ_0 is the vacuum magnetic permeability. Integrating eq. (2.24) over the duration of the laser pulse τ and substituting $|\boldsymbol{B}_0|^2$ with the energy density flux, one obtains

$$\overline{P} \simeq \frac{\mu_0\mu_\text{B}^2}{\hbar^2 c^2\overline{\nu}_0}\sqrt{\frac{(m_\text{p}+m_\mu)c^2}{2\pi kT}}\left(\frac{m_e}{m_\text{p}}\mu_\text{p} + \frac{m_e}{m_\mu}\mu_\mu\right)^2 |\overline{\boldsymbol{F}}|\tau \tag{2.25}$$

Expressing the energy density flux $|\overline{\boldsymbol{F}}|$ in terms of the energy output E, the duration of the pulse τ and the laser beam cross section A ($|\overline{\boldsymbol{F}}| = E/(A\tau)$), the transition probability can be roughly expressed as [64]

$$\overline{P} \approx 8\times 10^{-5}\cdot\frac{E[\text{J}]}{A[\text{m}^2]\sqrt{T[\text{K}]}} \tag{2.26}$$

Evaluating eq. (2.26) using the energy output of the IR laser developed for the Lamb shift experiment (0.25 mJ) [16, 25] focused on a 1 cm^2 area, the spin-flip probability results to be 1.2×10^{-5} at 300 K, definitely too small for the proposed experiment [64]. The transition probability may be increased by lowering the temperature of the target, but T should be kept higher than $\sim$ 10 K to avoid the formation of unwanted molecular pμp ions.

The efficiency of this process may be substantially increased by squeezing the laser beam reducing its cross section and placing the target atoms within a multipass cavity that provides k reflections. Using a multipass cavity similar to the one used in the Lamb shift experiment ($k \sim 2\times 10^3$) [16] it is possible to reach a transition probability of about 12%, much more adequate for the goal of this experiment.

2.3.3 *Muon transfer to a higher-Z gas*

Once a number of muonic hydrogen atoms large enough has been excited to the triplet state, these atoms are de-excited back to the $F = 0$ state through collisions with the H_2 molecules gaining about 120 meV of kinetic energy in the process. The key point of this experimental proposal is the possibility to detect these kicked atoms by studying the muon transfer rate from μp to specific higher-Z gases that exhibit a sensitive energy dependence in the muon-transfer cross section.

The first evidence that some elements could show this particular behaviour was obtained by Mulhauser and collaborators [69] studying the muon-transfer rate from μp atoms to SO_2 molecules in the framework of the research on the muon-catalyzed fusion [75].

When a muon is stopped in hydrogen, it forms a muonic hydrogen atom that is quickly de-excited and thermalized as described in the previous section. If in the hydrogen target there are small contaminations of another gas G, the muonic hydrogen can disappear by muon decay, with an associated rate $\lambda_0 = \tau_\mu^{-1}$, or by muon transfer to the G gas with a rate λ_{pG}. In order to compare these rates, they are usually normalized to the liquid hydrogen density ρ_{lh}. Hence, the lifetime $\tau = \lambda^{-1}$ of the muonic hydrogen atom under the particular condition of pressure, temperature and contamination of the experiment is [68]

$$\tau^{-1} = \lambda = \lambda_0 + \phi c_{\mathrm{G}} \lambda_{\mathrm{pG}} \tag{2.27}$$

where ϕ is the atomic density of the gas mixture under investigation normalized to the density of liquid hydrogen and c_{G} is the atomic concentration of the G element. The characteristic X-rays of the G gas are emitted immediately after both a direct atomic capture of a muon and the transfer of a muon from a μp atom. However, with a properly delayed time window, one is able to consider only the X-rays due to the muon transfer. Their time distribution $N_{\gamma\mathrm{G}}(t)$ is expected to follow the evolution of the number of muonic hydrogen atoms $N_{\mu\mathrm{p}}(t)$, being proportional to

$$N_{\gamma\mathrm{G}}(t) \propto \lambda_{\mathrm{pG}} N_{\mu\mathrm{p}}(t) \propto \lambda_{\mathrm{pG}} N_{\mu\mathrm{p}}^0 \mathrm{e}^{-\lambda t} \tag{2.28}$$

where $N_{\mu\mathrm{p}}^0$ is the initial number of muonic hydrogen atoms.

Observing the time distribution of the characteristic $2P \to 1S$ X-rays for sulphur and oxygen in a hydrogen target with a 0.4% addition of SO_2 (fig. 2.5), Mulhauser and collaborators found that the two gases exhibit quite different behaviours [69].

The time spectrum of the delayed muonic sulphur $2P \to 1S$ transition (fig. 2.5 left), as well as for the Lyman and Balmer transitions, shows an exponential decay with a characteristic time τ_1 as expected. In contrast, the time distributions of the four Lyman transitions of muonic oxygen μO present a more complex structure with two different "decay" times (fig. 2.5 right) [69], the longer (τ_1) being the same of the sulphur one and the other (τ_2) much shorter.

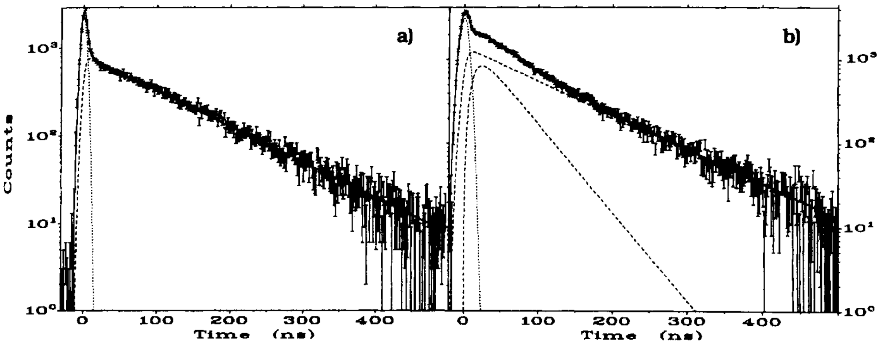

Figure 2.5: Measured time distribution of $2P \rightarrow 1S$ X-rays of sulphur (left) and oxygen (right). Considering the sulphur X-rays distribution the prompt peak and the exponential decay are easy to distinguished, while for oxygen the structure of the time spectrum is more complex [69].

The sulphur characteristic time τ_1, which is the same of the far delayed events of the μO X-rays time spectrum in fig. 2.5, is interpreted as the mean lifetime of the thermalized μ atoms [68] ($\tau_1 = \lambda^{-1}$ with λ defined in eq. (2.27)).

Repeating the measurement for different pressures and concentrations of SO_2, the same shape of the time distribution of the oxygen characteristic X-rays was observed. Additional studies using hydrogen with a O_2 addition were later performed [68, 76] obtaining the same peculiar structure in the time spectrum of the μO X-rays.

The τ_2 parameter was found to depend on the target pressure and on the oxygen concentration [69]. This led to the interpretation that τ_2 reflects the mean lifetime of a particular μp(1S) state which decays mainly through a channel depending on the hydrogen density c_p and another one depending on the oxygen concentration c_O: the latter channel is clearly related to the muon-transfer to oxygen, while the first one points to a thermalization process [76]. Hence, the τ_2 parameter was expressed as

$$\tau_2^{-1} = \lambda_2 = \lambda_0 + \phi\left(c_\mathrm{p}\lambda_\rho + c_\mathrm{O}\lambda^*_\mathrm{pO}\right) \tag{2.29}$$

where the thermalization (λ_ρ) and the transfer to oxygen (λ^*_pO) rates have been introduced. Using the data collected at different pressures and oxygen concentrations, a thermalization rate of $\lambda_\rho = 8.2(7) \times 10^8\,\mathrm{s}^{-1}$ was obtained. The muon transfer rate extracted from τ_2 was $\lambda^*_\mathrm{pO} = 2.1(3) \times 10^{11}\,\mathrm{s}^{-1}$, to be compared to $\lambda_\mathrm{pO} = 0.83(8) \times 10^{11}\,\mathrm{s}^{-1}$ obtained from τ_1 using eq. (2.27).

The short-time slope τ_2 of the oxygen X-rays time distribution is then interpreted as the mean lifetime of *ephitermal* μp atoms. This can be explained using a simplified two-components model depicted in fig. 2.6 and assuming an energy dependence of the muon transfer rate to oxygen. As described in sec. 2.3.1, muonic hydrogen atoms are formed in high-excited states and part of the deexcitation energy is converted in kinetic energy. In addition, the quenching of the triplet states also releases about 120 meV kinetic energy to the μp atoms. As

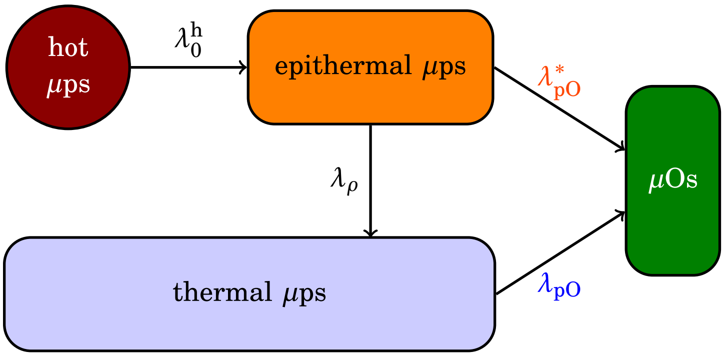

Figure 2.6: Schematic representation of the two-component model for the muon transfer to oxygen [76].

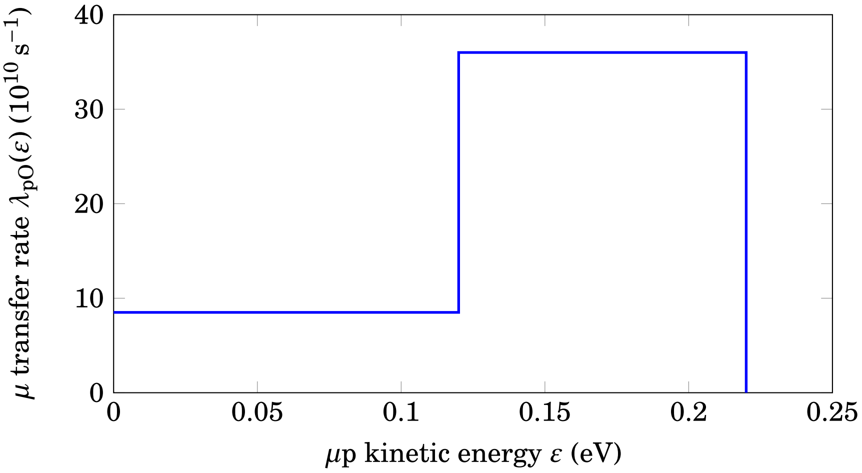

Figure 2.7: Transfer rate λ_{pO} as a function of the μp atom kinetic energy used in [68]. The energy dependence is approximated using a simple step-function with $\lambda_{pO} = 8.3 \times 10^{10}\,s^{-1}$ for ε smaller than 120 meV, $\lambda_{pO} = 36 \times 10^{10}\,s^{-1}$ for ε between 120 meV and 220 meV and $\lambda_{pO} = 0$ for higher energies.

a result, the kinetic energy distribution of the muonic hydrogen is not simply a Maxwellian distribution centered on the nominal target temperature (~ 40 meV at room temperature), but a strong component with a mean energy of ~ 20 eV is also present. These hot atoms are slowed down with a deceleration rate λ_0^h to epithermal energies. Once μp has reached the epithermal energy range, it can either transfer its muon to oxygen with a rate $\lambda_{pO}^* = \lambda_{pO}^{epith}$ or be thermalized with a rate λ_ρ. Thermalized μp atoms join the thermal component of the initial energy distribution, whose muon transfer rate to oxygen is λ_{pO} [76].

Monte Carlo simulations performed using the ultra-simplified step function shown in fig. 2.7 as a model for the energy dependence of the muon transfer rate to oxygen $\lambda_{pO}(\varepsilon)$ confirmed this interpretation.

A theoretical treatment of the muon transfer process is not easy. A muonic hydrogen atom in the 1S state is a small electrically-neutral object that can eas-

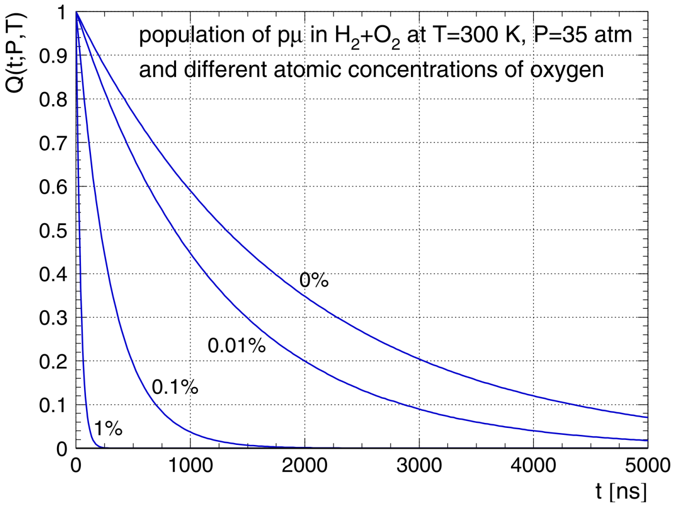

Figure 2.8: Number $Q(t;P,T)$ of survived μp(1S) atoms in a H_2–O_2 gas mixture at 300 K, 35 atm for various oxygen concentrations. $Q(t;P,T)$ is normalized to the number of depolarized and thermalized μps at the time t_0 (eq. (2.20), here $t_0 = 0$ for simplicity) [63].

ily penetrate the electron hull of other atoms. The muon transfer process then is reduced to a three-bodies problem involving the proton, the muon and the Ze nucleus. The evidence of an energy dependence in the muon transfer rate to some specific elements (in particular, oxygen) motivated detailed theoretical studies. However, results obtained by Dupays et al. in [77–79] and Le and Lin [80] are not perfectly compatible and still quite controversial, also for the lack of experimental data. An accurate analysis of this process is thus needed and this is one of the goals of the test that will be performed in the future.

However, whatever the exact dependence of $\lambda_{\mathrm{pG}}(\varepsilon)$ on energy is, in the experiment is fundamental to have a large number of μp(1S) atoms at a time larger than the width of the peak of the *prompt* characteristic X-rays that follow the direct atomic muon capture of the G gas. Results of the simulations in [63] for oxygen (fig. 2.8) show that, for the same conditions of pressure and temperature, the higher the concentration of O_2, the faster the depopulation of μp is. The optimal oxygen concentration is reached when, given a fixed number of muons stopped in hydrogen, the maximum number of muon-transfer events from thermalized muons takes place. The results of the Monte Carlo simulation for different oxygen concentrations, shown in fig. 2.9, suggest that the statistical uncertainty of a measurement of the muon transfer rate (being proportional to the inverse squared root of the number of μTEs) can be drastically reduced by choosing the right gas concentration.

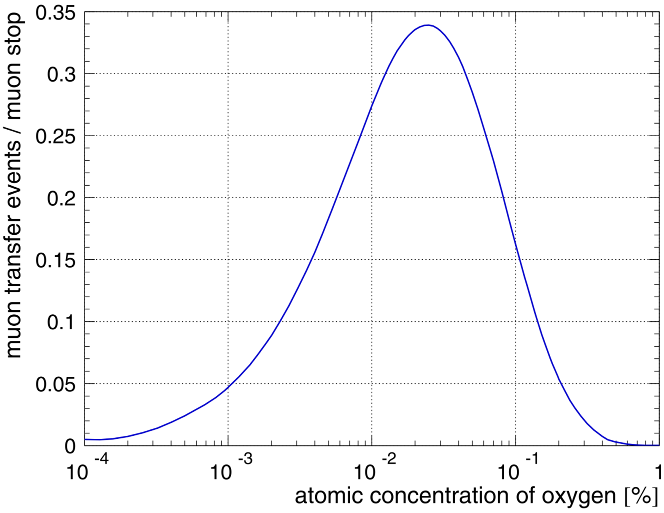

Figure 2.9: Number of muon-transfer events from thermalized μp($1S$) atoms to oxygen for $T = 300\,\mathrm{K}$ and $P = 35\,\mathrm{atm}$ scaled for the number of muonic hydrogen atoms thermalized and depolarized as a function of the oxygen concentration [63].

CHAPTER 3

THE 2014 BEAM TEST: EXPERIMENTAL SET-UP

In June 2014 the FAMU collaboration tested the feasibility of the measurement described in the previous chapter using a preliminary version of the set-up imagined for the final experiment.

To perform the measurement, a pulsed muon beam is needed. Such a requirement can be satisfied only by two facilities in the world: the ISIS muon source located at the Rutherford Appleton Laboratory (RAL, UK) and the MUSE muon science facility, which is part of J-PARC (Japan Proton Accelerator Research Complex).

The beam test has been performed at the RIKEN-RAL muon facility, that will be described in the first part of this chapter. The proposed experiment requires the construction of a gas target surrounded by a detection system to measure the X-rays coming from the muonic atoms transition inside the target. The detection system for the X-ray spectrometry has two main components: a fast one with five $LaBr_3$(Ce) scintillating detectors placed near the vessel and a slow but very accurate HPGe detector positioned far from the target.

In order to obtain information both on the X-ray energy and the time of the detection, both the HPGe and the $LaBr_3$ scintillating detectors were readout using a 500 MHz digitizer. A detailed description of the Data Acquisition (DAQ) system is given in sec. 3.3. The last part of the chapter is devoted to the software for the off-line data analysis (sec. 3.4) and the results of this analysis strategy applied to calibration runs.

3.1 THE RIKEN-RAL FACILITY

The RIKEN-RAL [81] muon facility is one of the structures connected to the ISIS proton synchrotron located at the Rutherford Appleton Laboratory in the Harwell Oxford Science and Innovation Campus, Oxfordshire (UK). This laboratory is operated by the Science and Technology Facilities Council[1] (STFC), one of the seven publicly founded Research Councils in the United Kingdom. Among many scientific facilities, RAL hosts ISIS, a synchrotron able to accelerate protons up to an energy of 800 MeV that are used to produce intense pulsed muon and neutron beams. Two different targets for neutron production and a target for muon production are present. A schematic view of the ISIS ac-

---

[1] Web site: `http://www.stfc.ac.uk/`

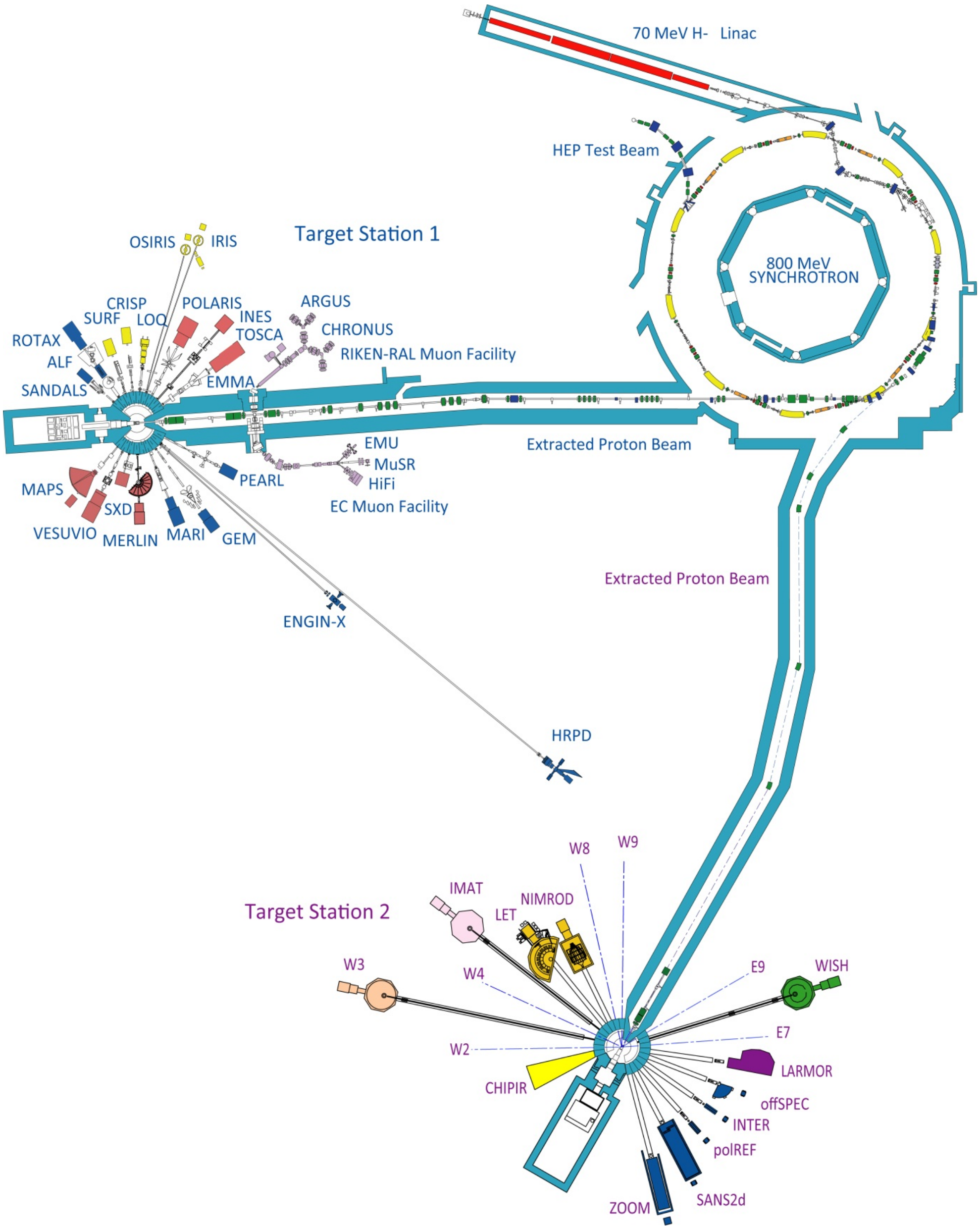
70 MeV H- Linac
HEP Test Beam
800 MeV SYNCHROTRON
Target Station 1
OSIRIS
IRIS
CRISP
SURF
LOQ
POLARIS
INES
TOSCA
ARGUS
CHRONUS
RIKEN-RAL Muon Facility
ROTAX
ALF
SANDALS
EMMA
Extracted Proton Beam
EMU
MuSR
HiFi
PEARL
EC Muon Facility
MAPS
SXD
VESUVIO
MERLIN
MARI
GEM
ENGIN-X
Extracted Proton Beam
HRPD
W8
W9
IMAT
NIMROD
LET
Target Station 2
W3
W4
E9
WISH
E7
W2
CHIPIR
LARMOR
offSPEC
INTER
polREF
ZOOM
SANS2d

Figure 3.1: Sketch of the ISIS accelerator complex (Image credit: STFC, `https://www.stfc.ac.uk/2912.aspx`).

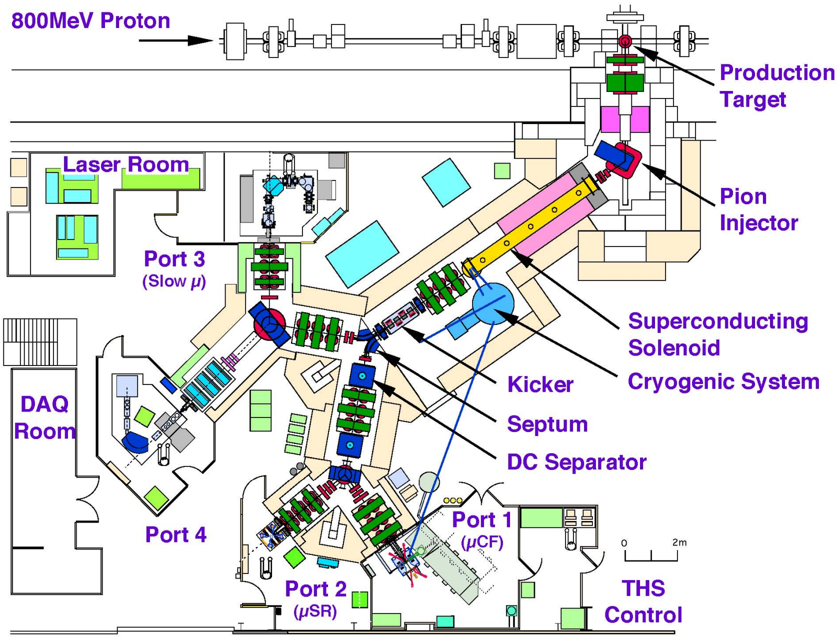
800MeV Proton
Production Target
Pion Injector
Laser Room
Port 3
(Slow μ)
Superconducting Solenoid
Cryogenic System
Kicker
Septum
DC Separator
DAQ Room
Port 4
Port 1
(μCF)
0
2m
Port 2
(μSR)
THS Control

Figure 3.2: Layout of the RIKEN-RAL muon facility (Image credit: STFC).

celerator complex, including the different target stations, is shown in fig. 3.1. The muon target is placed 20 m upstream the Target Station 1 for neutron production and consists of a 10 mm thick carbon target. Pions produced by the 200 µA, 800 MeV proton beam impinging on carbon as well as *surface muons* coming from the pion decay on the surface of the production target, are collected and momentum-analysed in the pion injection system (fig. 3.2) and transported into the RIKEN-RAL muon facility[2] through a superconducting solenoid magnet, where pions decay to muons during the flight. A muon beam is delivered to four experimental ports (Port 1–4 in fig. 3.2) dedicated to different scientific activities such as material science exploiting various μSR techniques (muon Spin Relaxation, Rotation and Resonance) and the study of muon catalized d-t fusion (μCF).

3.1.1 *Muon beam properties*

The muon beam delivered to the experimental ports reflects the behaviour of the ISIS proton beam showing a 50 Hz double-pulse structure. Each pulse is about 70 ns long and the time between the two pulses is 320 ns (fig. 3.3).

To exploit most effectively this particular feature, the double-pulsed muon beam can be separated into two single pulsed muon beams delivered to two different experimental ports by the kicker magnet system. In order to accom-

---

[2] The RIKEN-RAL muon facility was built by the RIKEN Nishima Center for Accelerator-Based Science as part of an agreement between RIKEN and the UK Science and Engineering Research Councils signed in 1990 and extended in 2000 until March 2018.

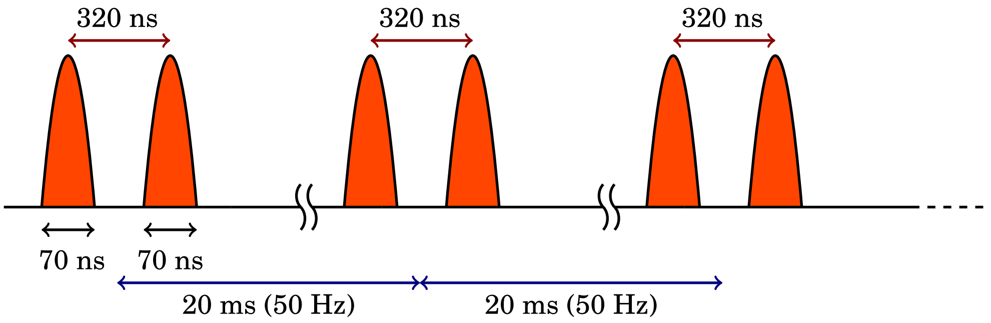

Figure 3.3: Time structure of the pulsed muon beam. The pulse width of 70 ns is intended at FWHM.

plish its task, the kicker magnet should generate a pulsed flat magnetic field of a duration longer than 150 ns with rise/fall times shorter than 230 ns [81] so that only the first *or* the second pulse is deflected. Unfortunately, at the time of the June 2014 beam test, the use of a single-pulsed muon beam was possible only for a muon beam with a momentum $\lesssim 30\,\mathrm{MeV}/c$, while - as will be explained later - the measurement would require a muon beam with a higher momentum.

Surface muons and the ones generated by pions decay (also called *decay muons*) present a very different momentum range: surface muons can have a momentum in the range 20–30 MeV/c, while the decay muons one can vary between 20 and 120 MeV/c. The typical muon intensity is of the order of 1.5×10^{6} /s for surface muons while it is 4×10^{5} /s and 7×10^{4} /s for positive and negative decay muons respectively. The expected intensity as a function of the beam energy is shown in fig. 3.4 [81].

During the beam test the last collimator stage was removed, obtaining a beam with a dimension of about $4\times4\,\mathrm{cm}^2$.

3.2 DESCRIPTION OF THE EXPERIMENTAL SET-UP

The final design of the experiment presented in the previous chapter requires an intense work of development and tuning of its many parts, from the target to the detection system. The 2014 beam test at RAL was the first step in this direction.

Since there was no clear idea of the expected background, the test was quite a leap in the unknown. The main goal of the 2014 beam test was indeed to perform an exploratory measurement to evaluate the feasibility of the final experiment.

The used gas target, described in sec. 3.2.1, was indeed quite far from the imagined design for the experiment, without the cryogenic system and the optical cavity. The muon beam was monitored by a scintillating fiber hodoscope (sec. 3.2.2) readout by Silicon PhotoMultipliers (SiPM). The X-ray detection sys-

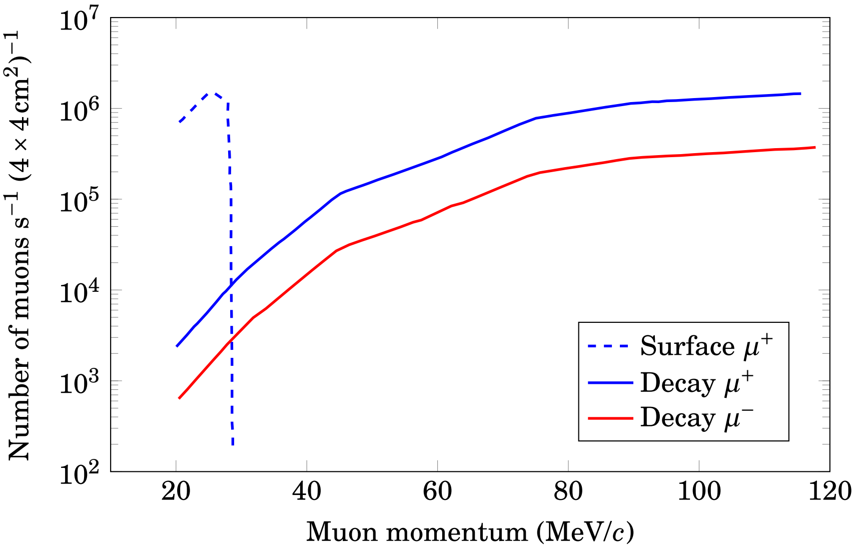

Figure 3.4: Calculated muon intensity as a function of the muon momentum on an area of $4 \times 4\,cm^2$ (from [81]).

tem consisted in five $LaBr_3(Ce)$ scintillating detectors (depicted in sec. 3.2.3) and a HPGe detector optimized for low energy X-rays that is described in sec. 3.2.4.

3.2.1 *The gas target*

The gas target is a fundamental element in the performed measurement. The gas target used in the 2014 beam test consisted of an aluminium cylindrical vessel filled with high pressure gas. The vessel, produced by Criotec Impianti S.r.l.[3], was built in the form of a $\varnothing 125\,mm \times 260\,mm$ cylinder with an inner volume of $2.8\,dm^3$ using the aluminium compound Al6061. The vessel walls are 7 mm thick except for a 4.4 cm diameter 4 mm thick entrance window. This choice was made to reduce the deterioration of the muon beam due to multiple scattering and the number of stopped muons in the target wall maintaining sufficient mechanical resistance to be certified for a pressure of tens of bars.

The cell itself is provided with a safety valve, a pressure gauge and a connection flange; this whole system was protected by a metal shield in order to prevent it from damages during the transportation and handling.

The filling gas consisted in high-purity gases provided by CK Products L.t.d.; in particular pure hydrogen (99.999%) and a special mixture of 4% (±0.08%) carbon dioxide (CO_2) in hydrogen and of 2% (±0.04%) argon (Ar) in hydrogen. All the gas mixtures are to be intended by weight.

The filling procedure foresaw evacuating the gas target to a pressure of 10^{-5} bar, cleaning it using nitrogen and then filling with the desired high purity gas. To avoid waste of time with this procedure, two identical targets were used.

---

[3] Web site: `http://www.criotec.it/`

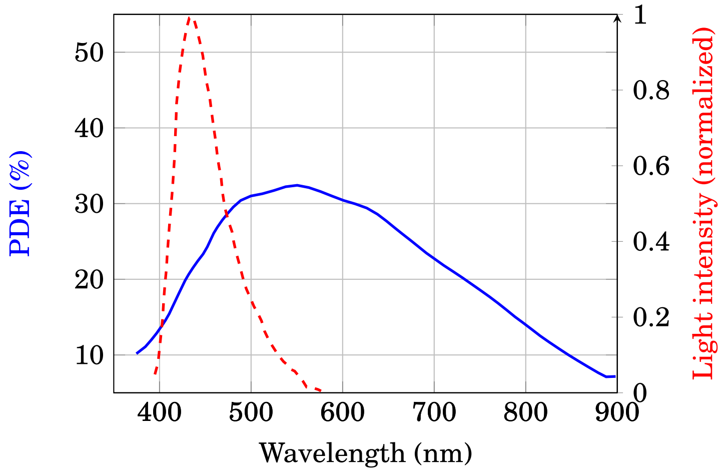

Figure 3.5: PhotoDetection Efficiency of the ASD-RGB3S-P SiPM (blue, solid) superimposed to the light output spectrum of the BCF-12 scintillating fiber (red, dashed) [82, 83].

3.2.2 *The hodoscope*

A scintillating fiber hodoscope was built in order to obtain information about the beam size, position and timing. The detector was built by the INFN sections of Milano-Bicocca and Pavia, using 64 squared shape Bicron BCF-12 scintillating fibers [82] (32 for each side, in a x-y $10 \times 10\,\text{cm}^2$ configuration) with a 3 mm pitch, readout at one end by ASD-RGB3S-P Silicon PhotoMultipliers (SiPMs) manufactured by AdvanSiD [83].

A Silicon PhotoMultiplier [84] consists of a matrix of silicon photodiodes (pixels) operating in the limited Geiger–Muller avalanche mode; each pixel has a dimension in the range $20 \times 20 - 50 \times 50\,\mu\text{m}^2$. Even if each pixel acts as a binary device, the SiPM is able to provide an analog information given its output signal is the sum of the signals of all the pixels and thus proportional to the light intensity. This particular model has an area of $3 \times 3\,\text{mm}^2$, a cell-size of $40 \times 40\,\mu\text{m}^2$ and a typical gain in the range 1–2.5×10^6. The probability for an impinging photon to trigger a Geiger discharge in the SiPM (PhotoDetection Efficiency, PDE) is about 20% at the emission peak of the scintillating fiber which is about 435 nm (fig. 3.5). The typical dark count rate is of the order of 1–5×10^7 counts/s.

The SiPMs were both readout and powered by means of a custom made system developed in the TPS project [85, 86] framework by the INFN section of Roma 3. Each module (8 channels) provides a fine regulation of the individual SiPM bias (the breakdown voltage is $\sim 29\,\text{V}$), the signal amplification, shaping and discrimination. The output signal of each SiPM was then delivered to a CAEN V792 QDC, after being attenuated of a factor 10 with a custom made attenuator, for the measurement of the charge integrated signal.

Before being used with the very intense muon beam at the RIKEN-RAL muon facility, the hodoscope was tested with a low multiplicity electron beam at the

Beam Test Facility (BTF [87]) of the INFN National Laboratories in Frascati [88]. Unfortunately, the higher intensity (~ 70 muons/spill for each fiber) of the muon beam of the RIKEN-RAL facility caused the SiPMs saturation. A new hodoscope with an electronic with larger dynamic range is currently being developed.

3.2.3 *LaBr3(Ce) scintillating detectors*

The nature of the observation of the characteristic X-ray spectrum of muonic atoms to measure the muon transfer rate puts stringent requirements on the detection system. On one hand, the detector must have a good energy resolution in order to separate different lines also in the relatively low 60–500 keV energy range. On the other hand, the detection system has to be fast enough to reduce pile-up events down to a reasonable rate and to make the precise measurement of the photon interaction time possible. Of course the pile-up rate can be reduced placing the detector at a larger distance from the target, but this would imply the need of a larger detection area and the consequent increase of the number of readout channels and the cost.

The requirements on the cost and timing performance identify HPGe (High Purity Germanium) detectors as not ideal, although they present the best performance in terms of energy resolution. This brought the attention of the collaboration on what is considered the most dramatic new alternative to NaI(Tl) in scintillator-based γ ray spectroscopy: *Lanthanum Halides*. Lanthanum chloride ($LaCl_3$(Ce)) and lanthanum bromide ($LaBr_3$(Ce)) [89, 90] have been discovered in recent years, and feature outstanding scintillator characteristics, including a high effective Z and density, a fast decay time of 30 ns (obtained with a 0.5% Ce^{3+} concentration, even faster increasing the concentration of the activator), an emission wavelength well matched to common photocathodes and an excellent energy resolution. $LaBr_3$(Ce), in particular, has raised great interest for a wide range of applications primarily because of its superior energy resolution. As a result of these features, compared with the ones of the other inorganic scintillators in tab. 3.1, $LaBr_3$(Ce) was chosen as the heart of the detection system although it is quite expensive.

One of the main drawbacks of $LaBr_3$(Ce), apart from the large cost, is the presence of a radioactive background mainly due to the presence of ^{138}La, a naturally occurring radioisotope of La with a 0.09% abundance and a half life of 1.05×10^{11} y. In 66.4% of its decays, ^{138}La undergoes electronic capture (EC) to produce excited ^{138}Ba, whose de-excitation causes the emission of a 1436 keV γ ray. As a result of the EC, the subsequent refill of the electronic shell causes the emission of a X-ray in the 35 keV region. The remaining 33.6% of the ^{138}La decays proceed via β emission (endpoint of 255 keV) to an excited state of ^{138}Ce which in turn decays emitting a 789 keV γ ray [94]. A α particle background is also present at higher energy (1750–2750 keV) due to ^{227}Ac contamination, but the increasing knowledge on the crystal growth allows manufacturers to keep the presence of this unwanted guest under control.

	Density (g/cm^3)	Z_{eff}	Light yield (ph/keV)	Decay time (ns)	Refr. index	$\Delta E/E$	λ_{max} (nm)	Relative Pulse Height[*]	Hygroscopic
NaI(Tl)	3.67	51.0	41	230	1.85	9% @140 keV	410	100	yes
CsI(Tl)	4.51	52	65	680 (fast, 64%) 3340 (slow, 36%)	1.80	14% @140 keV	540	49	slightly
BGO	7.13	83	8.2	300	2.15	10% @511 keV	480	13	no
YAP	5.37	36	18	27	1.95	20% @140 keV	370	45	no
LSO	7.4	66	25	47	1.82	10% @511 keV	420	75	no
LaBr$_3$(Ce)[†]	5.08	47.4	63	16	≈ 1.9	7% @140 keV 2.6% @662 keV	380	165	yes
LuAg(Pr)	6.73	62.9	22	20	2.03	4.2% @662 keV	310 (peak)		no

Table 3.1: Properties of common inorganic scintillators compared to LaBr$_3$ (data from [91–93]).

[*] The pulse height is relative to NaI(Tl) (100).

[†] The properties of LaBr$_3$(Ce) are those of the compound made commercially available by Saint-Gobain Crystal under the name of Brillance 380. The Ce^{3+} concentration is 5%, resulting in a shorter decay time.

An accurate background estimation has been performed in [94, 95], showing a self-counting rate of (0.077 ± 0.004) cps/g. The number of spurious events due to the crystal activity is therefore very small.

Two kinds of lanthanum halides scintillating detectors were available at the time of the beam test. The first one was a commercially available Brillance 380 detector by Saint-Gobain Crystals (provided with an embedded PMT) based on a $\varnothing 1'' \times 1''$ $LaBr_3$(5 %Ce) cylindrical crystal, while the second consisted in a mosaic of four $LaBr_3$(5 %Ce) crystals (Brillance 380 type) with a diameter of 0.5” and a height of 0.5”.

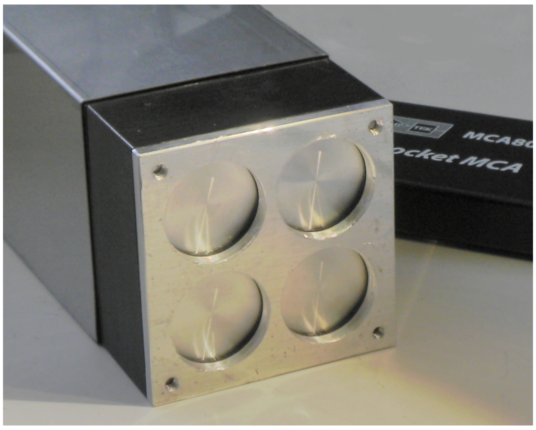

Figure 3.6: Picture of the so-called “mosaic” detection module, which is based on a 2×2 matrix of $\varnothing 0.5'' \times 0.5''$ $LaBr_3$ scintillating crystals.

The four smaller detectors were inserted in a $80 \times 80 \times 200\,mm^3$ iron box coated on its side with a 2 mm thick lead sheet, forming a 2 × 2 matrix shown in fig. 3.6. Each $\varnothing 0.5'' \times 0.5''$ crystal was coupled to a Hamamatsu R11265-200 photomultiplier tube [96] using the Dow Corning[4] optical glue.

The R11265-200 PMT window consists in borosilicate glass (pirex) on which a semitransparent layer of alkali metal (*ultra bialkali*) is deposited. The Use of ultra bialkali photocathodes boosts the PMT quantum efficiency (QE), *i.e.* the probability for an impinging photon to produce a photoelectron, from typical values of ~ 25% up to 43%. This is a great improvement in the performance of scintillator counters because the main limit in the energy resolution is given by the relatively small number of photoelectrons due to the typical small efficiency of traditional photocathodes: an increase of the 20% in QE is then fundamental to improve the energy resolution.

The four smaller crystals and their corresponding PMT were assembled by prof. Baldazzi of the Bologna INFN section; for this reason in the following they are referred to as the BO 1–4 detector, while the Brillance 380 $\varnothing 1'' \times 1''$, property of the INFN section of Milan, is indicated as $LaBr_3$ MI.

The absorption efficiency of the Brillance 380 crystal as a function of the photon energy for different crystal thicknesses is shown in fig. 3.7; in the 60–

---

[4] Web site: `http://www.dowcorning.com/`

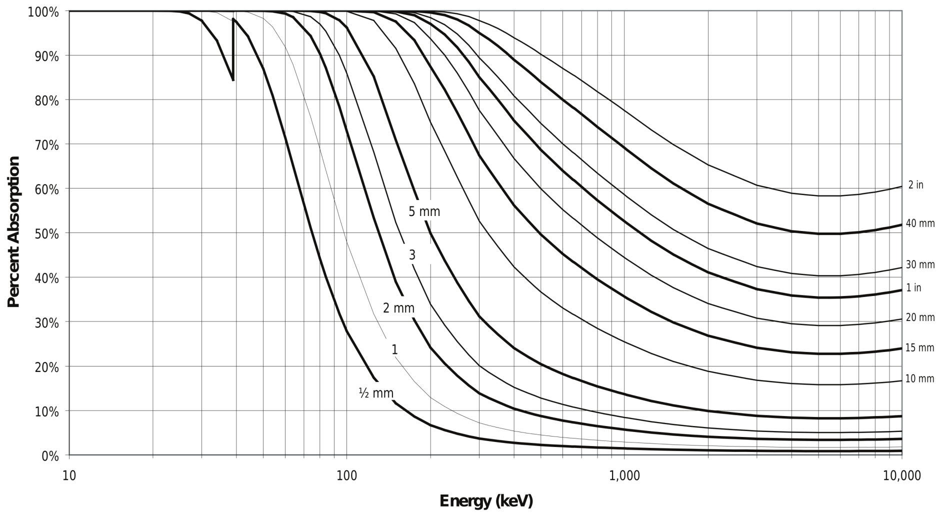

Figure 3.7: Plot of the intrinsic total efficiency of lanthanum bromide scintillators of different thickness. Photons are assumed to be normally incident on the crystal surface [97].

200 keV energy range, the detector efficiency is fully satisfactory even for a 0.5″ thick crystal, while it is smaller than 50% for photon energies larger than 500 keV.

3.2.4 *HPGe detectors*

The gold standard for X- and γ- ray spectrometry is given by High Purity Germanium solid state detectors. The scintillation counters limit on the energy resolution is caused by the inefficient conversion of the deposited energy into photoelectrons; typically each photon interaction produces only a few thousands of photoelectrons and the statistical fluctuations in such a small number place a limit on the achievable energy resolution [91].

The only way to reduce the statistical limit on the energy resolution is to increase the number of information carriers generated by the radiation interaction. In semiconductors the energy needed to excite an electron from the valence to the conduction band is of the order of the eV, to be compared with the 100 eV required for the production of a single photoelectron. This explains the wide use of semiconductors in the field of radiation detection.

The main problem in the production of semiconductor γ ray detectors is to obtain a large enough depletion region (~ 1 cm), impossible to achieve at normal semiconductor purity. Techniques to reduce the impurity concentration to the level of 10×10^{10} atoms/cm^3 (1 part in 10^{12}) have been developed for germanium, but not for silicon. Detectors manufactured from this ultra-pure germanium are usually called *high-purity germanium detectors*.

The detection of low energy X-rays does not require a huge depleted volume, but a thin entrance window is needed. ORTEC provides a detector series specifically designed for low energy spectroscopy (ORTEC GLP series Planar HPGe Low-Energy Detector [98]) consisting of planar germanium detectors of various dimensions. The planar configuration is well suited for this purpose because the p^+ electric contact on the high-purity p-type germanium bulk may be obtained by ion implantation, a technique which allows to produce a very thin contact layer (~ 300 nm) so that it can serve as entrance layer for weakly penetrating radiation [91], such as low energy X-rays.

The detector used at the beam test in RAL was a ORTEC GLP-12195/10-P from the INFN section of Milano Bicocca. This detector is based on a $\varnothing 10\,\mathrm{mm} \times 7\,\mathrm{mm}$ high-purity crystal cooled at 77 K and isolated from the environment through a 127 µm thick beryllium window. The detector presents the outstanding energy resolution typical of HPGe detectors (~ 1 keV) obtained using a 6 µs amplifier (ORTEC 672) time constant.

Another HPGe detector from the RIKEN-RAL scientific staff was installed at the beam test. This detector belongs to the ORTEC GMX series, a n-type coaxial HPGe detector with a thin entrance window made by a beryllium layer of 500 µm and a 0.3 µm p-contact on the entrance window [99].

3.3 DATA ACQUISITION

The scheme of the Data Acquisition (DAQ) system used at the RAL beam test is shown in fig. 3.8. The facility provides a trigger signal which is fed into the FAMU control board that provides the trigger with a controllable delay to the other components of the DAQ, as sketched in fig. 3.9. The signals of the $LaBr_3$(Ce) scintillating detectors were digitized by a 8-channel CAEN DT5730 500 MHz digitizer, sent to the DAQ PC and stored. The digitizer, triggered by the FAMU control board, sampled the output signal every 2 ns in a time window of 5 µs. The signal of the GLP HPGe had to go through a stage of amplification before it was amplified and shaped by a ORTEC 672 [100] amplifier with a time constant of 6 µs. Both the shaped signal and the one at the output of the preamplifier stage were digitized.

The signals from the 64 scintillating fibers of the hodoscope, readout by SiPMs, were amplified and shaped by 8 TPS boards, resulting in ~ 200 ns long signals. They are then integrated by two 32-channel CAEN V792 QDCs (Charge to Amplitude Conversion) [101] and acquired in a gate set by the FAMU control board (fig. 3.9).

The VME bus is connected to the PC responsible for the DAQ by means of a SBS Bit3 bridge with an optical link.

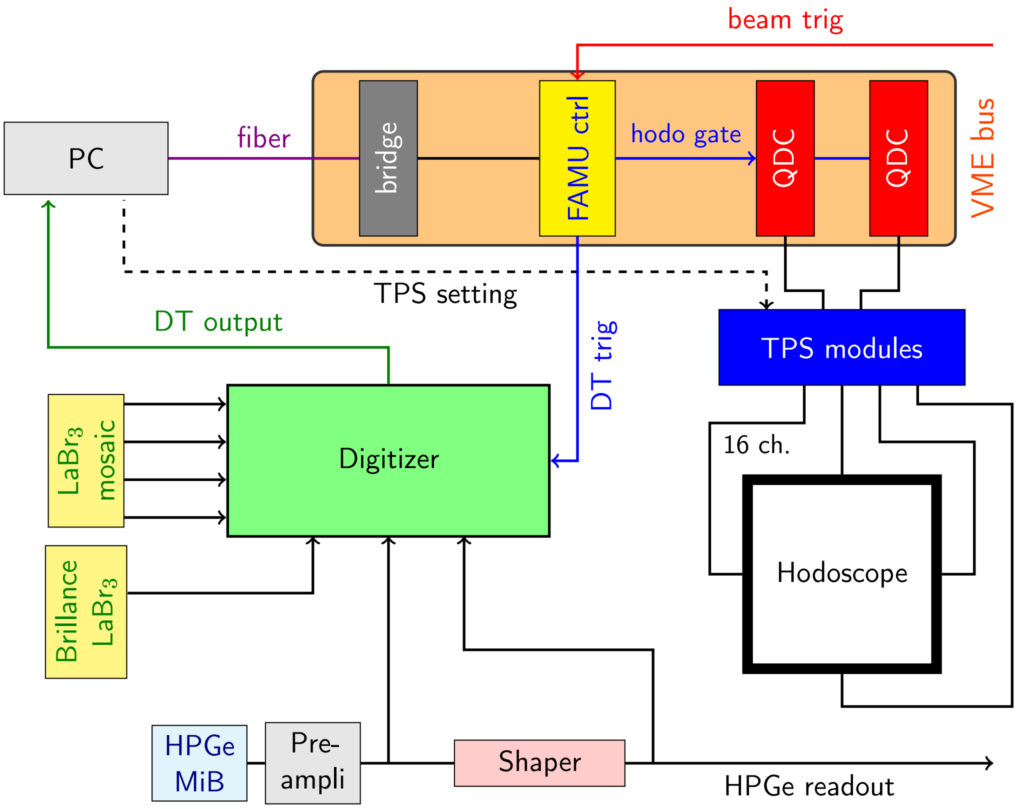
beam trig
PC
fiber
bridge
FAMU ctrl
hodo gate
QDC
QDC
VME bus
TPS setting
DT output
DT trig
TPS modules
LaBr3 mosaic
Digitizer
16 ch.
Hodoscope
Brillance LaBr3
HPGe MiB
Pre-ampli
Shaper
HPGe readout

Figure 3.8: Scheme of the Data Acquisition system used at the beam test.

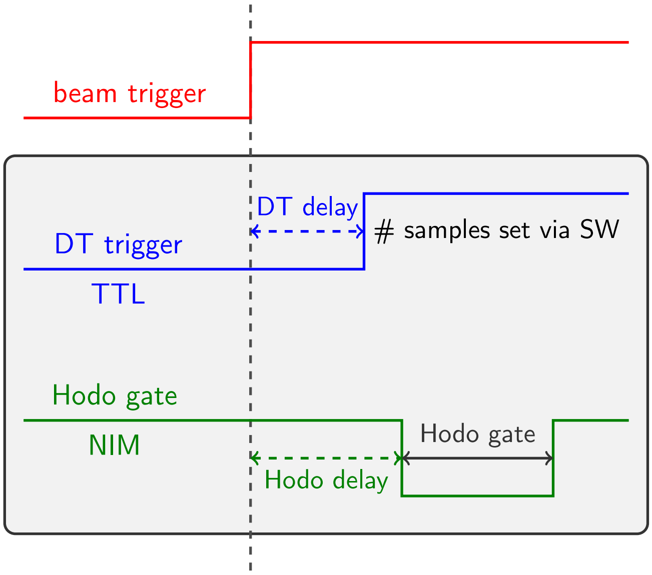
beam trigger
DT delay
# samples set via SW
DT trigger
TTL
Hodo gate
NIM
Hodo gate
Hodo delay

Figure 3.9: FAMU control board timing sketch. The board is able to set the delay for the digitizer (DT) trigger, which is a TTL signal, together with the delay and the gate for the hodoscope (hodo) set by a NIM signal.

3.4 WAVEFORM ANALYSIS STRATEGY

As mentioned earlier, the output of the five $LaBr_3$ scintillating detectors was recorded by a 500 MHz digitizer for about 5 µs after the trigger given by the FAMU control board described in the previous section. This choice came from the specific requirements of the measurement: on one side, not only the energy spectrum of the detected X-rays is interesting but also their *time distribution*, that can be easily obtained from the digitizer output once a proper analysis method is implemented. On the other hand, the background and, in particular, the event rate in the detectors were unknown; from the analysis of the full waveform of the signal one can discriminate single-pulse from pile-up events, and (may eventually) recover information from pile-up events that otherwise would be excluded.

The output of the digitizer consists of a short-int array of 2560 components. Two typical examples of the digitizer output coming from the $LaBr_3$ scintillating detectors (after the inversion of the signal and the subtraction of the baseline) are shown in fig. 3.10. Fig. 3.10b underlines the need of a method to identify and analyse the single- and multi-pulse events recorded by the digitizer.

The first step in the analysis process is the identification of the pulses in the waveform. This can be done by using (in a slightly improper way) the `TSpectrum` class of the `ROOT` data analysis framework [102]. This class is based on the code originally developed by Miroslav Morhac [103–105] to analyse γ and X ray spectra and includes a method called `Search` aimed at identifying and localizing the peaks in the energy spectra; thus it can be used to identify pulses in the waveform.

The `Search` method output consists of the number N of found peaks and two arrays: one with the position of the pulses and one with their height. From these "pulses", events with a pulse height (PH) smaller than a certain threshold are discarded in order to exclude fake low energy events that are actually due to baseline fluctuations.

At this point, another kind of filter is needed. In fig. 3.11 the signal output from the four $\varnothing 0.5'' \times 0.5''$ (BO 1–4) $LaBr_3$ detectors is shown. It is clear that when one of the detectors records a high energy event (that may even saturate the output), a spike appears in all the other detectors. This sort of *pick-up* noise was probably due to some interference in the power supply chain and is larger than any reasonable pulse-height threshold. Anyway, given the spikes are much more faster than the true pulses coming from the scintillating detector, a filter based on the signal recovery time was implemented. This is done computing the time needed for the baseline restoration starting from the pulse position previously obtained by the `TSpectrum Search` method. A threshold of 40 ns in the recovery time is set. In this way, these events are completely rejected.

After these preliminary "data-cleaning" operations, some of the N pulses initially identified by the `Search` method have been excluded from the analysis.

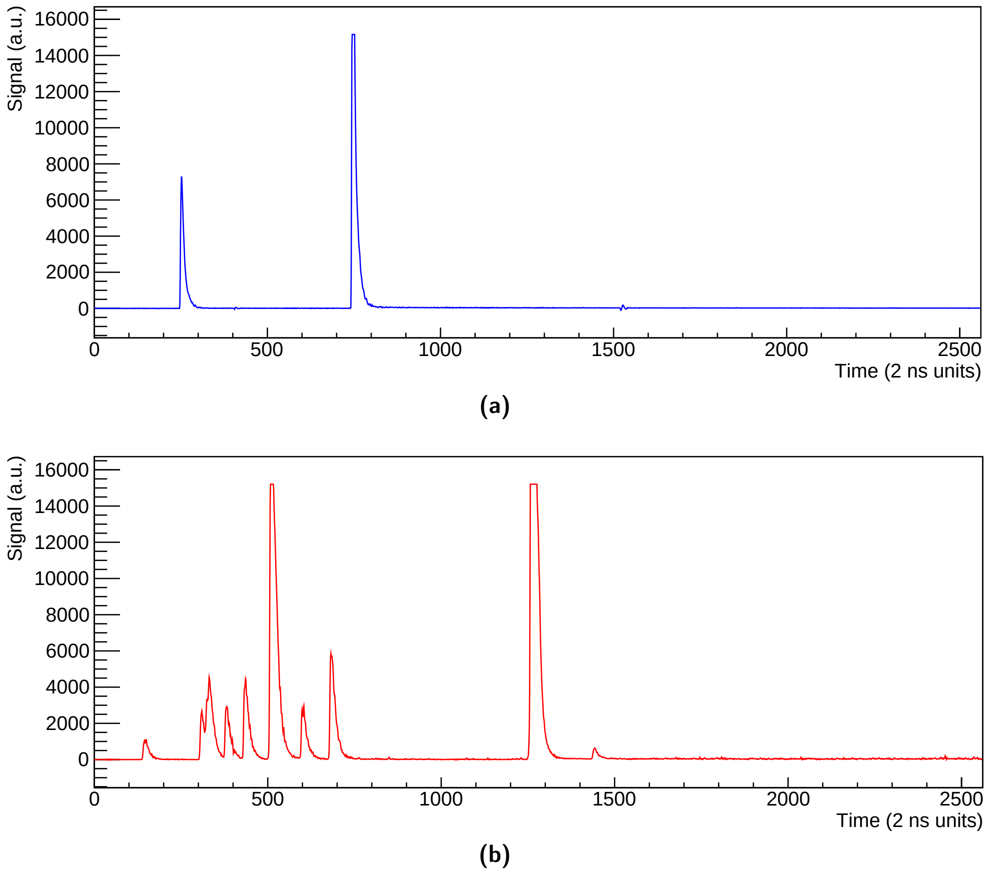

Figure 3.10: Two examples of the digitizer output of the $LaBr_3$ detector in case of **(a)** low and **(b)** high event rate.

Starting from the first of the survived pulses in the digitizer output, the pulse starting time and the time for the baseline restoration are evaluated. In this time region there can be just one pulse or more (fig. 3.12). The signal between the pulse start and the baseline restoration, together with the number of pulses in this region, are used to define a custom `Peak` object.

To solve the problem of pile-up, a fit of the whole time-window is performed with the `ScanPeak` method implemented in the `Peak` class. The fit uses Landau functions[5] to model pulses because of their simple form (three free parameters) that ensure a high convergence rate nevertheless providing good results. The result of this procedure applied to the pulses in fig. 3.12 is shown in fig. 3.13.

In this way, every pulse is associated to a Landau function, described by a `TF1` object in the `ROOT` framework, from which it is straightforward to obtain the properties of the single pulse, such as its height (PH), its integral (PI), its starting time and its FWHM.

---

[5] CERN-Root package reference internet page:
`http://root.cern.ch/root/html/TMath.html#TMath:Landau`

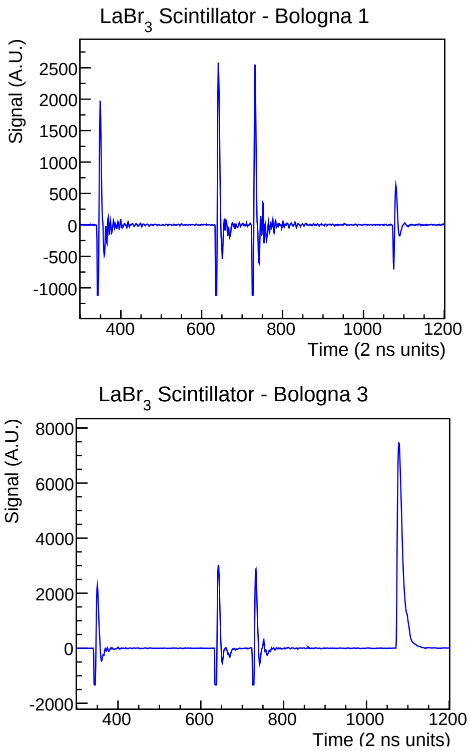

Figure 3.11: Signal output from the four $\varnothing 0.5'' \times 0.5''$ (BO 1–4) $LaBr_3$ detectors. When one of the detectors records a high energy event, a spike appears in all the other detectors.

3.4.1 *Calibration and performance of the LaBr$_3$ scintillating detectors*

All the five $LaBr_3$ scintillating detectors were carefully calibrated and re-tested in the Insulab laboratory in Como after the beam test in RAL using the same conditions of the beam test. The calibration was performed with radioactive sources of ^{241}Am, ^{226}Ra, ^{137}Cs and ^{60}Co and was useful to test the off-line analysis procedure described in the previous section.

As mentioned earlier, the analysis procedure associates a Landau function to each pulse, allowing an easy access to the pulse features. In order to obtain the energy deposited in the detector, the height and the integral of any single pulse were evaluated. In particular, the pulse integral was computed in the range between the time t_1 and t_2 corresponding to the 80% of the maximum of the signal, as shown in fig. 3.14a. The variation in the integral range did not influence the results in terms of energy resolution and linearity of the detector response. From fig. 3.14b one can observe the not surprising correlation between the height and the integral of the pulses, that allows to perform a parallel analysis of both the PH and PI distribution.

Fig. 3.15 shows a part of the ^{226}Ra γ ray spectrum in both the cases of the pulse integral (PI) and the pulse height (PH) distribution.

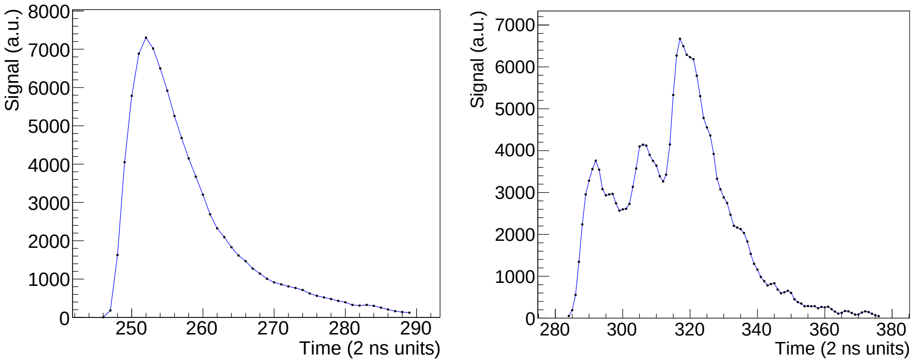

(a) single-pulse event **(b)** multi-pulse event

Figure 3.12: Example of single- and multi-pulse events in the digitized output of the $LaBr_3$ scintillating detector.

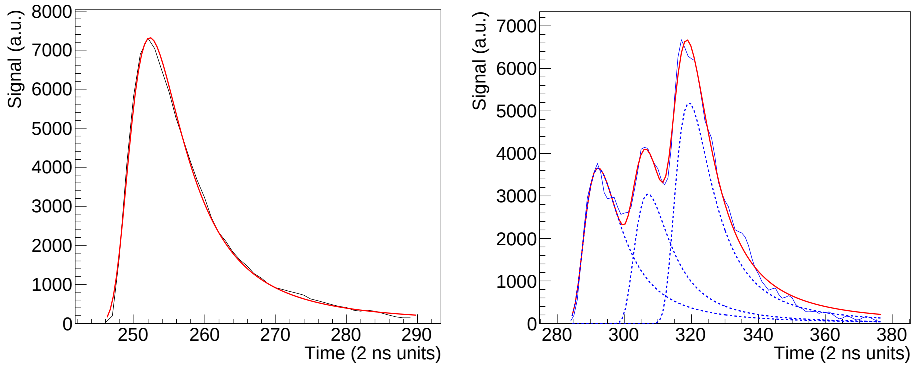

(a) single-pulse event **(b)** multi-pulse event

Figure 3.13: Example of single- and multi-pulse events processed by the `ScanPeak` method.

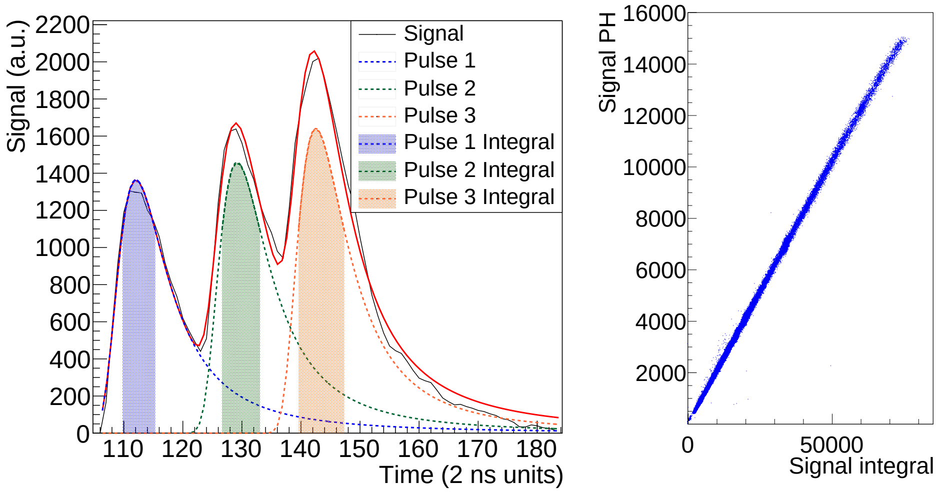

(a) **(b)**

Figure 3.14: (a) Example of the pulse integration domain. **(b)** Correlation between the pulse height and its integral for γ rays from ^{226}Ra.

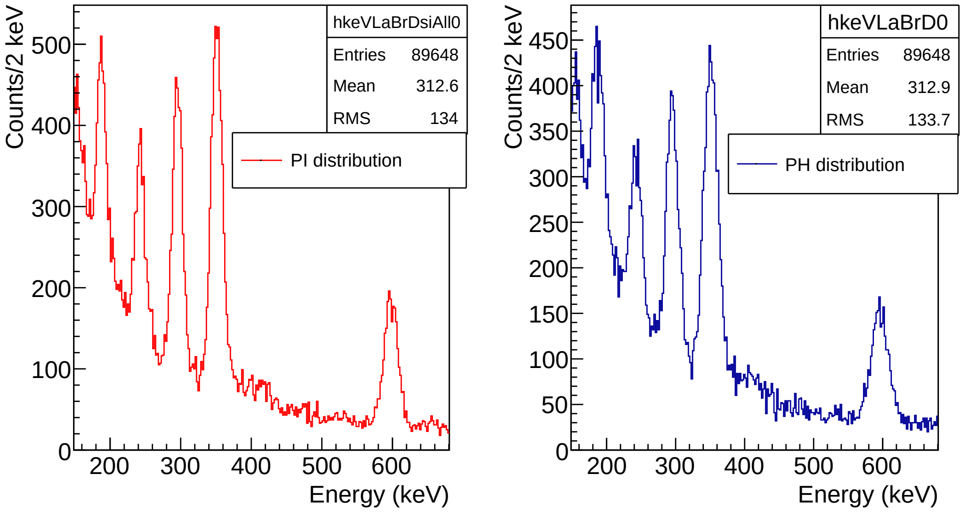

Figure 3.15: A fraction of the ^{226}Ra spectrum obtained by the distribution of the pulse integral (left, red) and of the pulse height (right, blue) using one of the $\varnothing 0.5'' \times 0.5''$ detectors.

$\varnothing 0.5'' \times 0.5''$ LaBr$_3$ scintillator - BO 1

linear fit in the range 50–700 keV

PH ANALYSIS			PI ANALYSIS		
Energy (keV)	FWHM/mean (%)	Data-Fit (lin, %)	Energy (keV)	FWHM/mean (%)	Data-Fit (lin, %)
59.5	17.7466	-0.212093	59.5	14.6443	-0.117123
242	6.83959	1.41281	242	5.99789	1.24597
295	6.29775	1.32312	295	5.20349	1.23898
352	6.5827	1.05737	352	5.1982	0.900197
609	5.02451	-0.798024	609	3.83352	-0.655977
661.5	4.86031	-0.167168	661.5	3.9364	-0.244861
1173	3.46223	-4.50921	1173	2.66325	-3.73608
1333	3.02198	-6.20488	1333	2.70729	-4.94441

$\varnothing 0.5'' \times 0.5''$ LaBr$_3$ scintillator - BO 2

linear fit in the range 50–400 keV

PH ANALYSIS			PI ANALYSIS		
Energy (keV)	FWHM/mean (%)	Data-Fit (lin, %)	Energy (keV)	FWHM/mean (%)	Data-Fit (lin, %)
59.5	16.0448	-0.0615576	59.5	13.2688	-0.036986
242	5.65531	0.935781	242	5.28758	0.557981
295	5.66562	0.321958	295	4.94498	0.225936
352	5.6423	-0.26034	352	4.71787	-0.143653
609	4.21209	-3.71544	609	3.52247	-2.22217
661.5	3.98937	-5.15925	661.5	3.58988	-3.379

Table 3.2: Performance of two (BO 1 and BO 2) of the four $\varnothing 0.5'' \times 0.5''$ LaBr$_3$ scintillating detectors.

The performance of the five scintillating detectors in terms of energy resolution and deviation from linearity are summarized in tab. 3.2, 3.3 and 3.4.

From the parallel analysis of the pulse height and pulse integral spectra it can be noticed that the energy resolution (FWHM/mean) obtained from the distribution of the PI is always better than the one measured with the PH distribution. The energy resolution obtained with the integration of the signal is in good agreement with the values reported in literature obtained with standard spectroscopic techniques, while the one coming from the pulse height distribution is slightly worse.

The calibration results show a surprisingly large deviation from linearity in the detector response. This cannot be ascribed to a non-proportionality in the crystal light yield, because several works have shown that this is of the order of 2–5% in the energy range of interest [106]. This non linearity is thus probably originated in the PhotoMultiplier Tubes for one of the following reasons [107, 108].

The PMTs were operated at high voltage (−880 V) to obtain a clear pulse signal over the baseline in the 50–700 keV region of the energy spectrum, but a too

$\varnothing 0.5'' \times 0.5''$ $LaBr_3$ scintillator - BO 3

linear fit in the range 50–700 keV

PH ANALYSIS			PI ANALYSIS		
Energy (keV)	FWHM/mean (%)	Data-Fit (lin, %)	Energy (keV)	FWHM/mean (%)	Data-Fit (lin, %)
59.5	15.325	-0.260401	59.5	13.179	-0.0994175
242	6.37454	1.5179	242	5.70411	1.25772
295	5.84293	1.28021	295	4.94353	0.975065
352	5.74092	1.13457	352	4.8812	0.663718
609	4.37709	-0.099341	609	3.62766	-0.173637
661.5	4.25826	-0.560351	661.5	3.67066	-0.373145
1173	2.76356	-4.98205	1173	2.57176	-3.39593
1333	2.14976	-6.73531	1333	2.30206	-4.3976

$\varnothing 0.5'' \times 0.5''$ $LaBr_3$ scintillator - BO 4

linear fit in the range 50–400 keV

PH ANALYSIS			PI ANALYSIS		
Energy (keV)	FWHM/mean (%)	Data-Fit (lin, %)	Energy (keV)	FWHM/mean (%)	Data-Fit (lin, %)
59.5	15.5849	-0.0104021	59.5	13.467	-0.00946371
242	6.02417	0.289699	242	5.47546	0.308248
295	5.59872	0.295485	295	4.92591	0.322088
352	5.58041	-0.174339	352	4.52501	-0.167537
609	4.28484	-2.14126	609	3.56504	-1.65222
661.5	4.07377	-3.39046	661.5	3.44921	-2.73596

Table 3.3: Performance of two (BO 3 and BO 4) of the four $\varnothing 0.5'' \times 0.5''$ $LaBr_3$ scintillating detectors.

$\varnothing 1'' \times 1''$ $LaBr_3$ scintillator - MI-1

linear fit in the 50–400 keV range

PH ANALYSIS			PI ANALYSIS		
Energy (keV)	FWHM/mean (%)	Data-Fit (lin, %)	Energy (keV)	FWHM/mean (%)	Data-Fit (lin, %)
59.5	14.6036	-0.137984	59.5	12.7544	-0.0549587
242	4.95399	2.93871	242	4.48343	1.42519
295	4.65226	1.7591	295	4.11013	0.793082
352	4.20262	-0.787512	352	4.08191	-0.483652
609	2.51576	-15.5447	609	2.89033	-8.23391
661.5	2.38556	-18.1084	661.5	2.7273	-9.69205

Table 3.4: Performance of the $\varnothing 1'' \times 1''$ $LaBr_3$ scintillating detector.

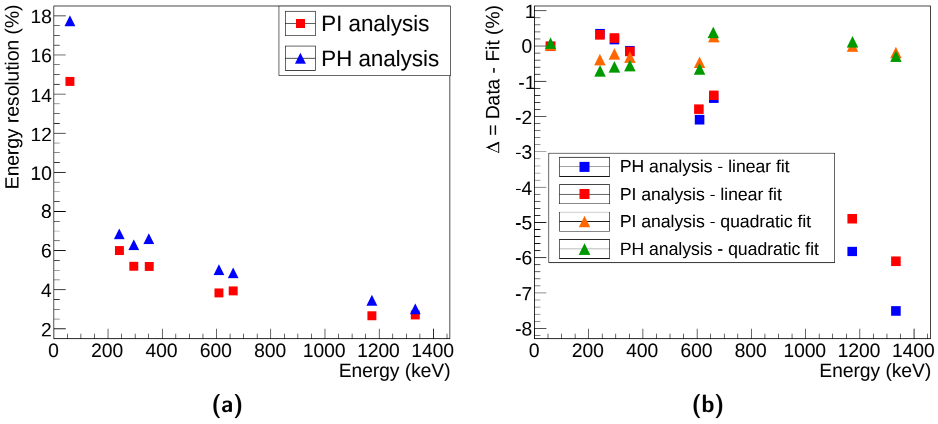

Figure 3.16: Energy resolution **(a)** and deviation from the calibration values **(b)** for the BO 1 detector obtained using the different methods described in the text.

large current may cause the potentials of the voltage divider to be redistributed and, as a result, the voltage between the dynodes and between the final dynode and the anode change.

In addition, when a large amplitude pulse current, such as the one generated by the intense and fast light output of a $LaBr_3$(Ce) crystal (~ 25 times larger than the one generated by NaI(Tl)), flows through the PMT, space charges are formed between the last dynodes, as well as between the final dynode and the anode. This change in the spatial charge distribution opposes the acceleration of electrons reducing the secondary emission ratio and the efficiency of electron collection in the anode, and thus the pulse amplitude.

While one expects that the energy resolution measured using the PI distribution could be better than the one obtained from the PH spectrum, it is interesting to note that using the pulse integral distribution seems to reduce these non-linearity effects. This is particularly evident in the performance of the MI-1 detector (tab. 3.4) that exhibits the strongest non-proportional behaviour; in this case the deviation from linearity at 662 keV measured with the PI analysis is about half of the one obtained from the PH distribution.

In order to correct the effect of non-proportionality in the detector response, a second-order polynomial fit was used to calibrate the detectors. The energy resolution measured with both the PI and PH analysis and the value

$$\Delta = \frac{(\text{data} - \text{fit})}{E_{\text{true}}}$$

for the BO 1 detector are shown in fig. 3.16. As can be noticed, a quadratic calibration curve reduces the effect of non-linearity keeping the deviation from the calibration value below 1%.

CHAPTER 4

DESCRIPTION OF THE RESULTS

The beam test of June 2014 at RAL provided a large amount of data. In this chapter, after a brief description of the set-up geometry (sec. 4.1) and of the procedure used for the choice of the optimal beam energy (sec. 4.2), the preliminary results of the analysis will be shown.

As mentioned earlier in chapter 3, four different targets were tested: a graphite block and three gaseous target consisting of pure hydrogen, a hydrogen–argon mixture and a hydrogen–carbon dioxide mixture. The main goal of the beam test at RAL was to prove that a X-ray detection system based on $LaBr_3$ scintillating crystals fits the requirement of the proposed experiment both in terms of energy and time resolution. From the preliminary results of the analysis presented in sec. 4.3, one can see that the $LaBr_3$ scintillating detectors were able to measure all the expected peaks due to the various muonic atoms transitions, hence the performance of the $LaBr_3$ counters completely meets the expectations in this sense. On the other hand, a relevant background was also found in the scintillating counters spectra and its origin is not completely understood yet.

Also for what concerns the time spectra the situation is not so clear. Indeed, dedicated Monte Carlo simulations require to be implemented in order to understand the obtained time spectra.

4.1 GEOMETRICAL DESCRIPTION OF THE EXPERIMENTAL SET-UP

The experimental set-up, whose parts have been described in the previous chapter, was installed in the experimental Port 4 (fig. 3.2) where the measurements were performed. Figure 4.1 shows the installation of the detector system at RAL without the gas target. The last collimator stage was removed from the beam pipe in order to make room for the experimental set-up; the hodoscope was placed right in front of the pipe window and the four $LaBr_3$ BO 1–4 mosaic detectors were situated at about 17 cm from the beam axis, while the $LaBr_3$ MI detector was placed ~ 1 cm under the gas target, in front of a dedicated window in the vessel support.

Given the larger solid angle covered by the $\varnothing 1'' \times 1''$ $LaBr_3$ MI detector, about a half of the events recorded by the $LaBr_3$ scintillating counters was obtained by

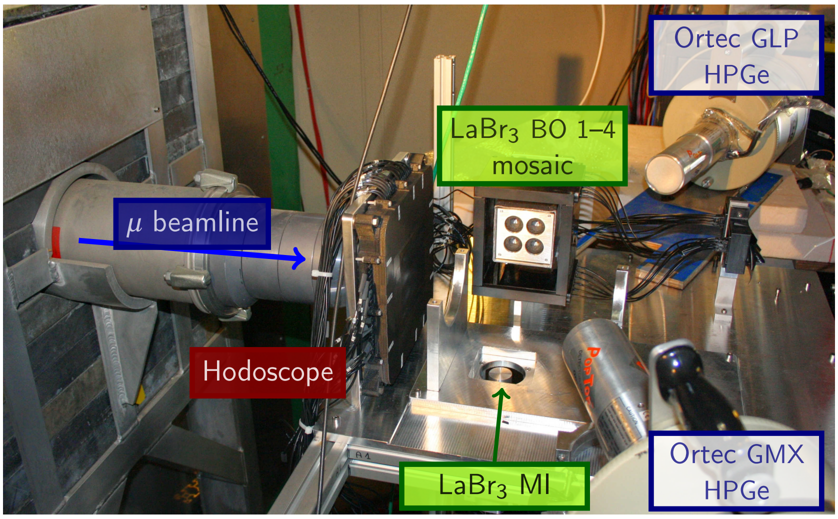

Figure 4.1: Picture of the experimental set-up installed at the experimental port-4 at the RIKEN-RAL muon facility.

this detector. The proximity of the $LaBr_3$ MI detector to the target results in a much higher rate with respect to the four $LaBr_3$ BO detectors that, in addition to their smaller area (∅0.5″), are placed at a larger distance from the target. The high count rate is such that about 25% of the recorded events are labelled as multi–pulse events (see sec. 3.4).

In contrast, the HPGe detectors were placed far from the target because, given their large shaping time (6 µs), a high-rate environment would have induced a constant pile-up in the detector, causing the output saturation. The energy spectra acquired with the GLP-HPGe detector shown in this chapter have been obtained from the distribution of the pulse-height of the shaped signal acquired by the digitizer.

4.2 BEAM ENERGY CALIBRATION

The momentum of the muon beam of the RIKEN–RAL facility described in the previous chapter can vary in the 20–120 MeV/*c* range. To obtain the largest achievable number of muonic hydrogen atoms, a tuning of the beam energy was needed. The simulations of the muon interaction in the target (fig. 4.2) indicate that the best energy is the 60–64 MeV/*c* range. The fine tuning was performed by counting with the HPGe detector the oxygen characteristic X-rays for different beam energies when the gas target filled with the H_2–CO_2 mixture (sec. 4.3.4) was exposed to the muon beam. The maximum number of X-rays with an energy corresponding to the $2P \rightarrow 1S$ transition in muonic oxygen occurred at 61 MeV/*c*, hence this was considered the optimal energy for the data acquisition.

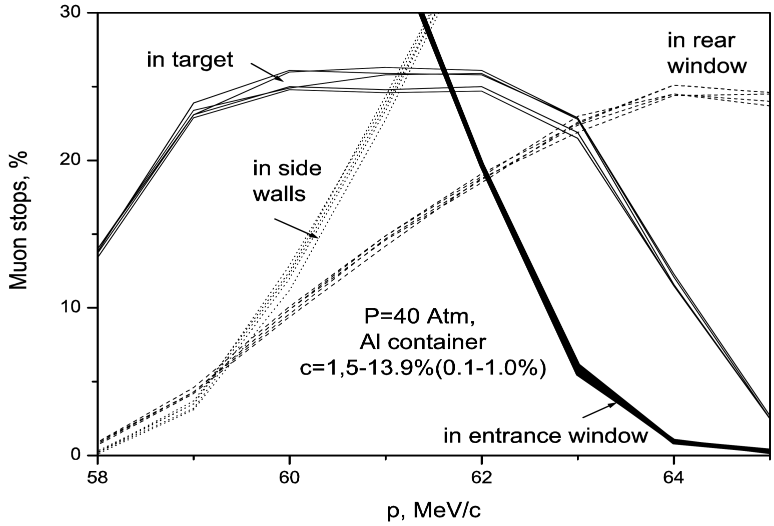

Figure 4.2: Fraction of muons stopped in the entrance window, in the target and in the rear wall as a function of the muon beam momentum obtained with a Monte Carlo simulation [109].

4.3 DATA ANLYSIS

The first aim of the 2014 beam test was to determine the suitability of the detectors described in the previous chapter for the proposed measurement. As already outlined in chapter 3, at the time of the beam test there was no idea of the background induced by the intense muon flux provided by the RAL accelerator complex, hence also the complete saturation of the detectors was considered as a possible scenario.

In an environment with a large background, also the detection of characteristic X-rays was not taken for granted: for this reason different elements were tested using a graphite target (pure carbon) and an aluminium vessel filled with several mixtures of hydrogen and other gases. The first task of the analysis is thus to identify the peaks due to the characteristic X-rays of the muonic atoms in the energy spectrum obtained by the HPGe and the $LaBr_3$ detectors.

However, as was pointed out in chapter 2, the X-ray spectrum is not the only object of interest in the proposed measurement; the event time distribution in fact has a very important role. The time spectrum is particularly important for the gas target, especially for the H_2–CO_2 mixture, since oxygen is the main candidate for a muon-transfer experiment given the energy dependence of the transfer rate at epithermal energies.

4.3.1 *Graphite target*

The first and simplest target that was considered was a small high-purity ~ 1cm thick graphite block. From a block of such a pure material, only the

Transition	Transition energy for various elements (keV)				
	C	N	O	Al	Ar
K_α	75.258	102.556	133.535	346.828	644.004
K_β	89.212	121.547	158.422	412.877	770.6
K_γ	94.095	128.194	167.125	435.981	815.0
L_α			24.830	65.756	126.237
L_β			33.521	88.771	170.420
L_γ				99.423	190.870

Table 4.1: Relevant transition energies for the muonic atoms formed by the selected elements [72, 110–112].

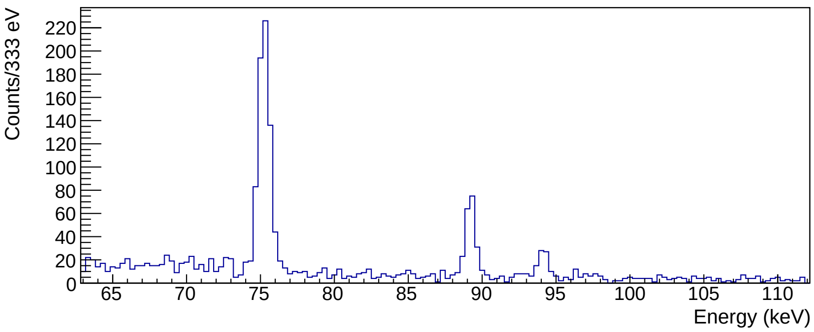

Figure 4.3: The three lines at 75.26, 89.21 and 94.1 keV of muonic carbon in the energy spectrum of the HPGe detector.

characteristic X-rays of carbon are expected. The relevant transitions in the muonic carbon atom (μC) are [72] the K_α (75.2588 keV), K_β (89.212) and K_γ (94.095 keV) lines (see tab. 4.1).

The purity of the target was confirmed by the X-ray spectrum measured by the HPGe detector (fig. 4.3), where all the lines can be ascribed to muonic carbon.

The X-ray spectrum recorded by the $LaBr_3$ detectors is shown in fig. 4.4. The better energy resolution of the spectrum obtained with the pulse-integral distribution with respect to the one obtained with the PH is evident from the separation between the main peak at 75.26 keV and the ones at 89.21 and 94.1 keV, that cannot be individually resolved. Given the better performance in terms of energy resolution, all the spectra presented in the rest of the chapter are obtained with the PI method.

The time distribution of the X-rays detected by the four BO-1–4 and the $LaBr_3$ MI scintillating detectors is reported in fig. 4.5. Observing the time spectrum one can notice two intense peaks with FWHM ≈ 70 ns separated by 320 ns corresponding to the two beam spills (fig. 3.3). A large number of X-rays are then emitted immediately after the muon interaction with the target, and in the following these events are referred to as *prompt* events. After the two pulses,

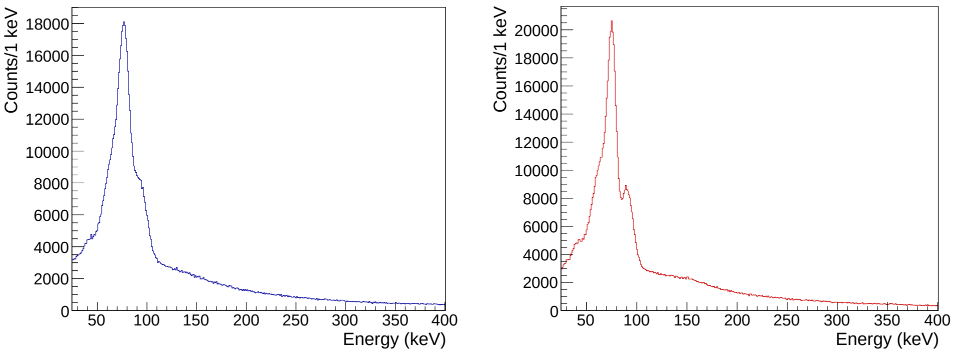

(a) PH distribution **(b)** PI distribution

Figure 4.4: X-ray spectrum of the graphite target measured with the $LaBr_3$ scintillating detectors and obtained from **(a)** the PH and **(b)** the PI distributions.

the number of recorded events decreases exponentially with a time constant $\tau_{\mathrm{Bo}} = 1977 \pm 5\,\mathrm{ns}$ for the BO detectors and $\tau_{\mathrm{Mi}} = 1989 \pm 7\,\mathrm{ns}$ for the MI detector. This exponential tail is actually the sum of two exponentials: one with the slope set by the free muon decay rate $\lambda_0^{-1} = \tau_0 = 2196.98\,\mathrm{ns}$ and the other with the slope given by the lifetime of the μC atom, which is $\approx 2020\,\mathrm{ns}$ ([113] and references therein) and dominates in this situation.

Selecting the events recorded during the beam spill (*i.e.* the ones under the two pulses in fig. 4.5), and considering their energy spectrum, it can be noticed (fig. 4.6) that most of the carbon characteristic X-rays are emitted promptly after the muon interaction, while events occurring outside the two pulses (here generically labelled as *delayed*) may be ascribed to electrons with the muon decay or γ- and X-rays following the muon capture process, which generate a diffuse background with a peak at 511 keV. The origin of this peak is not completely understood yet: contributions from the internal radioactivity of the $LaBr_3$ detectors and from the environment should not be so relevant; the main suspects for this peak are the electrons from muons decay. The electrons generated by the decay of the muons in fact may have an energy of the order of 50 MeV, thus it is possible that small electromagnetic showers may develop in the lead shield of the $LaBr_3$ mosaic or in the aluminium coating of the crystals.

In general, the origin of this background is somehow unclear, and it will be a constant presence also for the various gas targets described in the following sections.

4.3.2 *Pure hydrogen target*

Among the different gaseous targets, the simplest one is a pure hydrogen target. While muonic hydrogen transitions are not expected to give any contribution in the X-ray spectrum, the aluminium of the vessel must be considered. Fig. 4.2 shows that a large number of muons is stopped in the walls of the alu-

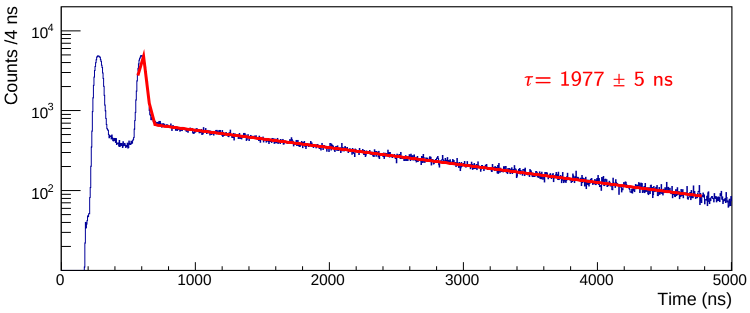

(a) LaBr$_3$ BO mosaic

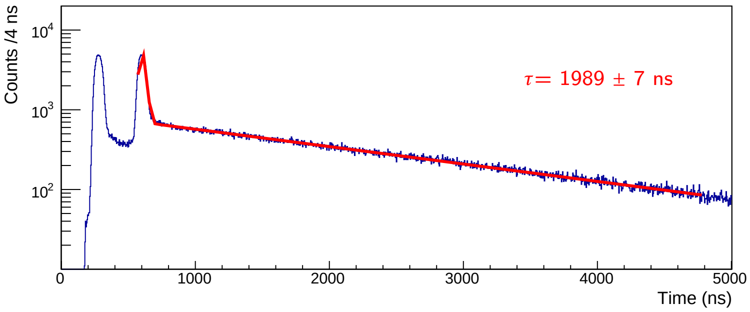

(b) LaBr$_3$ MI

Figure 4.5: Time spectrum of the events recorded by the LaBr$_3$ scintillating detectors for the graphite target. The exponential decay is characterized by a time constant of $\tau_{\mathrm{Bo}} = 1977 \pm 5\,\mathrm{ns}$ for the BO detectors and $\tau_{\mathrm{Mi}} = 1989 \pm 7\,\mathrm{ns}$ for the MI one.

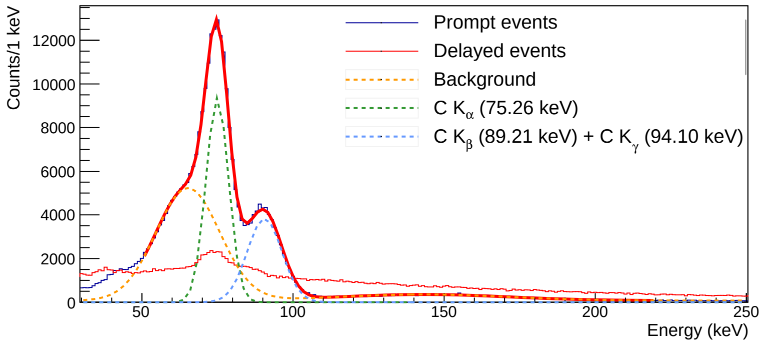

(a) LaBr$_3$ BO 1–4 Mosaic

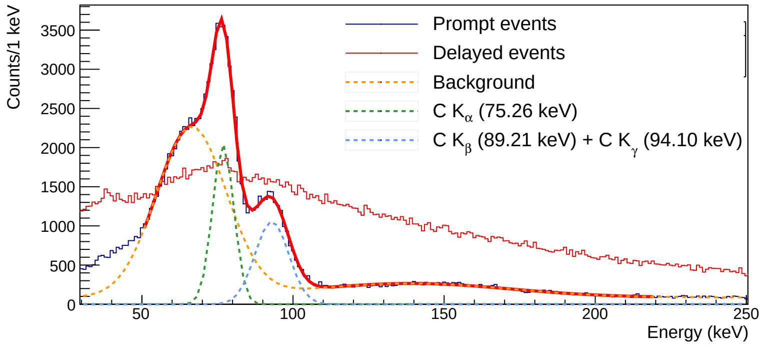

(b) LaBr$_3$ MI

Figure 4.6: X-ray spectrum of the graphite target obtained with the LaBr$_3$ scintillating detectors. The muonic carbon lines can be distinguished clearly in the prompt events spectrum.

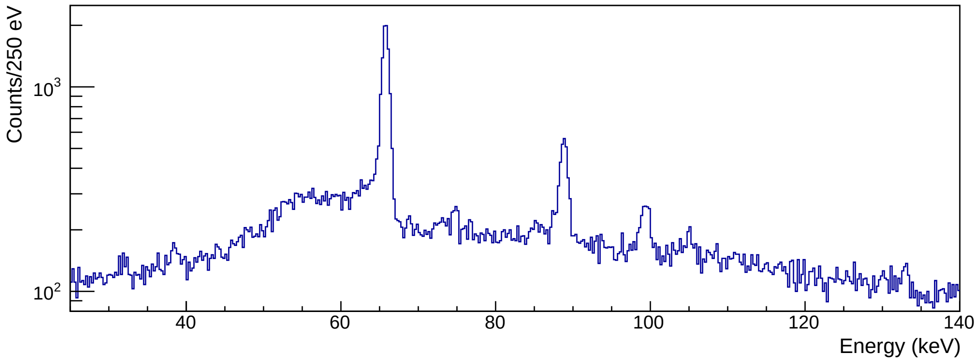

Figure 4.7: Energy spectrum recorded by the HPGe detector for the pure H_2 target. The three lines are due to the L_α (65.756 keV), L_β (88.771 keV) and L_γ (99.423 keV) transition of the muonic aluminium atoms.

minium vessel where they form μAl atoms. A study of a pure H_2 target is thus needed in order to understand the background due to aluminium characteristic X-rays.

In the X-ray spectrum obtained by the HPGe detector (fig. 4.7) only the characteristic X-rays of aluminium are present. This is an evidence that there are no contaminations in the gas target.

The X-ray spectrum obtained using the $LaBr_3$ scintillating detectors (fig. 4.8) confirms the observation of the characteristic lines of aluminium, including the K-lines (346.828, 412.877 and 435.981 keV) that were not recorded by the HPGe detector because they were out of its energy range. When considering the delayed events detected by the $LaBr_3$ scintillation counters, the peak at 511 keV is still present. Considering gaseous targets, an additional contribution to this peak may come from the development of small electromagnetic showers in the vessel walls. However, a dedicated Monte Carlo simulation has to be implemented in order to confirm this hypothesis.

The time spectrum of the recorded events is not as simple as the one of the graphite case. The time distribution is the sum of the free-μ decay distribution, the μp decay distribution and the time distributions of the decays of other muonic atoms. In particular, the μp lifetime varies with the hydrogen pressure (here 35 bar), and its contribution in this case is difficult to estimate because there is no experimental indication of the number of μp formed inside the target nor of the exact effect of such a high pressure on the μp lifetime. As shown above, muonic aluminium is the only muonic atom formed apart from μp and has a lifetime of $\approx$ 880 ns [113]. None of these processes involve directly the emission of a X-ray, but the electrons emitted in the muons decays can generate photons interacting with the target walls or deposit part of their energy directly in the $LaBr_3$ crystals. The contribution to the background of electrons interacting with the scintillating crystals must be studied with a dedicated simulation, but it can also be removed by means of an anti-coincidence veto based on plastic scintillators.

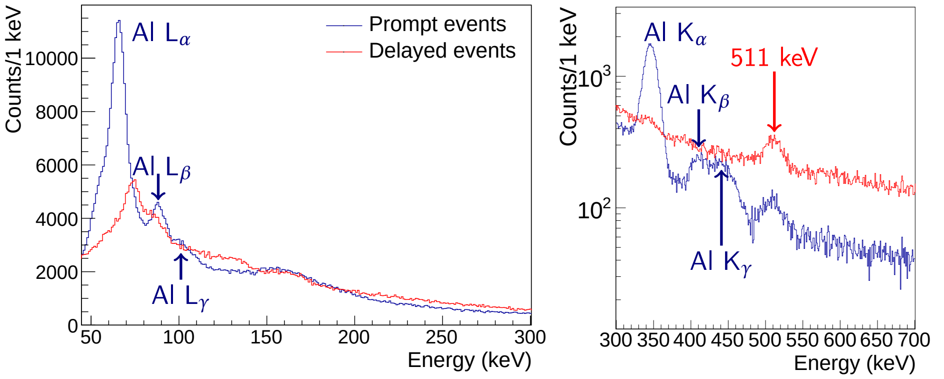

(a) LaBr$_3$ BO 1–4 mosaic

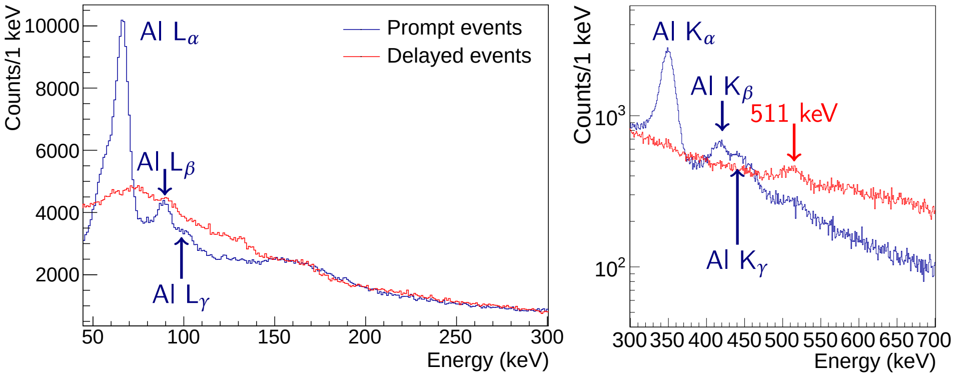

(b) LaBr$_3$ MI

Figure 4.8: X-ray spectrum obtained with the LaBr$_3$ scintillating detectors for the H$_2$ target.

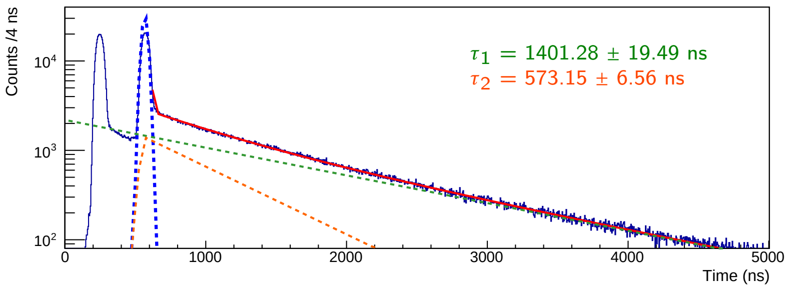

(a) LaBr$_3$ BO 1–4 Mosaic

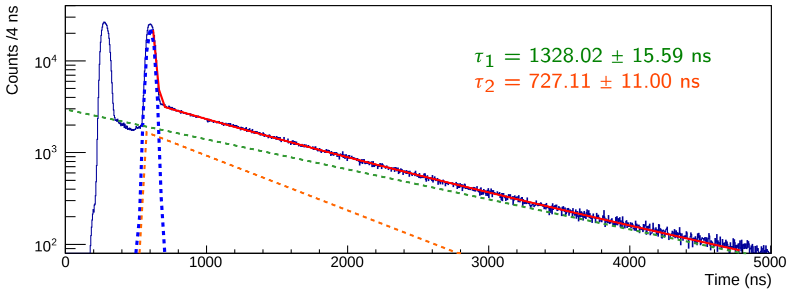

(b) LaBr$_3$ MI

Figure 4.9: Time spectrum of the recorded events for the H_2 target. The solid red line is the fitted function. The dashed green line describes the exponential decay in the far delayed range with the τ_1 characteristic time, while the orange dashed line corresponds to the function in eq. (4.1) (the τ_2 characteristic time). Finally, the dashed blue line represents a gaussian function that models the prompt peak. The same color convention is adopted for all the figures of this kind in the rest of the chapter.

The sum of all these different terms results in a time distribution which is far from being described by a single exponential. As a first approximation, the distribution of the delayed events has a double-exponential shape (fig. 4.9). The fit in fig. 4.9 has been performed fixing the τ_1 characteristic time of the exponential in the far delayed range (3500–4900 ns) and using a function of the type

$$C \cdot \left(e^{-x/\tau_2} - e^{-x/\tau_r}\right) \tag{4.1}$$

to take into account the correction of the single exponential for times closer to the prompt peak, which is modelled using a gaussian function. The exponential with the smaller decay time describes events which can be ascribed to the decay of the muonic atom with the shortest lifetime. The τ_1 and τ_2 characteristic times obtained from the fits in fig. 4.8 are $\tau_1 = 1401.28 \pm 19.49$ ns and $\tau_2 = 573.15 \pm 6.56$ ns for the data collected by the four BO detectors, while for the MI detector the values are $\tau_1 = 1328.02 \pm 15.59$ ns and $\tau_2 = 727.11 \pm 11$ ns.

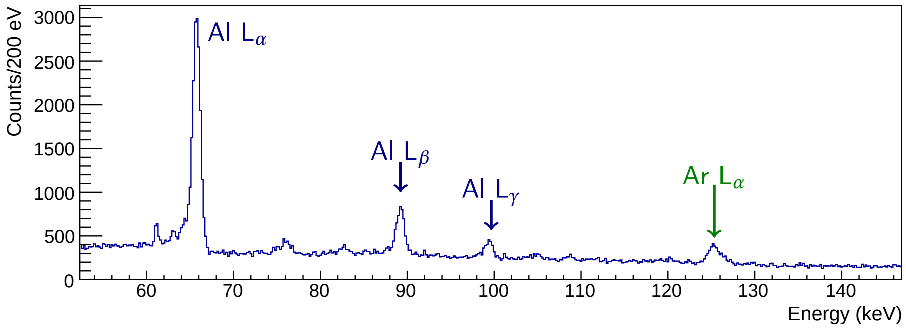

Figure 4.10: Energy spectrum obtained with the GLP HPGe detector for the H_2–Ar target.

4.3.3 *Argon target*

The muon transfer rate to argon, as to many other elements, has been studied in the past in the framework of muon-cathalized fusion and showed a slight energy dependence in the epithermal range. For this reason a mixture of hydrogen and argon at a pressure of 40 bar was chosen to be tested. The argon mass concentration was 2%, which resulted in an atomic concentration c_{Ar} of about 1.03‰.

In the energy spectrum recorded by the GLP HPGe detector, shown in fig. 4.10, only the aluminium lines together with the argon L_α peak are present, confirming the purity of the gas mixture.

The spectrum obtained from the $LaBr_3$ scintillating detector allows to detect also the argon K_α transition at 673 keV (fig. 4.11). As in the case of the pure-hydrogen target, a peak at 511 keV appears in the delayed spectrum, but this time there is also a peak at 400 keV which has not been explained yet.

Also in this case, the time distribution (fig. 4.12) of the delayed events cannot be described by a single exponential. With respect to the pure-hydrogen target, an additional contribution from the decay of μAr atoms (which have a lifetime[1] of 550 ns [113]) is present. Performing the same kind of fit used in the previous section, values of $\tau_1 = 875.77 \pm 7.19$ ns and $\tau_2 = 580.30 \pm 9.72$ ns are obtained for the data collected by the $LaBr_3$ MI detector, while for the events recorded by the $LaBr_3$ BO 1–4 mosaic one finds $\tau_1 = 892.78 \pm 9.14$ ns and $\tau_2 = 468.94 \pm 5.56$ ns.

A detailed study of the different components contributing to the time spectrum has not been performed yet, thus only a qualitative comparison between the results of the BO 1–4 mosaic and the MI detector is possible. However, in the case of the H_2–Ar target, the τ_1 and τ_2 characteristic times are smaller than the ones obtained with the pure-H_2 target for both the $LaBr_3$ detectors modules, and this difference may be ascribed to the presence of μAr atoms, which have

---

[1] The tabulated value of the lifetime of muonic argon may be actually overestimated because it does not take into account the effect of the high-pressure environment on the μAr lifetime.

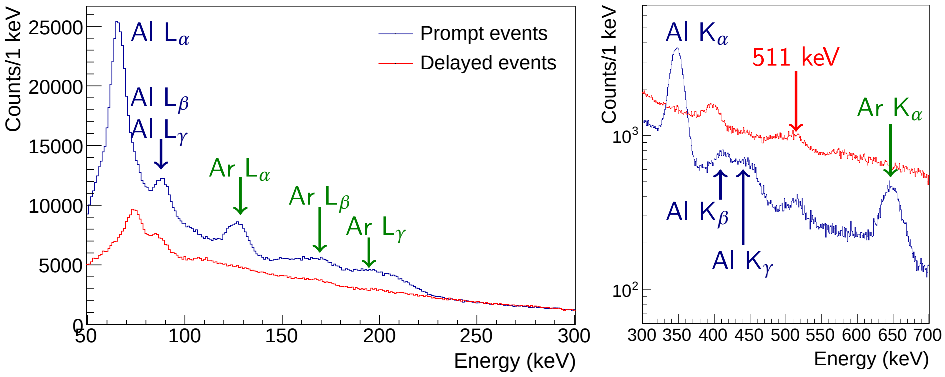

(a) $LaBr_3$ BO 1–4 mosaic

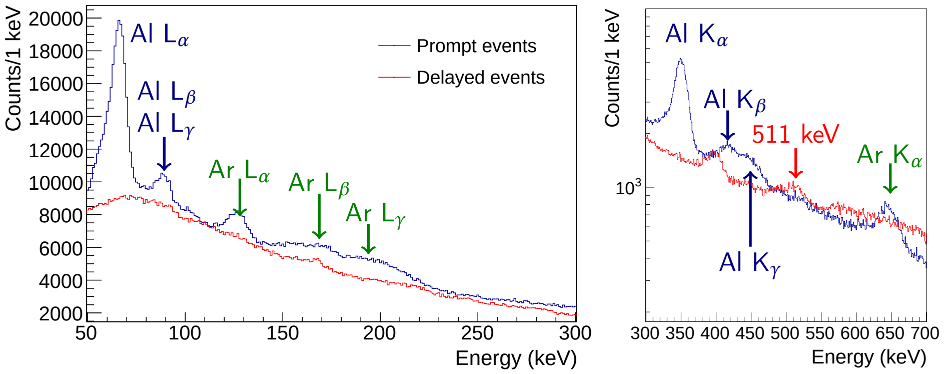

(b) $LaBr_3$ MI

Figure 4.11: Energy spectra of the prompt and delayed events recorded by the $LaBr_3$ scintillating counters for the H_2–Ar target.

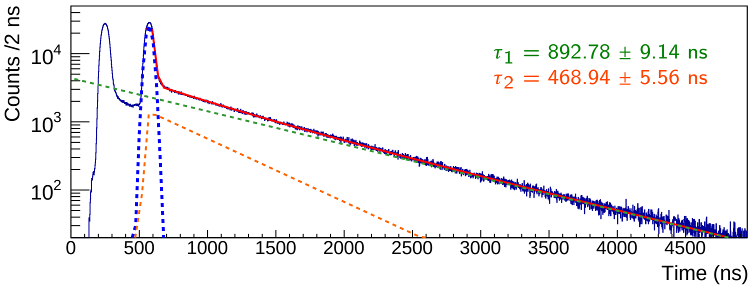

(a) $LaBr_3$ BO 1–4 mosaic

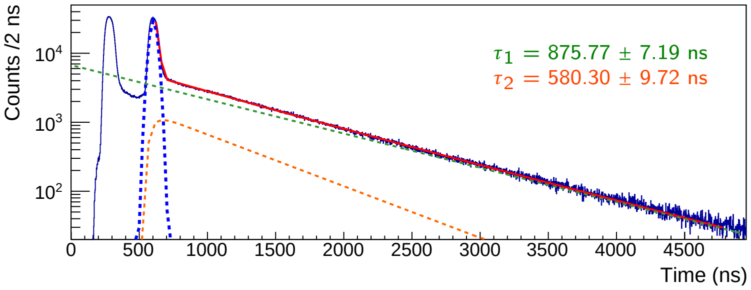

(b) $LaBr_3$ MI

Figure 4.12: Time distribution of the events recorded by the $LaBr_3$ detectors for the H_2–Ar target. The characteristic times τ_1 and τ_2 are referred to the slow- and fast- component of the delayed events distribution respectively.

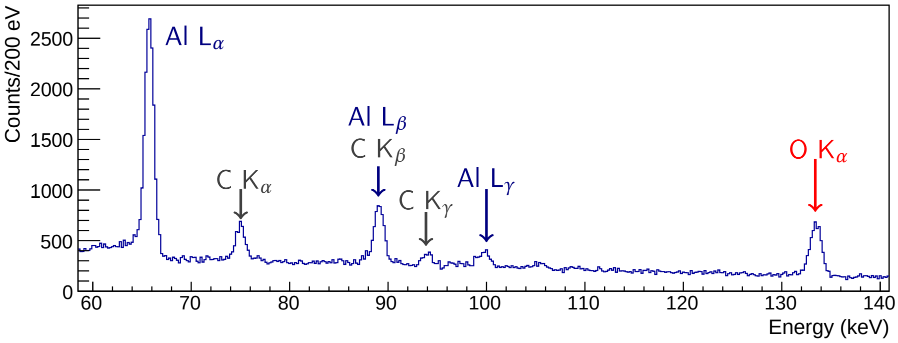

Figure 4.13: Energy spectrum as measured by the GLP HPGe detector for the H_2–CO_2 gas target.

a lifetime much shorter than the one of muonic aluminium, thus reducing the time scale of the exponential decay of the events time distribution.

4.3.4 *Carbon dioxide target*

As mentioned earlier in chapter 2, the most promising candidate for the gas mixture is oxygen. Oxygen is indeed one of the few elements that showed a clear energy dependence of the muon-transfer rate in the epithermal range, and for this reason a discrete number of experimental studies have already been performed in the nineties.

The natural choice for testing the detectors sensitivity to oxygen and the presence of an anomalous muon-transfer rate at epithermal energies would have been to use a H_2–O_2 mixture with the largest possible oxygen concentration. However, such a high concentration of oxygen in a mixture with hydrogen at high pressure is a problem from the safety point of view, given the possibility of explosion. This problem can be solved using carbon dioxide (CO_2) instead of molecular oxygen in the gas mixture; thus the target was filled with a mixture of 96% H_2 and 4% (mass) CO_2 at a pressure of 38 bar, which, in terms of atomic concentration of oxygen, results in $c_O \simeq 3.8‰$.

The choice of this concentration clashes with the optimal concentration depicted in chapter 2 (fig. 2.9), where the value of the oxygen density that would have guaranteed the largest number of muon-transfer events to oxygen was estimated in $c_O \simeq 0.2‰$. This happened because the results of the simulation [63] presented in sec. 2.3.3 were not available at the time of the beam test, and thus the number of delayed oxygen X-rays due to the higher muon-transfer rate from μp to oxygen at epithermal energies is not expected to be particularly relevant.

Once again, the energy spectrum measured by the GLP HPGe detector (fig. 4.13 was used to guarantee that there were no contamination in the gas target and the observation of the lines corresponding to the μAl, μC and μO transitions confirms the composition of the gas mixture.

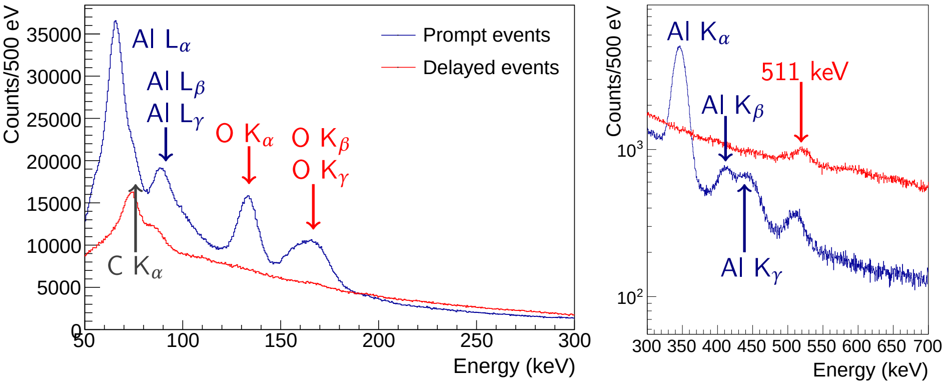

(a) LaBr$_3$ BO 1–4 mosaic

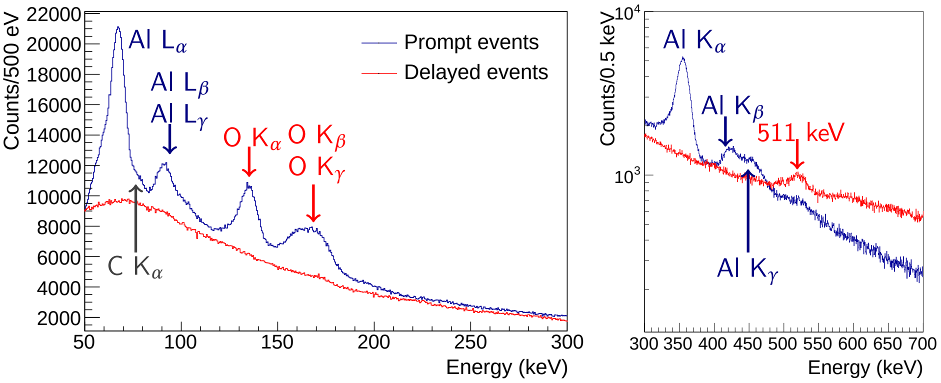

(b) LaBr$_3$ MI

Figure 4.14: Energy spectrum measured by the LaBr$_3$ detectors with the H_2–CO_2 gas target. The oxygen K_α, K_β and K_γ lines are clearly visible.

The energy spectrum as recorded by the LaBr$_3$ detectors is shown in fig. 4.14. The presence of oxygen is evident from the appearance of the K_α, K_β and K_γ transition lines of μO. In the high energy region of the spectrum, only the peaks due to μAl and the line at 511 keV are present, while the mysterious peak at ≈ 400 keV observed in the delayed events obtained with the H_2–Ar gas target (sec. 4.3.3) vanishes, leaving this puzzle confined to the argon mixture only.

The time distribution of the events recorded by the LaBr$_3$ scintillating detectors can be approximated with a double-exponential decay also in this case (fig. 4.15). The characteristic times obtained from the fit are $\tau_1 = 1369.43 \pm 7.59$ ns and $\tau_2 = 609.81 \pm 3.02$ ns for the LaBr BO mosaic, while for the MI detector the values are $\tau_1 = 1271.51 \pm 6.91$ ns and $\tau_2 = 681.52 \pm 5.83$ ns. The difficulties in treating these distributions without a solid theoretical background are the same encountered in the case of the argon target, but still some qualitative considerations are feasible. In this situation the contributions to the time spectrum come from the decay of the free muons and of the various muonic

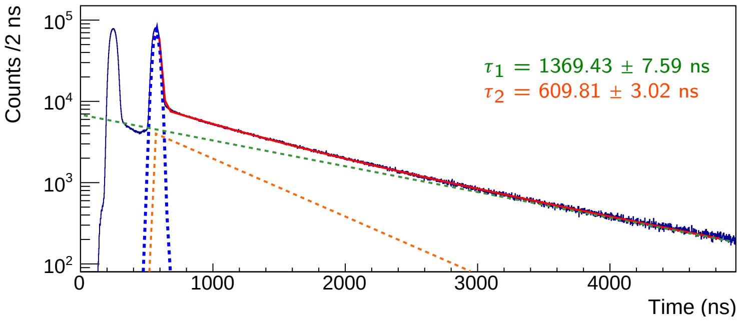

(a) $LaBr_3$ BO 1–4 mosaic

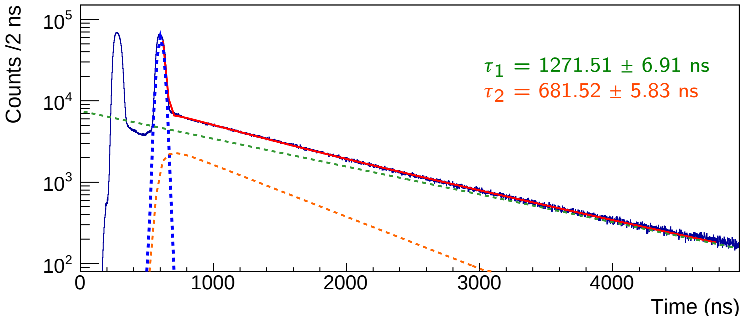

(b) $LaBr_3$ MI

Figure 4.15: Time spectrum of the events obtained with the H_2–CO_2 gas target and recorded by the four $LaBr_3$ BO 1–4 detectors and by the $\varnothing 1'' \times 1''$ $LaBr_3$ scintillator. The τ_1 and τ_2 characteristic times are referred to the slow (far delayed) component and to the faster component respectively.

atoms generated in the target (μAl, μO, μC, μp) and, last but not least, from the various atomic transitions of the muonic atoms.

Assuming that the main difference in the events time distribution for the pure hydrogen and the H_2–Ar/CO_2 mixtures is due to the different decay rate of the muonic atoms formed with the elements present in the target, one can compare the values of τ_1 obtained for the different mixtures and find that (at least) their hierarchy is consistent. A comparison of the τ_2 parameter is much more delicate, given the strong dependence on τ_1. Indeed, the lifetime of the μO atoms is $\approx 1800\,\text{ns}$ [113], thus one can expect the τ_1 time scale to be slightly smaller than the one obtained from the pure hydrogen target (sec. 4.3.2). On the contrary, given the much shorter lifetime of muonic argon ($\approx 537\,\text{ns}$), the value of τ_1 for the H_2–CO_2 target is expected to be larger than the one of the H_2–Ar mixture (sec. 4.3.3). As one can see from the values of τ_1 obtained from the different gaseous targets summarized in tab. 4.2, these predictions are verified.

Despite the fact that the oxygen concentration was not the ideal one, one can always look for an anomalous distribution of the muonic oxygen characteristic X-rays due to the spin-flip of some residual $\mu p(1S)^{F=1}$ atoms that can profit from the higher muon-transfer rate to oxygen at epithermal energies. This can

Detector	τ_1 (ns) for target		
	H_2	$H_2+(4\%)CO_2$	$H_2+(2\%)Ar$
BO 1–4 mosaic	1401.28 ± 19.49	1369.43 ± 7.59	892.78 ± 9.14
MI	1328.02 ± 15.59	1271.51 ± 6.91	875.77 ± 7.19

Table 4.2: τ_1 characteristic times describing the far delayed events distribution for the three different gaseous targets.

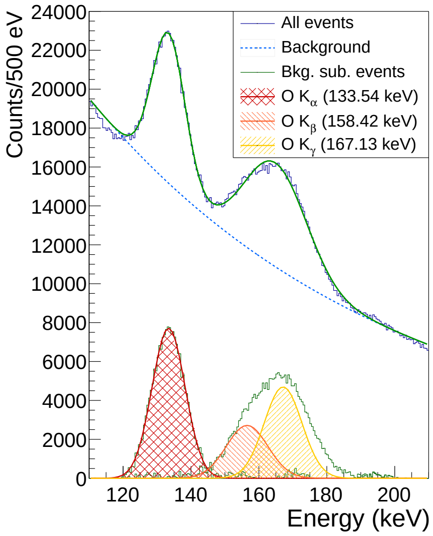

Figure 4.16: Muonic oxygen transition lines measured with the $LaBr_3$ BO mosaic detectors. The relative intensity of the μO K lines is roughly in agreement with the values measured in [76].

be done considering the time distribution of the events under the K_α peak of oxygen. This peak corresponds to an energy of 133.53 keV and does not overlap with any other characteristic X-ray but background. The excellent energy resolution of the $LaBr_3$ detectors (8.59% for the BO mosaic and 8.44% for the MI detector at 133 keV) allows to separate this peak from the K_β and K_γ lines of muonic oxygen (fig. 4.16).

The events under the oxygen 133 keV peak have been selected and fitted following the procedure already used in the previous analysis of the time spectra, and the result has been compared to the ones obtained selecting other portions of the energy spectrum, namely a *test* window between 200 and 290 keV where no particular structure was supposed to play any role, and the 511 keV peak (fig. 4.17).

While the time distribution of the events in the 511 keV region has a single-exponential shape with $\tau_{511} = 1091.50 \pm 38.11$ ns, the temporal distributions of

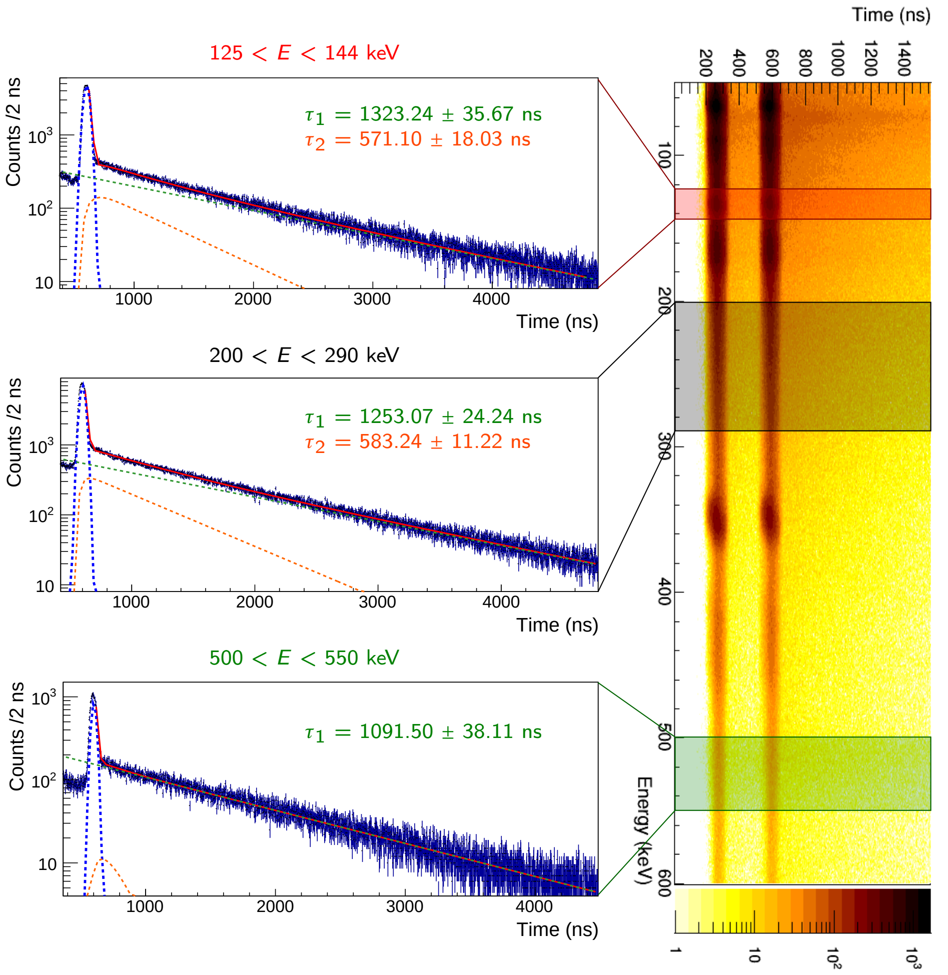

Figure 4.17: Temporal distribution of the events corresponding to different regions of the energy spectrum obtained with the $LaBr_3$ MI detector.

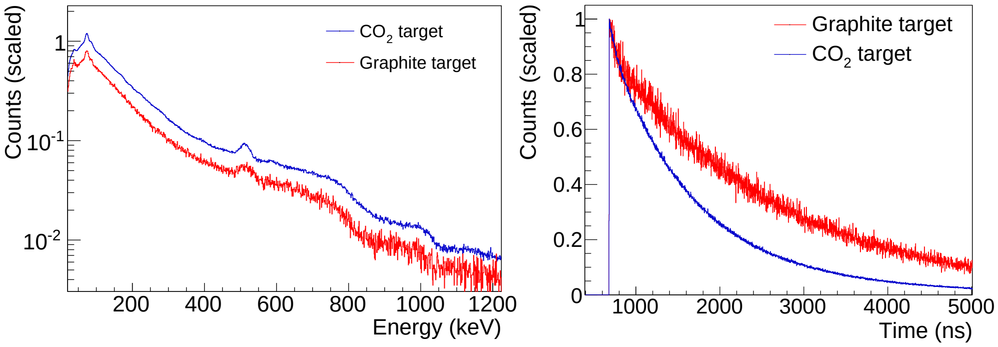

(a) Energy spectrum ($t > 680$ ns) **(b)** Time spectrum ($t > 680$ ns)

Figure 4.18: Energy and time spectrum of the events recorded after $t = 680$ ns with the H_2–CO_2 mixture (blue) and the graphite (red) target. The energy spectra **(a)** have been rescaled differently for the two targets in order to allow a better comparison.

the events under the K_α μO peak and in the test energy window are essentially identical and no evidence of an abundance of delayed oxygen X-rays is found.

This is probably due to the high concentration of atomic oxygen which reduces the population of μp atoms in the triplet state in a time too small to let them play a significant role in the time region outside the two pulses corresponding to the beam spills.

4.4 FINAL REMARKS

In conclusion, the $LaBr_3$ detectors completely met the requirements of the experiment for what concerns their performance in terms of energy resolution, while the events time spectra are not well understood yet and require some additional simulations and theoretical work.

Another unclear aspect in the data acquired during the June 2014 test beam is the background which afflicts the $LaBr_3$ detectors. The intrinsic radioactivity of lanthanum is too small to play a significant role, while the presence of activated materials in the experimental area has been ruled out analysing the data of some runs acquired when the muon beam was down. As explained earlier, the main suspects for the origin of this background are electrons generated in muons decays interacting with matter around the crystals or with the crystals themselves.

This hypothesis can also explain the fact that the energy spectrum of the events occurring after 680 ns from the trigger for the graphite and the H_2–CO_2 target is essentially the same for the two cases, though it shows a substantially different time distribution (fig. 4.18). As already discussed, to verify this possibility a Monte Carlo simulation of the target and the detection system is needed.

CHAPTER 5

CONCLUSIONS AND OUTLOOKS

The proton radius puzzle is one of the many intriguing problems in modern physics. Four years after the publication of the results of the Lamb shift experiment at PSI that provided a measurement of the RMS proton charge radius inconsistent with the ones obtained in previous experiments, a solution of the problem is still far.

In this framework, many hypotheses are still on the table: from unconsidered methodology uncertainties in the measurements to effects of new physics beyond the Standard Model. The FAMU experiment aims at shading new light on the electromagnetic structure of the proton by measuring the hyperfine splitting (HFS) of the ground state of muonic hydrogen. The value of this transition is indeed sensitive to the proton Zemach radius, that is the first moment of the convolution of the proton charge and magnetic moment density. A comparison with the values extracted from previous experiments performed with electrons, may delimit or strengthen the proton radius puzzle.

In this experiment the techniques of particle physics and atomic spectroscopy are combined to obtain the first direct measurement of the ground state HFS of muonic hydrogen. The experimental strategy relies on the transfer of a negative muon from muonic hydrogen to some specific higher-Z gas. Singlet-state muonic hydrogen atoms in thermal equilibrium are excited in the triplet state by a ~6.8 µm wavelength laser pulse; these atoms are de-excited back to the singlet configuration in collision with H_2 molecules and the transition energy ($\approx$ 180 meV) is converted into kinetic energy of the H_2–μp system; thus the muonic hydrogen atom results accelerated of about 120 meV (~ 2/3 of the available energy). These "kicked" atoms can be recognized since the transfer of their muon to some other element (*e.g.* oxygen) occurs at higher rate with respect to thermalized muonic hydrogen; indeed, the muonic atom formed after the muon passage is in an excited state and promptly de-excites to its ground state emitting a characteristic X-ray that can be detected. Hence, counting the number of characteristic X-rays emitted after the laser pulse for different laser frequencies one can obtain a resonance-like plot from which the hyperfine transition energy can be extracted.

In this thesis the results of a preliminary detection system tested in June 2014 at the Rutherford-Appleton Laboratories are described. A hodoscope was built for the beam monitoring and a HPGe detector specifically suited for low-energy X-rays was used to obtain a benchmark of the X-ray spectrum, while the heart of the X-spectrometric system consisted in scintillating detectors based on $LaBr_3$(Ce) crystals. In order to obtain the largest achievable amount of information from the data of the $LaBr_3$ scintillating detectors, the full waveform was recorded by a 500 MHz digitizer for a time of 5 µs after the trigger provided by the muon beam. This required the development of an algorithm for the offline analysis of the waveforms; this program is able to automatically identify the pulses in the signal and to extract all the desired information (pulse height, integral, starting time, etc.) with a fit of every single pulse with a Landau function. In this way, pile-up events (typically ~ 26% of the data set) are recovered for the analysis.

During the beam test a graphite block and three different gaseous targets were exposed to a muon beam. In all the cases, the detection system was capable of identifying all the expected muonic atoms transitions, despite the presence of a quite relevant diffused background whose origin is still unclear. The obtained events time distributions roughly agree with reasonable expectations, but require some additional theoretical work and dedicated Monte Carlo simulations to be really understood. The explanation of the background is of great importance for a correct interpretation of the data, and a Monte Carlo simulation of the detector system may have a primary role in performing this task. Even if the background spectrum is quite “smooth” in the region of the muonic oxygen characteristic peaks and this could allow to recognise quite easily a peak of events occurring after the laser pulse, a reduction of the background would be welcome.

A new beam test will be performed at RAL in the summer 2015 treasuring the experience of 2014. In particular, some changes are foreseen in the experimental set-up:

GAS TARGET A cryogenic gas target is being currently developed for the 2015 beam test. While a lower temperature would allow a faster thermalization of the muonic hydrogen atoms, the impact of the larger material budget on the detection of ~ 100 keV X-rays might be a problem. This effect will be studied with dedicated Monte Carlo simulations.

The result of the simulation which has determined the optimal oxygen concentration (sec. 2.3.3) has given a value much smaller than what expected. This opens the door for the H_2–O_2 gas mixture, since with this level of oxygen concentration the target might fulfill the safety requirements also at high pressure.

HODOSCOPE The readout electronics of the hodoscope used in the 2014 beam test was not fit for the high intensity muon beam of the RIKEN-RAL facility and the output signals were saturated. A new hodoscope is currently under construction using ∅1 mm scintillating fibers. Also the electronics will be replaced in order to achieve a larger dynamic range that would allow to manage signals corresponding to about 70 muons/spill for each fiber.

SCINTILLATING CRYSTALS For the 2015 beam test four new ∅1.5″ × 1.5″ Brillance $LaBr_3$(Ce) crystals, in addition to the ones already used in the 2014 beam test, will be present. To avoid the non-linearity observed at high energies (sec. 3.2.3), a specific PMT voltage divider has been developed.

As mentioned earlier in chapter 4, the main suspects for the background observed by the $LaBr_3$ counters are electrons from muon decays; the energy deposit of such electrons in the scintillating crystals may be identified by means of an anti-coincidence veto able to discriminate the passage of photons from charged particles. The most natural choice is the use of plastic scintillator tiles or fibers rolled around the crystals themselves.

The FAMU experiment combines many different aspects of physics, and for all of them there is work to do: together with the detectors, also the laser system is currently being developed [114], while the theoretical work on atomic dynamics and on the muon transfer process is still going on. The conjoint efforts of different parts of the physics community are indeed needed to shed some light on such a fascinating problem.

LIST OF ACRONYMS

ADC	Analog to Digital Converter
CODATA	Committee on Data for Science and Technology
DAQ	Data AcQuisition
DOF	Degrees Of Freedom
EC	Electronic Capture
ep	Ordinary hydrogen
FAMU	Fisica Atomi MUonici (*Muonic Atoms Physics*)
FIR	Far InfraRed
FT	Fourier Transform
FWHM	Full Width at Half Maximum
HFS	HyperFine Splitting
HPGe	High Purity Germanium
INFN	Istituto Nazionale di Fisica Nucleare (*Italian National Institute for Nuclear Physics*)
JLab	Jefferson Laboratories
MAMI	MAiz MIcrotron
MIP	Minimum Ionizing Particle
μCF	Muon Catalized Fusion
μp	Muonic hydrogen
μSR	Muon Spin Relaxation, Rotation and Resonance
μTE	Muon Transfer Event
PH	Pulse Height
PI	Pulse Integral
PMT	PhotoMultiplier Tube
PSI	Paul Scherrer Institute

QCD	Quantum ChromoDynamics
QDC	Charge to Digital Converter
QED	Quantum ElectroDynamics
RAL	Rutherford Appleton Laboratory
RF	Radio Frequency
RMS	Root Mean Square
SiPM	Silicon Photo-Multiplier
SLAC	Stanford Linear Accelerator Complex
SM	Standard Model (of Particle Physics)
STFC	Science and Technology Facilities Council
TPE	Two-Photons Exchange
VME	Versa Module Eurocard

LIST OF FIGURES

Figure 1.1 Feynman diagrams representing the elastic scattering of an electron off a heavier point-like particle and a proton. 9
Figure 1.2 Scheme of the arrangement of the three spectrometers used at MAMI by the A1 collaboration. 13
Figure 1.3 Rendering of the detector system and of one of the magnetic spectrometers used by the A1 collaboration. 14
Figure 1.4 The electric form factor $G_E(Q^2)$ normalized to the standard dipole as a function of Q^2, as obtained by the A1 collaboration. 16
Figure 1.5 Feynman diagrams of the leading order contributions to the electron self-energy and to the vacuum polarization. 19
Figure 1.6 Scheme of the experimental set-up used by Parthey et al. for the measurement of the $1S$–$2S$ transition energy. 20
Figure 1.7 Photon count rate as a function of the frequency detuning for different values of the delay τ. 21
Figure 1.8 Values of the proton charge radius r_p obtained from hydrogen spectroscopy. 22
Figure 1.9 Recent "history" of the proton charge radius. 23
Figure 1.10 Comparison of the $n = 2$ energy levels in ordinary hydrogen and in muonic hydrogen. 24
Figure 1.11 Integrated X-ray spectrum recorded on- and off- resonance in the Lamb shift experiment. 26
Figure 1.12 Resonance plot of the $2S \to 2P$ transition in muonic hydrogen obtained in the Lamb shift experiment. 27
Figure 2.1 Recent values of the Zemach radius of the proton obtained using data from ordinary hydrogen and muonic hydrogen. 36
Figure 2.2 Scheme of the FAMU experimental method. 37
Figure 2.3 Time evolution of the average μp$(1S)$ for different target pressures at a constant temperature and at different temperatures for a fixed hydrogen density. 40
Figure 2.4 Time evolution of the population of the triplet state of muonic hydrogen at a room temperature $T = 300\,\mathrm{K}$ for different values of pressure. 41
Figure 2.5 Measured time distribution of $2P \to 1S$ X-rays of sulphur and oxygen. 44
Figure 2.6 Schematic representation of the two-component model for the muon transfer to oxygen. 45

Figure 2.7 Transfer rate λ_{pO} as a function of the μp atom kinetic energy used by Wertmüller et al. 45
Figure 2.8 Number of survived μp$(1S)$ atoms in a H_2–O_2 gas mixture at 300 K, 35 atm for various oxygen concentrations. . 46
Figure 2.9 Number of muon-transfer events from thermalized μp$(1S)$ atoms to oxygen for $T = 300\,\mathrm{K}$ and $P = 35\,\mathrm{atm}$ as a function of the oxygen concentration. 47
Figure 3.1 Sketch of the ISIS accelerator complex. 50
Figure 3.2 Layout of the RIKEN-RAL muon facility. 51
Figure 3.3 Time structure of the pulsed muon beam of the RIKEN-RAL muon facility. 52
Figure 3.4 Calculated muon intensity as a function of the muon momentum on an area of $4 \times 4\,\mathrm{cm}^2$. 53
Figure 3.5 PhotoDetection Efficiency of the ASD-RGB3S-P SiPM and light output spectrum of the BCF-12 scintillating fiber. . . 54
Figure 3.6 Picture of the “mosaic” detection module. 57
Figure 3.7 Intrinsic total efficiency of LaBr_3 scintillators of different thickness. 58
Figure 3.8 Scheme of the DAQ system used at the beam test. 60
Figure 3.9 FAMU control board timing sketch. 60
Figure 3.10 Two examples of the digitizer output of the LaBr_3 detector. 62
Figure 3.11 Signal output (and spikes) from the four (BO 1–4) LaBr_3 detectors. 63
Figure 3.12 Example of single- and multi-pulse events in the digitized output of the LaBr_3 scintillating detector. 64
Figure 3.13 Example of single- and multi-pulse events processed by the `ScanPeak` method. 64
Figure 3.14 Example of the pulse integration domain and correlation between the pulse height and its integral for γ rays from ^{226}Ra. 65
Figure 3.15 A fraction of the ^{226}Ra spectrum obtained with the distribution of the pulse integral and of the pulse height. . . 65
Figure 3.16 Energy resolution and deviation from the calibration value for the BO 1 detector. 68
Figure 4.1 Picture of the experimental set-up installed at the experimental port-4 at the RIKEN-RAL muon facility. 70
Figure 4.2 Fraction of muons stopped in the entrance window, in the target and in the rear wall as a function of the muon beam momentum obtained with a Monte Carlo simulation. 71
Figure 4.3 The three lines at 75.26, 89.21 and 94.1 keV of muonic carbon in the energy spectrum of the HPGe detector. . . . 72
Figure 4.4 X-ray spectrum of the graphite target measured with the LaBr_3 scintillating detectors and obtained from the PH and the PI distributions. 73

Figure 4.5 Time spectrum of the events recorded by the $LaBr_3$ scintillating detectors for the graphite target. 74

Figure 4.6 X-ray spectrum of the graphite target. 75

Figure 4.7 Energy spectrum recorded by the HPGe detector for the pure H_2 target. 76

Figure 4.8 X-ray spectrum obtained with the $LaBr_3$ scintillating detectors for the H_2 target. 77

Figure 4.9 Time spectrum of the recorded events for the H_2 target. . 78

Figure 4.10 Energy spectrum obtained with the GLP HPGe detector for the H_2–Ar target. 79

Figure 4.11 Energy spectra of the prompt and delayed events recorded by the $LaBr_3$ scintillating counters for the H_2–Ar target. 80

Figure 4.12 Time distribution of the events recorded by the $LaBr_3$ detectors for the H_2–Ar target. 81

Figure 4.13 Energy spectrum as measured by the GLP HPGe detector for the H_2–CO_2 gas target. 82

Figure 4.14 Energy spectrum measured by the $LaBr_3$ detectors with the H_2–CO_2 gas target. 83

Figure 4.15 Time spectrum of the events obtained with the H_2–CO_2 gas target and recorded by the $LaBr_3$ detectors. 84

Figure 4.16 Muonic oxygen transition lines measured with the $LaBr_3$ BO mosaic detectors. 85

Figure 4.17 Temporal distribution of the events corresponding to different regions of the energy spectrum obtained with the $LaBr_3$ MI detector. 86

Figure 4.18 Energy and time spectrum of the events recorded after $t = 680\,\mathrm{ns}$ with the H_2–CO_2 mixture and the graphite target. 87

LIST OF TABLES

Table 2.1 Numerical values for the various corrections to the hyperfine splitting in hydrogen obtained by Volotka et al. . 34
Table 2.2 Recent values of the Zemach radius of the proton R_p. . . 35
Table 3.1 Properties of selected inorganic scintillators. 56
Table 3.2 Performance of BO 1 and BO 2 $\mathrm{LaBr_3}$ scintillating detectors. 66
Table 3.3 Performance of BO 3 and BO 4 $\mathrm{LaBr_3}$ scintillating detectors. 67
Table 3.4 Performance of the $\varnothing 1'' \times 1''$ $\mathrm{LaBr_3}$ scintillating detector. 67
Table 4.1 Relevant transition energies for the muonic atoms formed by the selected elements. 72
Table 4.2 τ_1 characteristic times describing the far delayed events distribution for the three different gaseous targets. 85

BIBLIOGRAPHY

[1] H. Geiger and E. Marsden. “On a diffuse reflection of the α-particles”. In: *Proceedings of the Royal Society A* 82 (1909).

[2] E. Rutherford. “The scattering of α and β particles by matter and the structure of the atom”. In: *Philosopical Magazine* 21 (1911).

[3] E. Rutherford. “Collision of α particles with light atoms. IV. An anomalous effect in nitrogen”. In: *Philosophical Magazine* 90 (1919).

[4] J. J. Thomson. “Cathode rays”. In: *Philosopical Magazine* 44 (1897).

[5] J. Chadwick. “Possible Existence of a Neutron”. In: *Nature* 192 (1932).

[6] P. J. Mohr, B. N. Taylor, and D. B. Newell. “CODATA recommended values of the fundamental physical constants: 2010*”. In: *Review of Modern Physics* 84 (2012).

[7] I. Estermann, R. Frisch, and O. Stern. “Magnetic Moment of the Proton”. In: *Nature* 132 (1933).

[8] G. D. Rochester and C. C. Butler. “Evidence for the Existence of New Unstable Elementary Particles”. In: *Nature* 160 (1947).

[9] M. Gell-Mann. “Symmetries of Baryons and Mesons”. In: *Physical Review* 125 (1962).

[10] M. Gell-Mann and Y. Ne’eman, eds. *The eightfold way*. W. A. Benjamin, 1964.

[11] D. J. Griffiths. *Introduction to Elementary Particles*. Wiley-VCH, 2008.

[12] R. W. McAllister and R. Hofstadter. “Elastic Scattering of 188-MeV Electrons from the Proton and the Alpha Particle”. In: *Physical Review* 102 (1956).

[13] R. P. Feynman. “Very High-Energy Collisions of Hadrons”. In: *Physical Review Letters* 23 (1969).

[14] E. D. Bloom et al. “High-Energy Inelastic e–p Scattering at 6° and 10°”. In: *Physical Review Letters* 23 (1969).

[15] S. Dürr et al. “Ab Initio Determination of Light Hadron Masses”. In: *Science* 322 (2008).

[16] R. Pohl et al. “The size of the proton”. In: *Nature* 466 (2010).

[17] P. G. Ratcliffe. *An Introduction to Elementary Particle Phenomenology*. IOP Publishing, 2014.

[18] N. F. Mott. “The Scattering of Fast Electrons by Atomic Nuclei”. In: *Proceedings of the Royal Society A* 124 (1929).

[19] F. Halzen and A. D. Martin. *Quarks and Leptons: an Introductory Course in Modern Particle Physics*. John Wiley and Sons, 1984.

[20] A. W. Thomas and W. Weise. *The Structure of the Nucleon*. Wiley-VCH, 2001.

[21] J. C. Bernauer et al. "High-Precision Determination of the Electric and Magnetic Form Factors of the Proton". In: *Physical Review Letters* 105 (2010).

[22] J. C. Bernauer. "Measurement of the elastic electron-proton cross section and separation of the electric and magnetic form factor in the Q^2 range from 0.004 to 1 (GeV/c)^2". PhD thesis. Johannes Gutenberg-Universität Mainz, 2010. URL: `http://wwwa1.kph.uni-mainz.de/A1/publications/doctor/bernauer.pdf`.

[23] K. I. Blomqvist et al. "The three-spectrometer facility at the Mainz Microtron MAMI". In: *Nuclear Instruments and Methods in Physics Research A* 403 (1998).

[24] M. N. Rosenbluth. "High Energy Elastic Scattering of Electrons on Protons". In: *Physical Review* 79 (1950).

[25] R. Pohl et al. "Muonic Hydrogen and the Proton Radius Puzzle". In: *Annual Review of Nuclear and Particle Science* 63 (2013).

[26] J. Arrington. "Comment on "High-Precision Determination of the Electric and Magnetic Form Factors of the Proton"". In: *Physical Review Letters* 107 (2011).

[27] J. C. Bernauer et al. "Bernauer *et al.* Reply:" in: *Physical Review Letters* 107 (2011).

[28] W. E. Lamb and R. C. Retherford. "Fine Structure of the Hydrogen Atom by a Microwave Method". In: *Physical Review* 72 (1947).

[29] C. G. Parthey et al. "Improved Measurement of the Hydrogen $1S$–$2S$ Transition Frequency". In: *Physical Review Letters* 107 (2011).

[30] A. Antognini. "The Lamb Shift Experiment in Muonic Hydrogen". PhD thesis. Ludwig-Maximilians-Universität München, 2005. URL: `http://nbn-resolving.de/urn:nbn:de:bvb:19-50441`.

[31] M. I. Eides, H. Grotch, and V. A. Shelyuto. "Theory of light hydrogenlike atoms". In: *Physics Reports* 342 (2001).

[32] J. Schwinger. "On Quantum-Electrodynamics and the Magnetic Moment of the Electron". In: *Physical Review* 73 (1948).

[33] B. de Beauvoir et al. "Absolute Frequency Measurement of the $2S$–$8S/D$ Transitions in Hydrogen and Deuterium: New Determination of the Rydberg Constant". In: *Physical Review Letters* 78 (1997).

[34] C. Schwob et al. "Optical Frequency Measurement of the $2S$–$12D$ Transitions in Hydrogen and Deuterium: Rydberg Constant and Lamb Shift Determinations". In: *Physical Review Letters* 82 (1999).

[35] X. Zhan et al. "High-precision measurement of the proton elastic form factor ratio at low Q^2". In: *Physics Letters B* 705 (2011).

[36] R. Rosenfelder. "Coulomb corrections to elastic electron–proton scattering and the proton charge radius". In: *Physics Letters B* 479 (2000).

[37] I. Sick. "On the rms-radius of the proton". In: *Physics Letters B* 576 (2003).

[38] I. Sick. "Troubles with the Proton rms-Radius". In: *Few-Body Systems* 50 (2011).

[39] I. Sick. "Problems with proton radii". In: *Progress in Particle and Nuclear Physics* 67 (2012). From Quarks and Gluons to Hadrons and Nuclei International Workshop on Nuclear Physics, 33rd Course.

[40] P. J. Mohr, B. N. Taylor, and D. B. Newell. "CODATA recommended values of the fundamental physical constants: 2006*". In: *Review of Modern Physics* 80 (2008).

[41] L. Ludhova. "The muonic hydrogen lamb shift experiment: lifetime and population of the μp($2S$) state". PhD thesis. Université de Fribourg, 2005. URL: `http://doc.rero.ch/record/5540`.

[42] L. Ludhova et al. "Planar LAAPDs: temperature dependence, performance, and application in low-energy X-ray spectroscopy". In: *Nuclear Instruments and Methods in Physics Research A* 540 (2005).

[43] A. Antognini et al. "Proton Structure from the Measurement of 2S-2P Transition Frequencies of Muonic Hydrogen". In: *Science* 339 (2013).

[44] A. Gasparian et al. *High Precision Measurement of the Proton Charge Radius. An Update to Proposal C12-11-106 for Jefferson Lab PAC-39*. 2012. URL: `https://www.jlab.org/exp_prog/proposals/12/C12-11-106.pdf`.

[45] A. Hoecker and W. J. Marciano. "The muon anomalous magnetic moment". In: *2014 Review of Particle Physics*. Ed. by K. A. Olive at al. *Chinese Physics C* 38, 2014.

[46] D. Tucker-Smith and I. Yavin. "Muonic hydrogen and MeV forces". In: *Physical Review D* 83 (2011).

[47] B. Batell, D. McKeen, and M. Pospelov. "New Parity-Violating Muonic Forces and the Proton Charge Radius". In: *Physical Review Letters* 107 (2011).

[48] R. Onofrio. "Proton radius puzzle and quantum gravity at the Fermi scale". In: *Europhysics Letters* 104 (2013).

[49] J. Arrington et al. *Studying the Proton "Radius" Puzzle with μp Elastic Scattering. A Proposal for the Paul Scherrer Institute πM1 beam line*. 2012. URL: `http://www.physics.rutgers.edu/~rgilman/elasticmup/mup_prop_finals.pdf`.

[50] D. J. Griffiths. *Introduction to Quantum Mechanics*. Pearson Prentice Hall, 2005.

[51] E. Fermi. “Über die magnetischen Momente der Atomkerne”. In: *Zeitschrift für Physik* 60 (1930).

[52] G. Breit. “Possible Effects of Nuclear Spin on X-Ray Terms”. In: *Physical Review* 35 (1930).

[53] C. M. Sommerfield. “Magnetic Dipole Moment of the Electron”. In: *Physical Review* 107 (1957).

[54] A. Petermann. “Magnetic moment of the electron”. In: *Nuclear Physics* 3.5 (1957).

[55] A. Dupays et al. “Proton Zemach radius from measurements of the hyperfine splitting of hydrogen and muonic hydrogen”. In: *Physical Review A* 68 (2003).

[56] A. V. Volotka et al. “Zemach and magnetic radius of the proton from the hyperfine splitting in hydrogen”. In: *The European Physical Journal D* 33 (2005).

[57] M. I. Eides. “Weak-interaction contributions to hyperfine splitting and Lamb shift in light muonic atoms”. In: *Physical Review A* 85 (2012).

[58] A. C. Zemach. “Proton Structure and the Hyperfine Shift in Hydrogen”. In: *Physical Review* 104 (1956).

[59] A.P. Martynenko and R.N. Faustov. “Hyperfine ground-state structure of muonic hydrogen”. In: *Journal of Experimental and Theoretical Physics* 98 (2004).

[60] S. G. Karshenboim. “Nuclear structure-dependent radiative corrections to the hydrogen hyperfine splitting”. In: *Physics Letters A* 225 (1997).

[61] J. L. Friar and I. Sick. “Zemach moments for hydrogen and deuterium”. In: *Physics Letters B* 579 (2004).

[62] M. O. Distler, J. C. Bernauer, and T. Walcher. “The RMS charge radius of the proton and Zemach moments”. In: *Physics Letters B* 696 (2011).

[63] D. Bakalov et al. “Theoretical and computational study of the energy dependence of the muon transfer rate from hydrogen to higher-Z gases”. In: *Physics Letters A* 379 (2015).

[64] A. Adamczak et al. “Hyperfine spectroscopy of muonic hydrogen and the PSI Lamb shift experiment”. In: *Nuclear Instruments and Methods in Physics Research B* 281 (2012).

[65] D. S. Covita et al. “Line Shape of the μH($3p-1s$) Hyperfine Transitions”. In: *Physical Review Letters* 102 (2009).

[66] D. Bakalov et al. “Experimental method to measure the hyperfine splitting of muomic hydrogen (μ-p)1S”. In: *Physics Letters A* 172 (1993).

[67] A. Adamczak et al. “On the Use of a H_2–O_2 Gas Target in Muonic Hydrogen Atom Hyperfine Splitting Experiments”. In: *Hyperfine Interactions* 136-137 (2001).

[68] A. Werthmüller et al. “Transfer of negative muons from hydrogen to oxygen”. In: *Hyperfine Interactions* 103 (1996).

[69] F. Mulhauser and H. Schneuwly. “Systematic study of muon transfer to sulphur dioxide”. In: *Hyperfine Interactions* 82 (1993).

[70] R. Jacot-Guillarmod et al. “Charge transfer from muonic hydrogen to neon”. In: *Physical Review Letters* 65 (1990).

[71] R. Jacot-Guillarmod et al. “Muon transfer from thermalized muonic hydrogen isotopes to argon”. In: *Physical Review A* 55 (1997).

[72] D. F. Measday. “The nuclear physics of muon capture”. In: *Physics Reports* 354 (2001).

[73] A. Adamczak et al. “Atlas of cross sections for scattering of muonic hydrogen atoms on hydrogen isotoped molecules”. In: *Atomic Data and Nuclear Data Tables* 62 (1996).

[74] A. Adamczak. “Differential cross sections for muonic atom scattering from hydrogenic molecules”. In: *Physical Review A* 74 (2006).

[75] W. H. Breunlich et al. “Muon-Catalyzed Fusion”. In: *Annual Review of Nuclear and Particle Science* 39 (1989).

[76] A. Werthmüller et al. “Energy dependence of the charge exchange reaction from muonic hydrogen to oxygen”. In: *Hyperfine Interactions* 116 (1998).

[77] A. Dupays et al. “Hyperspherical elliptic coordinate treatment of muon transfer from muonic hydrogen to atomic oxygen”. In: *Physical Review A* 68 (2003).

[78] A. Dupays et al. “Calculation of muon transfer from muonic hydrogen to atomic oxygen”. In: *Physical Review A* 67 (2003).

[79] A. Dupays et al. “Nonzero total-angular-momentum three-body dynamics using hyperspherical elliptic coordinates: Application to muon transfer from muonic hydrogen to atomic oxygen and neon”. In: *Physical Review A* 69 (2004).

[80] A.-T. Le and C. D. Lin. “Muon transfer from muonic hydrogen to atomic oxygen and nitrogen”. In: *Physical Review A* 71 (2005).

[81] T. Matsuzaki et al. “The RIKEN-RAL pulsed Muon Facility”. In: *Nuclear Instruments and Methods in Physics Research A* 465 (2001).

[82] Saint-Gobain Crystals. *Bicron BCF-12 datasheet*. URL: `http://www.crystals.saint-gobain.com/uploadedFiles/SG-Crystals/Documents/SGC%20Fibers%20Brochure.pdf`.

[83] AdvanSiD. *ASD-RGB3S-P datasheet*. URL: `http://advansid.com/attachment/get/up_53_1410956501.pdf`.

[84] B. Dolgoshein et al. “Limited Geiger-mode microcell silicon photodiode: new results”. In: *Nuclear Instruments and Methods in Physics Research A* 442 (2000).

[85] R. Pleskac et al. “The FIRST experiment at GSI”. In: *Nuclear Instruments and Methods in Physics Research A* 678 (2012).

[86] P. Branchini et al. “An FGPA Based General Purpose DAQ Module for the KLOE-2 Experiment”. In: *IEEE Transactions on Nuclear Science* 58 (2011).

[87] P. Valente et al. “Commissioning of the DAΦNE beam test facility”. In: *Nuclear Instruments and Methods in Physics Research A* 515 (2003).

[88] R. Carbone. “The fiber-SiPMT beam monitor of the R484 experiment at RIKEN-RAL Muon Facility”. In: *Proceedings of iWoRID 2014*. Accepted for publication on *Journal of Instrumentation*.

[89] E. V. D. van Loef et al. “High-energy-resolution scintillator: Ce^{3+} activated $LaBr_3$”. In: *Applied Physics Letters* 79 (2001).

[90] E. V. D. van Loef et al. “High-energy-resolution scintillator: Ce^{3+} activated $LaCl_3$”. In: *Applied Physics Letters* 77 (2000).

[91] G. F. Knoll. *Radiation Detection and Measurement*. John Wiley and Sons, 2010.

[92] Saint-Gobain Crystals. *Physical Properties of Common Inorganic Scintillators*. URL: `http://www.crystals.saint-gobain.com/uploadedFiles/SG-Crystals/Documents/Physical%20Properties%20of%20Inorganic%20Scintillators.pdf`.

[93] S. Derenzo et al. *Scintillation Properties*. Lawrence Berkeley National Laboratory. URL: `http://scintillator.lbl.gov/`.

[94] *Brillance^{TM} Scintillators Performance Summary*. Saint-Gobain Crystals. URL: `http://www.crystals.saint-gobain.com/uploadedFiles/SG-Crystals/Documents/Technical/SGC%20BrilLanCe%20Scintillators%20Performance%20Summary.pdf`.

[95] B. D. Milbrath et al. *Contamination in $LaCl_{3:}$Ce Scintillators*. Tech. rep. PNNL-15453. Pacific Northwest National Laboratory, 2005.

[96] Hamamatsu Photonics. *R11265U SERIES / H11934 SERIES*. URL: `http://www.hamamatsu.com/resources/pdf/etd/R11265U_H11934_TPMH1336E.pdf`.

[97] Saint-Gobain Crystals. *Efficiency calculation for selected scintillators*. URL: `http://www.crystals.saint-gobain.com/uploadedFiles/SG-Crystals/Documents/Technical/SGC%20Efficiency%20Calculations%20Brochure.pdf`.

[98] Ortec. *GLP series planar HPGe Low Energy Detector*. URL: `http://www.ortec-online.com/download/glp.pdf`.

[99] Ortec. *GMX series coaxial HPGe Detector*. URL: `http://www.ortec-online.com/download/gamma-x.pdf`.

[100] Ortec. *672 spectroscopy amplifier*. URL: `http://www.ortec-online.com/download/672.pdf`.

[101] CAEN. *V792 - 32 Channel Multievent QDC*. URL: `http://www.caen.it/csite/CaenProd.jsp?idmod=41&parent=11`.

[102] R. Brun and F. Rademakers. “ROOT - An Object Oriented Data Analysis Framework”. In: *Nuclear Instruments and Methods in Physics Research A* 389 (1997).

[103] M. Morhac et al. “Background elimination methods for multidimensional coincidence gamma-ray spectra”. In: *Nuclear Instruments and Methods in Physics Research A* 401 (1997).

[104] M. Morhac et al. “Efficient one- and two-dimensional Gold deconvolution and its application to gamma-ray spectra”. In: *Nuclear Instruments and Methods in Physics Research A* 401 (1997).

[105] M. Morhac et al. “Identification of peaks in multidimensional coincidence gamma-ray spectra”. In: *Nuclear Instruments and Methods in Physics Research A* 443 (2000).

[106] P. Dorenbos, J.T.M. de Haas, and C.W.E. van Eijk. “Gamma ray spectroscopy with a $\varnothing 19\times 19$ mm^3 LaBr3:0.5% Ce$_3^+$ scintillator”. In: *IEEE Transactions on Nuclear Science* 51 (2004).

[107] Yu. A. Trofimov, E. E. Lupar, and V. N. Yurov. “Linearity of the Energy Scale of a Detector Based on LaBr$_3$(Ce) Scintillator”. In: *Instruments and Experimental Techniques* 56 (2013).

[108] R. Pani et al. “Pulse height non-linearity in LaBr3:Ce crystal for gamma ray spectrometry and imaging”. In: *Nuclear Physics B - Proceedings Supplements* 215 (2011). Proceedings of the 12th Topical Seminar on Innovative Particle and Radiation Detectors (IPRD10).

[109] A. Vacchi. *Toward the measurement of the hyperfine splitting in the ground state of muonic hydrogen*. Talk at the 1st FAMU coll. meeting. 2014. URL: `http://webint.ts.infn.it/ricerca/exp/famu.html`.

[110] E. Borie and G. A. Rinker. “The energy levels of muonic atoms”. In: *Reviews of Modern Physics* 54 (1982).

[111] G. Fricke et al. “Nuclear Ground State Charge Radii from Electromagnetic Interactions”. In: *Atomic Data and Nuclear Data Tables* 60.2 (1995).

[112] F. Bienz et al. “Transfer of negative muons from hydrogen to argon in gaseous H$_2$+Ar mixtures at high pressure”. In: *Journal of Physics B* 21 (1988).

[113] T. Suzuki, D. F. Measday, and J. P. Roalsvig. “Total nuclear capture rates for negative muons”. In: *Physical Review C* 35 (1987).

[114] L. I. Stoychev et al. "DFG-based mid-IR laser system for muounic-hydrogen spectroscopy". In: *SPIE Proceeding* 9135 (2014).

All of science is nothing more than the refinement of everyday thinking.

— Albert Einstein

ACKNOWLEDGEMENTS

Many people deserve a sincere acknowledgement for their help with this thesis. First of all, I would like to thank Prof. Michela Prest for the dedication and the willingness shown as my advisor. Of course, there are many other reasons to thank you, but I'd prefer to keep them for later. Together with Michela, it's impossible not to say thanks to Dr. Erik Vallazza: thank you for having involved me in the FAMU project when I was confused about my "experimental vocation", my future and my thesis.

My sincere gratitude goes to all the members of the FAMU collaboration, in particular to Prof. Andrea Vacchi and to Dr. Rita Carbone: thank you for the opportunity of being part of this experiment, your help and your support. Rita deserves a special acknowledgement for her stoic resistance and patience in putting up with me and my doubts during several skype calls. Your help, particularly in these last "Monday debriefings", has been priceless.

Naturally, a word must be spent for the rest of the lab crew. Being part of the InsuLab for these years (with ups and downs) has been amazing; a bit harmful for my health, but still amazing. Thank you for all the opportunities you gave me: during this master I took eleven exams, but everything I learned from you was not less important. Thanks to Daniela, primarily because one never forgets his first co-advisor and, secondarily, for the mutual support in our writing sessions. I'm also in debt with "Professor" Alessandro Berra, that in these years was almost a spiritual guide to me: thanks for all the tips for the analysis, without you this code wouldn't be the same.

Thanks to all my friends here, abroad, physicists and not, for having stood with me.

Finally, my last and most heart-felt thanks goes to my family and to Isabella, who keeps on making me discover new pieces of a wonderful reality.

Como, March 2015 D. G.